Optical spectroscopy of single InAs/AlAs quantum dots

Dipankar Sarkar

Facultad de Ciencias
Departamento de Física de Materiales

Dissertation submitted for the degree of Doctor of Philosophy at
Universidad Autónoma de Madrid

Director: Herko P. van der Meulen
Co-Director: José Manuel Calleja Pardo

Madrid, February 2009

.

Optical spectroscopy of single InAs/AlAs quantum dots

Dipankar Sarkar

Facultad de Ciencias
Departamento de Física de Materiales

Dissertation submitted for the degree of Doctor of Philosophy at
Universidad Autónoma de Madrid

Director: Herko P. van der Meulen
Co-Director: José Manuel Calleja Pardo

Day of dissertation defense: 18 March 2009

Members of tribunal:
Luis Viña Liste, Universidad Autónoma de Madrid (President)
Luis Brey Abalo, Instituto de Ciencia de Materiales de Madrid, CSIC (Secretary)
Fernando Agulló López, Universidad Autónoma de Madrid
Rolf J. Haug, Leibniz Universität Hannover
Luisa González Sotos, Instituto de Microelectrónica de Madrid, CNM-CSIC

Substitutes:
Fernando Calle Gómez, Universidad Politécnica de Madrid
Benito Alén Millán, Instituto de Ciencias Fotónicas, Barcelona

Acknowledgements

I would like to express my gratitude to the directors of the PhD thesis, Herko van der Meulen and José Manuel Calleja, for introducing me into the world of semiconductor spectroscopy and their personal care, guidance and really everlasting encouragement. I also thank my colleagues of the group Snezana, Eva, Anna and Fran. Thanks to Klaus Pierz, who grew and provided us the quantum dot samples, and to Rolf Haug and Joerg-Michael Becker for their collaboration on the mask fabrication. For help and discussions I thank Luis Viña and Carlos Tejedor, to whom I also owe the fellowships I received. I am grateful to Elias and Valentin Guadaño for technical support as well to Manolo for helium delivery. Many many thanks also to the other members of the department: Lola, Alberto, Daniele, Dario, Elena, Lukasz, Olga, Juancho, Javi, Ivan, Jose-Luis, Jesus and Marta for a lot of things (discussions, help, company, lunch time, ...). During the past years I had the occasion to collaborate with other groups and stay at different laboratories and to get insight into other fields and techniques: I am grateful to Twan van Lippen, Richard Noetzel (Eindhoven Univ. of Technology), Rui He, Cyrus Hirjibehedin, Aron Pinczuk (Columbia University), Matthew Grayson, Gerhard Abstreiter (Walter-Schottky Institute, TUM), Pablo Molina, Luisa Bausa (Universidad Autónoma de Madrid), Ivan Prieto-Gonzalez, Luis Martinez, Aitor Postigo (Instituto de Microelectrónica de Madrid, CNM-CSIC) and the co-workers of these groups.

Finally, all my gratitude to my friends and my family.

Introducción

Los puntos cuánticos (PCs) son considerados como "átomos artificiales" fabricados en un laboratorio, porque se comportan en varios aspectos como átomos, debido a su densidad de estados cero-dimensional. Pero los PCs permiten el control sobre la energía de los estados, por ejemplo, aplicando un campo eléctrico o magnético, y también por ingeniería de banda de semiconductores. Además son fáciles de excitar ópticamente. Por otro lado, constituyen un sistema más complejo que abarca muchas partículas y grados de libertad, incrementando la cantidad y clase de las interacciones posibles. Estos átomos artificiales se pueden considerar como un laboratorio que permite la investigación de propiedades intrínsecas de la mecánica cuántica como indistinguibilidad, enlazamiento y desfase.

La comprensión de estos procesos en PCs es indispensable de cara a la realización de futuros dispositivos para el procesamiento cuántico de información, incluyendo computación y criptografía. Los posibles desarrollos basados en PCs incluyen elementos claves como emisores de fotones aislados y pares enlazados. Se ha demostrado ya la emisión de fotones aislados por PCs. La emisión de pares de fotones enlazados en polarización por PCs ha sido asimismo propuesta y demostrada.

El desdoblamiento de la estructura fina (FSS) y la energía de ligadura del biexciton (BBE) son parámetros físicos esenciales para la implementación de tales dispositivos. La secuencia de emisión biexciton-excitón-estado fundamental resulta en una cascada de dos fotones. El primer fotón se origina en la transición del biexciton a uno de los dos posibles estados de espín de excitón y su energía se distingue en la BBE del segundo fotón, emitido por la recombinación del excitón. Los dos posibles estados de espín de excitón están típicamente desdoblados debido a la interacción de intercambio de electrón y hueco. Si este desdoblamiento es más grande que la anchura homogénea de la línea, los caminos de recombinación son distinguibles y el enlazamiento cuántico

es imposible.

Los excitones confinados en PCs están sujetos a interacciones con otras excitaciones del cristal. El scattering elástico e inelástico con fonones es de importancia fundamental, y determina, entre otras, las contribuciones a la anchura y la forma de línea de la emisión. Las interacciones con fonones producen desfases, lo que limita el número de posibles operaciones coherentes en un dispositivo cuántico. Además, la interacción con fonones determina los procesos de relajación, que son cruciales para la operación eficiente de dispositivos ópticos.

Aparte de las aplicaciones cuánticas futuras, se han desarrollado aplicaciones clásicas con PCs. Dispositivos de opto-electrónica basados en PCs incluyen diodos de emisión de luz, fotodetectores, láseres y amplificadores ópticos. También son muy prometedores para dispositivos de memorias. Asímismo se han usado nanocristales en aplicaciones biológicas.

Muchos estudios, incluyendo algunos de los citados arriba, se concentran en el sistema material de puntos de In(Ga)As dentro de una matriz de GaAs. Menos atención se ha dirigido a los PCs similares de InAs/AlAs. No obstante, el sistema de InAs/AlAs es una combinación atractiva por varias razones. Las barreras altas y adicionalmente la incorporación de aluminio en el PC dan lugar a una fotoluminiscencia (FL) corrida hacia el azul. El corrimiento de la emisión, no solo hace interesante el sistema para aplicaciones de dispositivos ópticos, sino también para la investigación fundamental, dada la disponibilidad de láseres y detectores sensibles en el rango visible del espectro. Las barreras altas también impiden la disminución de la FL a temperaturas altas, porque la activación térmica de cargas a estados de la capa de mojado (wetting layer) o de la barrera está dificultada. La mayor localización de los portadores de carga hace esperar mayores interacciones de Coulomb en comparación con PCs de InAs/GaAs. También son de esperar interacciones de orden mas alto (correlación), porque las barreras altas confinan más estados de electrones y huecos. En relación con las propiedades vibracionales, la localización fuerte de portadores de carga y las barreras mas duras reducen la interacción del excitón con los fonones ópticos de la barrera.

No obstante, se han publicado solo unos pocos estudios ópticos de puntos cuánticos con barreras conteniendo aluminio, a diferencia de PCs de InAs/GaAs. La mayoría de los trabajos fueron realizados en conjuntos de PCs y estudiaron las propiedades

estructurales y la FL. Algunos de estos estudios fueron realizados en muestras con alta densidad de PCs, revelando efectos de acoplamiento entre PCs y, además, fueron estudiados efectos relacionados con la barrera indirecta de AlAs. Las propiedades vibracionales de conjuntos de PC fueron estudiadas por espectroscopia Raman e infrarroja, así como por excitación de FL.

En esta tesis se investigan puntos cuánticos aislados de InAs/AlAs mediante espectroscopia óptica. Para ello, se introduce la técnica de espectroscopia de PCs en el laboratorio, construyendo un microscopio de micro-FL y se establecen métodos básicos de caracterización. Se determinan las propiedades fundamentales de PCs de InAs/AlAs. La investigación sistemática de PCs revela propiedades electrónicas y vibracionales importantes a la vista de lo discutido arriba.

La tesis esta organizada de la siguiente manera: El capitulo 2 empieza con una descripción de los montajes experimentales construidos y utilizados en este trabajo. Además, se dan detalles de los PCs de InAs/AlAs investigados y finalmente se describe el método de fabricación de las mascaras sobre la muestra.

Los siguientes tres capítulos están dedicados a resultados experimentales y su análisis. El fin de capitulo 3 es dar una idea general de los propiedades fundamentales de PCs de InAs/AlAs. Contiene medidas macro-FL y micro-FL del conjunto de PCs que revelan los primeros resultados sobre el alineamiento de los estados. Todas las demás medidas se han realizado en PCs aislados. Se muestra de qué manera se usan series temporales, espectros en función de la polarización y de la intensidad de excitación para identificar la emisión del excitón y biexciton de un PC individual. Además, se presentan experimentos variando la temperatura y el campo magnético.

En el capitulo 4 se investigan las propiedades electrónicas de los PCs de InAs/AlAs dependiendo del tamaño. Se mide la BBE (sección 4.3) y el FSS (sección 4.4) en función de la energía de emisión del excitón. Los resultados son interpretados en términos de interacción de Coulomb.

El capitulo 5 enseña resultados experimentales de FL y excitación de FL relacionados con propiedades vibracionales. La sección 5.2 trata de la formación de estados de polaron que involucran el fonón óptico del PC de InAs. En la sección 5.1 se identifican todos los demás fonones ópticos-longitudinales del sistema PC-barrera. En la última sección 5.3 de este capitulo se investigan las interacciones entre excitón y fonones acústicos y especialmente se distinguen mecanismos de acoplamiento diferentes. Se

demuestra que parte de la interacción es mediada por el mecanismo piezoeléctrico, a diferencia de la atribución común al mecanismo de potencial de deformación. Ello constituye un aspecto nuevo y original en la observación experimental de interacciones excitón-fonón acústico.

Finalmente, se encuentra una lista de los resultados principales al final de la tesis en capitulo 6.

Conclusiones

Se ha presentado un estudio de espectroscopia óptica de puntos cuánticos auto-ensamblados individuales de InAs/AlAs. Se han desarrollado nuevas técnicas experimentales para este estudio en el laboratorio de Espectroscopía contínua en la UAM. Las propiedades básicas de los puntos cuánticos de InAs/AlAs, apenas estudiados, han sido investigadas y comparadas con los detalladamente estudiados puntos cuánticos de InAs/GaAs. Además, se han encontrado dependencias sistemáticas de las propiedades electrónicas y también se han estudiado las interacciones del excitón confinado con fonones ópticos y acústicos. Los resultados principales están resumidos en los siguientes puntos:

Condiciones experimentales:

- Se ha montado un microscopio de micro-fotoluminiscencia que permite por su alta resolución espacial la espectroscopia de puntos cuánticos aislados. Para medidas de excitación de luminiscencia el pre-monocromador ha sido automatizado construyendo una interfaz electrónica y se han desarrollado programas de ordenador para la adquisición automática de datos.

- Para reducir el numero de puntos cuánticos examinados, mascaras opacas con aperturas cuadradas de tamaños de 0.2 hasta 10 μm han sido fabricadas mediante litografía de haz de electrones sobre la muestra en colaboración con el Prof. R.J. Haug y J.M. Meyer (Leibniz Universität Hannover, Alemania).

Propiedades básicas de puntos cuánticos de InAs/AlAs

- Las medidas de micro-fotoluminiscencia de conjuntos de puntos cuánticos revelan lineas de emisión estrechas por debajo de 1.8 eV, y emisión continua para

energías mas altas. El carácter indirecto del gap de la matriz causa una transición inducida por confinamiento cuántico en el espacio real y reciproco (tipo I - tipo II y Γ-X, respectivamente) mediante la reducción del tamaño del punto cuántico. Para puntos cuánticos pequeños el estado fundamental del excitón se sitúa por encima del borde de la banda X de AlAs, permitiendo el scattering del electrón a los estados extendidos de la barrera.

- Una serie de experimentos fundamentales de micro-fotoluminiscencia han sido llevados a cabo para obtener una primera idea general de los propiedades de puntos cuánticos de InAs/AlAs. Series temporales de espectros de fotoluminiscencia revelan difusión espectral del pico de emisión permitiendo la asignación de lineas de emisión a puntos cuánticos individuales. Espectros resueltos en tiempo muestran dobletes polarizados linealmente para la emisión del excitón y del biexciton. Espectros dependientes de la potencia de excitación permiten diferenciar entre la emisión del excitón y biexciton por sus dependencias de la potencia.

- Espectros de fotoluminiscencia variando la temperatura muestran el habitual corrimiento hacia el rojo de la emisión del excitón que corresponde a la dependencia de la energía del gap de InAs de volumen. El ensanchamiento de la linea de cero-fonón está dentro de los valores típicos aunque es mas bien alto con 1.5 μeV/K, lo que se atribuye a la distancia pequeña entre el punto cuántico y la superficie. Bandas de fonones acústicos han sido identificadas y estudiadas con mas detalle (véase más adelante).

- Medidas de fotoluminiscencia con campo magnético revelan un corrimiento diamagnético extremadamente pequeño (1.4 μeV/T^2) por la fuerte localización debido a las altas barreras. El desdoblamiento Zeeman revela un factor g del excitón de 1.7, lo que esta en el rango típico de los valores observados. La polarización circular de la emisión del excitón es restaurada para campos magnéticos moderados por encima de 4 T, indicando una simetrización de las funciones de onda del electrón y hueco.

Propiedades electrónicas:

- Energías de ligadura del biexciton extremadamente altas, hasta 9 meV, han sido observadas y atribuidas a efectos de correlación aumentados por las altas barreras de AlAs. La energía de ligadura del biexciton es sensible al tamaño del punto cuántico, ya que su magnitud disminuye aumentando la energía de emisión del excitón. Además, el biexciton se vuelve anti-ligado para energías de emisión por encima de 1.63 eV. La tendencia es similar a las publicadas para puntos cuánticos de InAs/GaAs y igualmente atribuida al balance entre contribuciones directas de Coulomb y un impacto dominante de contribuciones de correlación. Para puntos cuánticos pequeños, con menos estados ligados, las contribuciones de correlación se reducen y las contribuciones repulsivas de Coulomb dominan.

- Desdoblamientos de estructura fina del estado del excitón hasta 0.3 meV han sido observados y son en general mayores que el desdoblamiento en los puntos cuánticos de InAs/GaAs tradicionalmente investigados. Esta diferencia se atribuye a efectos piezoeléctricos grandes, debido a la mayor constante piezoeléctrica de AlAs y a la morfología del punto cuántico. Ambos, la proporción altura/diámetro grande y la reducida mezcla entre indio y aluminio, que implica tensiones mas grandes, conducen a efectos piezoeléctricos aumentados.

- La energías de ligadura del biexciton y el desdoblamiento de estructura fina del estado del excitón se hacen ambos cero aproximadamente para la misma energía de emisión del exciton lo que sugiere un origen en común. Eso se atribuye tentativamente a la reducción simultanea de las contribuciones de intercambio y correlación al disminuir el tamaño del punto cuántico.

Interacciones del excitón con fonones:

- Los espectros de excitación de fotoluminiscencia de un punto cuántico exhiben resonancias anchas en múltiplos de 31 meV que se atribuyen a la formación de polarones implicando el fonón longitudinal-óptico de InAs del punto cuántico. Eso es contrario a lo observado en puntos cuánticos de InAs/GaAs, donde tipicamente se observa la formación del polaron con el fonón óptico de GaAs de la barrera. Este resultado evidencia el peor acoplamiento del excitón al fonón de la barrera debido a la fuerte localización del excitón en el punto cuántico de InAs y debido al material mas duro de la barrera de AlAs.

- Se han observado múltiples resonancias en el espectro de alta resolución de excitación de fotoluminiscencia de un punto cuántico individual, revelando que el excitón se acopla a todos los fonones longitudinales-ópticos del sistema barrera-fonón. Especialmente, una resonancia a 41 meV se asocia al fonón tipo-AlAs del punto cuántico. Eso constituye la detección directa mediante técnicas ópticas de la incorporación de aluminio en un punto cuántico individual, que se estima por debajo de 10 %.

- Se han estudiado interacciones entre excitón y fonón acústico variando la temperatura, la intensidad de excitación y la energía de excitación. Se han observado bandas de fonones acústicos muy anchas que se atribuyen al acoplamiento mediante el mecanismo de potencial de deformación. El gran desdoblamiento de estructura fina del excitón permite la identificación de bandas para cada uno de las lineas de cero-fonón. Aparte de ello, se han observado estrechas bandas de baja energía que se atribuyen al acoplamiento piezoeléctrico entre excitón y fonón acústico. Espectros de fotoluminiscencia en función de la intensidad y energía de excitación respaldan esa atribución por la observación de un efecto de apantallamiento. Cargas libres fotocreadas, que se sitúan en la capa de mojado (*wetting layer*), son capaces de apantallar la interacción. Se estima una longitud de apantallamiento característica de 10 nm, que es en el orden del tamaño del punto cuántico, demostrando la relevancia del efecto de apantallamiento en el sistema.

Abbreviations and Symbols

Mathematical and physical Symbols	
$\hbar$	Planck constant
T	Temperature
B	Magnetic field
E	Energy
d	spot diameter
D	beam diameter
F	focal length
l	focus extent
λ	wavelength

Chemical symbols of elements and compounds	
Ar	Argon
N_2	Nitrogen
Si	Silicon
Ti	Titan
HeNe	Helium-Neon
AlAs	Aluminum arsenide
GaAs	Gallium arsenide
InAs	Indium arsenide
DCM	4-dicyanomethylene-2-methyl-6-(p(dimethylamino)styryl)-4H-pyran
EL	Ethylene lactate
MIBK	Methyl Isobuthyl Cetone
MMA	Methyl-metacrylat
PMMA	Poly-methyl-metacrylat

Abbreviations	
AFM	Atomic force microscope
BBE	Biexciton binding energy
CCD	Charged coupled device
CB	Conduction band
CBM	Conduction band minimum
CL	Cathodoluminescence
cw	Continuous-wave
D	Dimensional
DWELL	Quantum dot in a quantum well
FSS	Fine structure splitting
FWHM	full width at half maximum
GS	Ground state
IF	Interface
IR	Infrared
LO	Longitudinal optical
LA	Longitudinal acoustical
MBE	Molecular beam epitaxy
MOCVD	Metal organic chemical vapor deposition
NA	Numerical aperture
NC	Nanocrystal
NIR	Near-infrared
NSOM	Near field scanning optical microscope,
PL	Photoluminescence
PLE	Photoluminescence excitation
QD	Quantum dot
RHEED	Reflection high energy electron diffraction
RTN	Random telegraph noise
SAQD	Self-assembled quantum dot
SEM	Scanning electron microscope
SNOM	Scanning near field optical microscope,
TEM	Transmission electron microscope
UV	Ultra violet

VB	Valence band
VBM	Valence band maximum
VIS	Visible
WD	Working distance
WL	Wetting layer
X	Exciton
XX	biexciton
X^+	Positively charged exciton
X^-	Negatively charged exciton

Contents

1 Introduction and objectives **25**

2 Experimental details **29**

2.1 Setups 30

2.1.1 Introduction 30

2.1.2 Macro- and magneto-photoluminescence setup 31

2.1.3 Microscope setup 35

2.2 Samples 39

2.2.1 Introduction 39

2.2.2 InAs/AlAs quantum dot sample 41

2.3 Masks 43

3 Basic properties of InAs/AlAs QDs **47**

3.1 Macro-photoluminescence 49

3.2 Micro-photoluminescence of the quantum dot ensemble 52

3.2.1 Introduction 53

3.2.2 Results 56

3.3 Micro-photoluminescence of single quantum dots 59

3.4 Temperature dependence 62

3.4.1 Results 65

3.5 Time evolution 70

3.5.1 Results 74

3.6 Excitation power dependence 76

3.6.1 Results 79

3.7 Polarization dependence 82

3.7.1 Results 87
3.8 Magnetic field dependence 88
3.8.1 Results 93

4 Electronic properties 99
4.1 Introduction 99
4.2 Experiment 102
4.3 Results: Biexciton binding energy 103
4.4 Results: Fine-structure splitting 104
4.5 Conclusion 107

5 Vibrational properties 109
5.1 AlAs-like LO-phonon and Intermixing 112
5.1.1 Introduction 113
5.1.2 Experiment 114
5.1.3 Results 114
5.2 InAs-like LO-phonon and polarons 119
5.2.1 Introduction 120
5.2.2 Experiment 121
5.2.3 Results 121
5.3 Piezoelectric exciton-acoustic phonon coupling 125
5.3.1 Introduction 125
5.3.2 Results and Discussion 127
5.4 Conclusions 133

6 Conclusions 135

List of Figures

2.1 Macro-photoluminescence setup. 31
2.2 Micro-photoluminescence setup. 35
2.3 Alignment. 36
2.4 Image of the spot on the CCD camera of the spectrometer. 38
2.5 The InAs/AlAs QD sample: TEM, AFM and layer structure. 41
2.6 Mask fabrication steps. 44
2.7 Mask fabrication: Optical microscope image. 45
2.8 Mask fabrication: Scanning electron microscopy image. 46

3.1 Macro-photoluminescence spectra. 51
3.2 Energy diagram. 55
3.3 Micro-photoluminescence spectra of QD ensembles. 56
3.4 Photoluminescence mapping. 60
3.5 Micro-photoluminescence spectra of a single QD. 61
3.6 Temperature dependent photoluminescence spectra. 66
3.7 Temperature dependence of the exciton emission energy. 67
3.8 Temperature dependence of the linewidth. 69
3.9 Photoluminescence spectra of a single QD for different cool down cycles. 74
3.10 Time series of photoluminescence spectra: Spectral jitter. 75
3.11 Excitation power dependent photoluminescence spectra. 80
3.12 Excitation power dependence: Intensities of the X and XX transitions. 81
3.13 Exciton level scheme. 83
3.14 Polarization-resolved photoluminescence spectra of a single QD. . . . 87
3.15 Magnetic field: Exciton level scheme. 90
3.16 Magneto-photoluminescence spectra. 93

3.17 Magneto-PL: Zeeman splitting, diamagnetic shift and sidebands. . . . 95

4.1 Dependence of the biexciton binding energy on the exciton emission energy. 103
4.2 Dependence of the bright exciton fine-structure splitting on the exciton recombination energy. 105

5.1 Scheme of Phonon-assisted absorption and emission processes. 112
5.2 Photoluminescence and PL excitation spectra of a single QD. 114
5.3 Photoluminescence intensity gray-scale plot. 115
5.4 Polarization resolved PL spectra for varying excitation energies. . . . 116
5.5 Unpolarized PL spectra for varying excitation energy: Successive intensity resonances of X and X+. 117
5.6 Polarization resolved PL spectra for excitation near the Y exciton resonance. 119
5.7 Excitation power dependence. 121
5.8 Polaron states: Excitation energy dependent photoluminescence spectra. 122
5.9 Polaron states: Photoluminescence and PL excitation spectra. 123
5.10 Photoluminescence spectra of an exciton doublet of a single QD for temperatures of 10 and 30 K. 126
5.11 Narrow sidebands due to piezoelectric exciton-acoustic phonon coupling. 127
5.12 Screening effect: Photoluminescence spectra of the exciton doublet for a series of excitation power. 129
5.13 Screening effect: Total apparent linewidth of the exciton peaks versus excitation energy for constant excitation power. 132

List of Tables

2.1 Details on the equipment used. 33
2.2 Mask fabrication: Recipe for the lift-off process. 43

Chapter 1

Introduction and objectives

Semiconductor quantum dots (QDs) are considered as "artificial atoms" fabricated in a laboratory, since they behave like atoms in many ways due to their zero-dimensional density of states. But the QD system allows the control over the confinement of the electronic states, for example, by applying electric or magnetic fields, as well as during the "design" (growth) by semiconductor band engineering. Furthermore, they are easy to excite optically. On the other hand they represent a more complex system that comprises many particles and degrees of freedom, increasing the number and kind of possible interactions. These "artificial atoms" may be considered as a testing ground for fundamental quantum mechanical phenomena, allowing the investigation of intrinsic quantum mechanical concepts as indistinguishability, entanglement and dephasing. The understanding of these processes in QDs is also indispensable in view of the realization of future devices for light emission and detection, as well as for quantum information processing, including both computation and cryptography. Implementations with QDs might provide some key elements [1] as single and entangled photon-pair sources [2]. QD single photon emission [3, 4] and indistinguishability [5] have been demonstrated already. Triggered polarization-entangled phonon pair emission by QD based sources was proposed [6] and demonstrated [7, 8]. The fine-structure splitting (FSS) and the biexciton binding energy (BBE) are essential physical quantities for the implementation of such devices. The biexciton-exciton-ground state decay sequence results in a two photon cascade. The first emitted photon originates from the decay of the biexciton into one of two possible spin-states of the bright exciton and its energy differs by the BBE from the second photon, which results

from the exciton recombination. The two possible exciton spin-states are typically split in energy due to electron-hole exchange interaction. If this splitting is larger than the homogeneous linewidths, the decay paths are distinguishable and quantum polarization-entanglement is unfeasible.

Excitons confined in QDs are subject to interactions with other excitations of the crystal. Elastic and inelastic scattering with phonons are of fundamental importance, and determine among other contributions the linewidth and shape of the emission transition. Interaction with phonons leads to dephasing, which limits the possible number of coherent quantum operations of a quantum gate device. Apart from this, the interaction with phonons determines relaxation processes, which are of fundamental importance for the efficient operation of optical devices.

Besides these future quantum applications, rather classical applications with QDs have been realized or proposed. Optoelectronic devices based on QDs include light-emitting-diodes [9], infrared photodetectors [10, 11], QD lasers [12] and semiconductor optical amplifiers [13]. They are also promising for memory devices [14]. Colloidal nanocrystals are used as tracers for biological applications [15].

Many studies, including some of those cited above, concentrate on the on the system of In(Ga)As dots embedded in a GaAs matrix. Much less attention has been paid to the similar InAs/AlAs QDs so far. However, the InAs/AlAs system is an attractive combination for several reasons. The high barriers and additionally the possible aluminum incorporation in the dot give rise to a blue-shifted PL. The shift of the emission peak makes the system not only interesting for optical device applications but also for fundamental research, since lasers and sensible detectors are available in the visible spectral region. Higher barriers also impede quenching of the PL at high temperatures, since thermal activation of carriers into the WL or barrier states is hindered. Stronger carrier localization lets expect increased Coulomb interactions compared to the InAs/GaAs QDs. Also, higher order Coulomb interactions may be expected since higher barriers confine more electron and hole states. With respect to the vibrational properties, strong carrier localization and a harder barrier material reduce the interaction of the QD exciton with the barrier optical phonons. However, only a few optical studies on single dots embedded in barriers containing aluminum have been published [16–19]. Most of the optical work was done on QD ensembles [19–33]. Some of these studies were performed on high dot density samples revealing inter-

dot coupling effects [23, 25, 34]. Effects related to the indirect gap of the barrier have been also addressed [35, 36]. The vibrational properties of QD ensembles were studied by Raman and infra-red spectroscopy [30–32, 37] as well by PLE spectroscopy [38, 39].

The scope of the thesis is the investigation of single InAs/AlAs QDs by means of optical spectroscopy. To this end, the technique of single dot spectroscopy is introduced into the laboratory by assembling a micro-PL microscope and basic methods of single dot characterization are established. Fundamental properties of single InAs/AlAs QDs are determined. The systematic investigation of these QDs provide information on the electronic and vibrational properties of importance in the view of the above discussion.

The thesis is organized as follows. Chapter 2 starts with a description of the experimental setups built and used in this work. Furthermore, details of the investigated InAs/AlAs QD samples are given and finally the fabrication method of the metal masks on top of the sample is described.

The following three chapters are dedicated to the experimental results and their analysis. The aim of chapter 3 is to provide a first insight into the basic properties of the InAs/AlAs QD sample. It contains macro-PL and micro-PL measurements of the QD ensemble, that reveal first results on the characteristics of the states (band alignment). All further measurements are done on single QDs. It is shown how time-series, polarization and excitation power dependent PL spectra are used to identify the exciton and biexciton emission lines of an individual QD. Furthermore, experiments for varying temperature and magnetic field are presented.

In chapter 4 size dependent electronic properties of InAs/AlAs QDs are investigated. The biexciton binding energy (sections 4.3) and the bright exciton fine-structure splitting (sections 4.4) are measured as a function of the exciton emission energy. The results are interpreted in terms of Coulomb interactions.

Chapter 5 provides experimental results of PL and PL excitation measurements related to the vibrational properties. Section 5.2 deals with the formation of polaron states involving the InAs QD LO sphonon. In sections 5.1 all other LO phonons of the dot-barrier system are detected. In the last sections 5.3 of this chapter exciton-

acoustic phonon interactions are investigated and in particular different coupling mechanisms are distinguished. It is demonstrated that part of the interaction is mediated by the piezoelectric coupling mechanism. This is in contrast to the common attribution of the coupling to the deformation potential mechanism and therefore constitutes a new, original aspect in the experimental observation of the quantum dot exciton-acoustic phonon interaction.

Finally, a list of the main results of this thesis can be found in chapter 6.

Chapter 2

Experimental details

Macro PL measurements on QDs reveal information on an energy scale in the order of the inhomogeneous broadening of the ensemble, which is typically around 30-100 meV for InAs/GaAs QDs [40–43] and for InAs/AlAs QDs [20, 23, 39]. Effects on the energy scale of a few meV or even of one order of magnitude less, e.g. the biexciton binding energy or the fine-structure of the exciton level, respectively, are obscured by the inhomogeneous broadening due to size, shape and composition variations of a large ensemble of QDs. Therefore, the investigation of effects on this energy scale requires, apart from low temperatures, the access to the individual QDs, by reducing the spot size and optionally by reducing the sample size using metal masks with small apertures or mesas [44]. Other approaches instead of micro-PL [45, 46] include near field scanning optical microscopy (NSOM) [47] and cathodoluminescence spectroscopy [48]. NSOM has a larger spatial resolution than micro-PL but a worse optical throughput.

In the present work high spatial resolution is achieved using micro-PL to provide a minimized spot size, as well as masks fabricated on top of the sample to reduce the probed sample size. In this chapter details on the used experimental setups, the mask fabrication and the sample structure are given.

2.1 Setups

2.1.1 Introduction

The present thesis is about optical spectroscopy of semiconductor quantum dots. The experimental techniques, equipment and setups relevant for this work will be described in this section. Optical spectroscopy allows the investigation of fundamental properties of materials, as it provides information about electronic and vibrational excitations.

Optical spectroscopy addresses the following light-matter interaction processes: 1. Absorption, 2. Radiative (emission) and no-radiative relaxation, 3. Elastic (Rayleigh) and inelastic (Raman) light scattering, the latter involving energy and impulse transfer between photons and elementary excitations (i.e. quasi particles) of the system. These can include e.g. vibrational modes (phonons), spin and charge collective excitations, etc, and 4. The optical absorption or emission process may be a phonon assisted transitions (including generation or absorption of phonons together with the photon). Optical spectroscopy permits to observe these processes in different types of experiments. The ones realized in this work are: (i) Photoluminescence spectroscopy, i.e. the analysis of light emitted by a system excited by light, and (ii) Photoluminescence excitation spectroscopy, i.e. photoluminescence spectroscopy for varying excitation energy. Observations in the latter type of experiment can include, apart from the photoluminescence, (resonant) Raman scattering as well phonon assisted processes, i.e. transitions involving the absorption or emission of a phonon. Distinction of them is rather a matter of interpretation than experimental realization.

The experimental setup in optical spectroscopy can be divided conceptually in the following components: (i) a light source (laser), (ii) the sample and its environment, (iii) instruments for analysis and detection of the emitted light (spectrometer+ detector) (iv) Data handling system. These components are common to the macro-, micro- and magneto- photoluminescence setups used in the present work. Some details on these components are given in the following. The sample will be described separately in section 2.2.2.

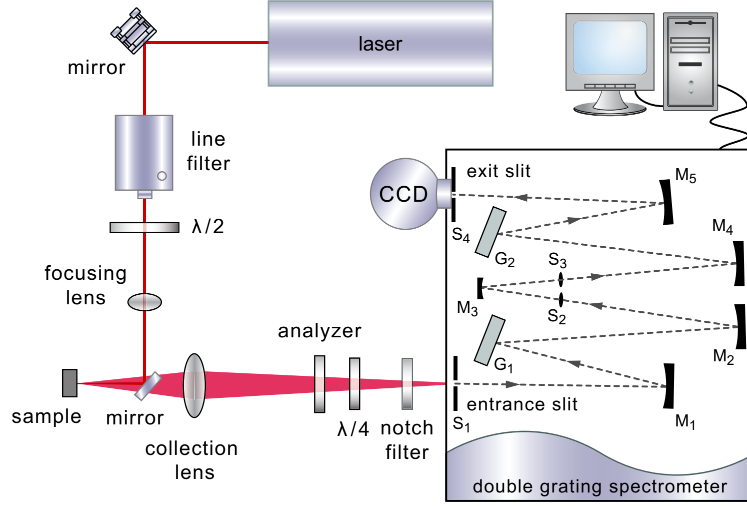

Figure 2.1: Experimental setup for macro-photoluminescence measurements. After: [49].

2.1.2 Macro- and magneto-photoluminescence setup

The model numbers, specifications and characteristic properties of the instruments described in the following can be found in table 2.1.

Lasers are useful for optical spectroscopy due to their characteristic properties, namely (i) very small beam divergence, (ii) coherence, (iii) very narrow line widths, (iv) very high intensity per bandwidth, (v) highly polarized emission and (vi) available in the excitation energy range required for semiconductor materials.

The small beam divergence results in good focusing characteristics: a spot diameter of (Gaussian optics) $d = 4\lambda F/\pi D$ and a depth of field of $l = 16\lambda F^2/\pi D^2$ can be achieved with a lens of focal length F and a beam diameter D at a wavelength λ. This permits to reduce the spot diameter for visible light typically to 50-100 μm with a 10 cm focal length lens and even down to about 1 μm near the diffraction limit with a microscope objective. Different continuous-wave lasers, namely Argon ion and HeNe-Lasers, as well tunable Ti:Sapphire- and dye lasers were used, depending on the required excitation energy. Stable dyes like DCM, Pyridine or Styryl 9 were used for the 600-1000 nm spectral range. The tunable dye and Ti:Sapphire Lasers are equipped with stepper motor driven birefringent filter which allows computer-controlled tuning of the wavelength. This is particularly useful for automated data acquisition in the photoluminescence excitation experiments. In table 2.1 model numbers and further

details on the used lasers are summarized.

On the detection side a single or a double grating spectrometer is used for the spectral analysis. The former is equipped with gratings of 1200 grooves/mm or1800 grooves/mm, the latter with pairs of gratings of 1800 grooves/mm or 600 grooves/mm, with a blaze optimized for the operation in second order of diffraction. The resolution of a spectrometer depends on the width of the entrance slit, the total number of grooves illuminated, and focal distance. The spectral resolution $\Delta\nu$ is given by $\Delta\nu = \Delta x\ (\nu^2/F)\ \sqrt{d^2 - 1/(4\nu^2)}$, being ν the wavenumber, Δx the slit width, F the focal length and d the grating period (all in cm or cm^{-1}).

For slits of 0.1 mm and 1800 groves/mm the spectral resolution of the double spectrometer is about 0.1 meV at a wavelength of $\lambda = 800$ nm. The laser plasma emission or the lines of a neon lamp were used for wavelength calibration of the spectrometers.

For multichannel detection in the visible spectral range silicon charge coupled devices (CCDs) are mounted on both spectrometers. The pixel size is 27 micron. Both detectors are cooled with liquid nitrogen down to approximately 140 K in order to reduce the noise level. The spectrometer and the CCD are computer-controlled. Characteristic properties of the spectrometers and CCDs as well model numbers are listed in table 2.1.

Other optical components are placed in the experimental setup, for the analysis of the polarization properties, as prisms (Nicol or Glan-Thompson prism) and film polarizers (Polaroid "H-sheets"). The former have the advantages of higher contrast, cover a larger wavelength range and absorb less light in comparison with film polarizers. Additionally, phase plates are used to change the polarization state of the light. The undesired polarization sensibility of the spectrometer originated mainly by the gratings is eliminated by converting linearly polarized light to circular polarized with a quarter wave plate (45°) located in front of the entrance slit of the spectrometer. Short-wave-pass filters (550 or 740 nm) are placed in front of the spectrometer's entrance slit in order to get rid of spurious laser light, especially in the case of the single grating spectrometer. Furthermore, filters are used to eliminate overlapping first and second order diffracted light in the case of the double grating spectrometer with the 600 groves/mm gratings operated in second order mode.

All the measurements presented are performed at low temperatures in the range

Laser-Systems		
Ar^+	Spectra-Physics Beamlok 2060/2080	
Ti:Sapphire	Spectra-Physics 3900 S	different optics depending on wavelength region
Dye	Spectra-Physics 375 B	different optics depending on wavelength region
HeNe	Optlectra 1125P no.44-3192	632.8 nm, 5 mW
Detectors		No. Pixels, pixel size (μm)
Si-CCD (Mounted on Spex 1404)	Jobin-Ivon SpectraView 2D	1024x256, 27x27, visible, Nitrogen cooled
Si-CCD ((Mounted on Spex 750 M))	Jobin-Ivon CD3000v	1024x256, 26x26, visible, Nitrogen cooled
Spectrometers		Focal distance, NA
Single grating	Spex 750 M	F=75 cm, NA = f/???
Double grating	Spex 1404	F=85 cm, NA = f/7.8
Cryostats		
Continuous helium flow	Oxford CF204	10-300 K
Continuous helium flow	Cryovac	6-300 K, Temperature controller Cryovac TIC 304 MA
Helium bath	Cryogenic	Superconducting magnet 0-12 T , 2 K
Microscope setup components		
Long WD microscope objective	Nikon CF Plan	M=50x/NA=0.55 ,∞/0 EPI ELWD, WD 8.7
DC Motors	Standa	controller 8DCMC1.01, stepsize 13 nm

Table 2.1: Details on the equipment used. M=Magnification WD = Working distance, NA = Numerical aperture.

from 10 K up to approximately 100 K. The samples are mounted in continuous-flow or bath cryostats and cooled down with liquid helium. The cryostat used for macrophotoluminescence measurements has an outer vacuum chamber and an inner sample chamber, where the sample is fixed with rubber cement to the copper sample holder and is in direct contact with exchange helium gas. Microphotoluminescence measurements are realized with another cryostat suitable for microscope applications (see section 2.1.3). The sample is placed in an outer vacuum chamber and glued in this case with silver paint, for a good thermal conductivity, which is necessary since the sample is not in direct contact with the helium gas. This secures that the sample cools down at the same rate as the brass or copper sample holder and does not break due to strain caused by different thermal expansion coefficients. In the case of the continuous-flow cryostats, sometimes pressure and temperature oscillations occur. In order to prevent them, the helium flow was usually adjusted by almost closing the needle valve on the helium transfer tube, while the valve of the gas flow controller in the return line was quite opened, resulting in a gas flow of about 1 l/hour, and a pressure of 0.2 bar and a sample holder temperature of about 10 K.

Magnetophotoluminescence on single QDs is performed in an helium-4 bath cryostat with a superconducting magnet (0-12 T). The sample is mounted on a three axis piezo-stage (attocube ANPxyz50/LT), which allows selection and alignment of QDs. The piezoscanner together with the sample and an aspherical lens (focal length $F = 12$ mm, 8.4 mm working distance, 15 mm diameter, thus the spot size is around $d = 2.5$ μm at the wavelength of $\lambda = 800$ nm and for a beam diameter of $D = 5$ mm) are immersed in the helium bath and centered in the bore of the magnet. The magnetic field is aligned normal to the sample surface, i.e. parallel to growth direction.

Schemes of the setups for macro-PL (more details are given below) and micro-PL are shown in Figure 2.1 and Figure 2.2, respectively.

With respect to the optical configuration of the setup, backscattering geometry is employed in all setups including the micro-PL setup described in more detail in the following section. Distances as well focal lengths of the lenses are chosen to match approximately the numerical apertures of the spectrometers.

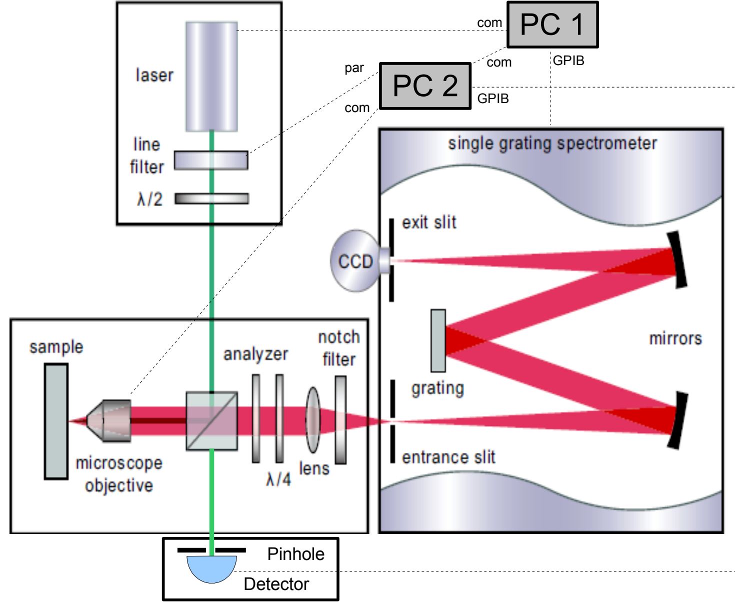

Figure 2.2: Microscope setup for micro-photoluminescence measurements. par = Parallel port, com = Serial port, GPIB = General purpose interface bus. After: [49].

2.1.3 Microscope setup

The optical spectroscopy of *single* QDs requires to reduce the spot size, which is in the order of 50-100 μm for a typical macro-PL setup. Therefore, a conventional microscope was set up for micro-PL measurements. A scheme of the chosen geometry is shown in Figure 2.2. Confocal geometry with the use of pinholes placed in intermediate image planes was not realized, as the improvement in lateral resolution by decreasing further the spot size by a factor $\sqrt{2}$ does not compensate for the more difficult alignment. The power of a confocal setup lies above all in the better depth resolution [50], which is not necessary in the present study of InAs/AlAs QDs.

The central component of the setup is the microscope objective, which is mounted on a computer-controlled three axis DC-motor stage. QBASIC programs were written to control the motion of the motors automatically. The position of the objective can be varied with a stepsize of 13 nm, sufficiently small to easily maximize the signal detected with the CCD. Typically 20 steps corresponding to 260 nm were used for fine alignment. Another useful application of the motors is the search of QDs in a low density area of the sample by an automatic 2D spatial scan of the surface in order to obtain a map of PL spectra (see Figure 3.4).

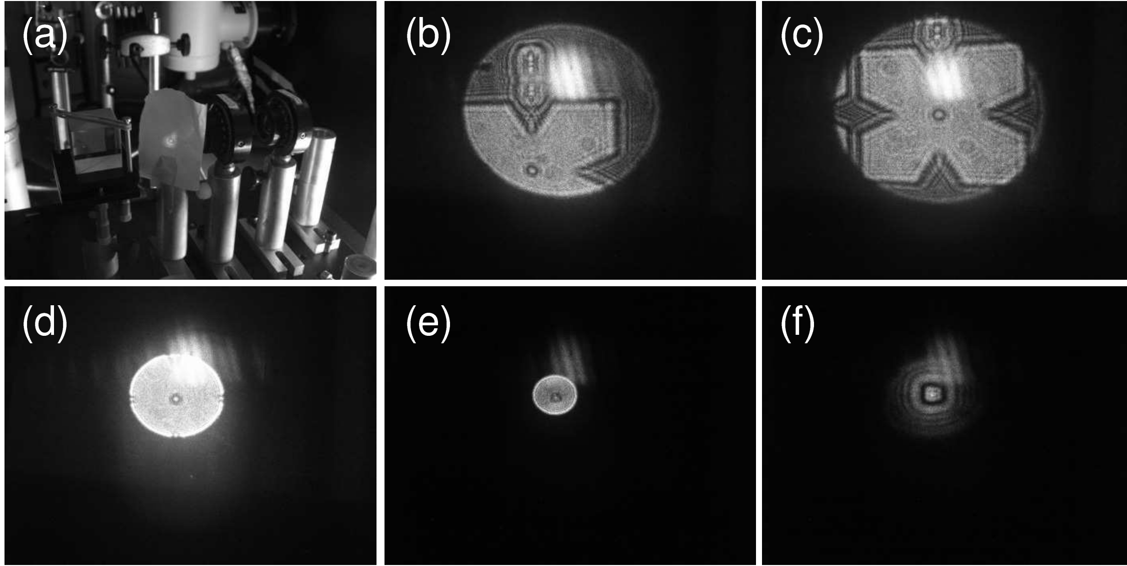

Figure 2.3: Rough alignment using the beam reflected on the sample surface. (a) A piece of paper is placed after the beam splitter. (b-f) Reflection of the laser beam (observed on the piece of paper): (b) The mask of interest is searched moving the unfocused microscope objective, (c) the mask is centered, (d,e) objectiv is approached to sample surface, (f) interference fringes due to the borders of the opening are visible when the sample reaches the focal plane of the objective, lateral dimension of the opening is 10 µm in the present case.

A first rough alignment of the microscope objective is done by observing the reflection of the laser beam on the sample surface on a piece of paper located after the beam splitter. Helpful are masks, markers or defects on the sample surface for positioning the laser spot onto the right place of the sample, as shown in the series of images in Figure 2.3. When the objective is too close to the sample surface, a large circular reflection limited by the dimensions of the objective is observed. As the sample approaches the focal plane of the objective, the circular reflection gets smaller and finally when the sample reaches the focal plane of the objective and the laser beam is moderately well focused, interference fringes appear due to the structured sample surface. Alternatively, also a real image of the sample surface on a CCD camera can be used for rough alignment.

The fine alignment starts on a strong PL signal, e.g. the emission of the bulk GaAs exciton. Objective (focus) and lens (focus and lateral movement) are displaced iteratively maximizing signal intensity on the spectrometer CCD. Then the spot is

positioned onto the aperture of the mask and PL intensity of a QD transition is maximized. After aligning the excitation spot by observing it on the imaging CCD camera (or the laser intensity on the CCD camera of the spectrometer) the final alignment is done by maximizing the PL signal on the CCD camera of the spectrometer. Maximizing the PL signal increases again the objective distance to the sample surface. This is due to chromatic aberration effects of the microscope objective: Focusing of the excitation beam onto the sample and collecting of the PL emission are done by the same objective, but the excitation and PL emission wavelength differ strongly, as they are typically 514 nm and around 800 nm, respectively. However, it is preferable to adjust the objective to the focal plane that corresponds to the PL emission wavelength, in order to obtain an optimized collection efficiency although excitation spot diameter is increased at the cost of spatial resolution. Finally, in order to reduce the noise level in the PL spectra, typically only 6 to 12 horizontal pixel lines of the spectrometer CCD area are selected for data acquisition (see also Figure 2.4: the spot on the CCD is about 10 pixels high, each spectraum shown corresponds to two pixel high areas).

Different configurations of the setup have been tried. For vertical arrangement of the cryostat, mechanical stability is achieved by placing the optical components with short posts onto on an elevated optical table, including the cryostat. If it is not mounted onto the elevated optical table it is crucial to fix both mechanically with a bar. Generally, if the cryostat is mounted horizontally a better mechanical stability is achieved. After approximately one hour of circulating helium thermal equilibrium is reached and an acceptable stability is achieved.

Usually a prism monochromator is placed in the laser beam path in order to eliminate the background emission of the Ti:Sapphire, the dye fluorescence or the plasma lines in the case of the argon and HeNe lasers. For the PL excitation measurements the laser is tuned continuously through a wavelength range and the prism monochromator has to be adjusted synchronously. Automated control of the prism monochromator was realized by installing a stepper motor that rotates the prism. The appropriate electronics including the interface to the computer's parallel port and a stepper motor driver was built [51]. This control was performed by a second PC (PC 2), communicating with the first PC (PC 1) used for data acquisition and spectrometer control (see figure 2.2). Automated PL excitation measurements could

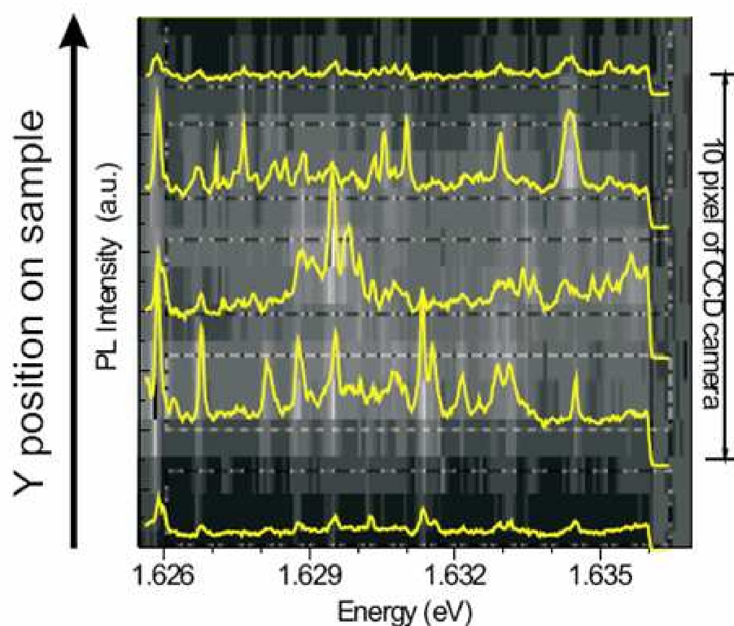

Figure 2.4: Background: Image of the spot on the CCD camera of the spectrometer. The PL curves in the foreground correspond to the integrated area of the dashed boxes of two pixel height: Inside the diffraction-limited µm-sized spot different QDs are spatially and spectrally resolved.

be performed this way using scripts for the data-acquisition software (SPECTRA-MAX) and QBASIC-programs for the monochromator control and laser control and for the PC-interfacing.

An automatically acquired PL excitation series starts with a manually aligned setup. For each new PL spectrum first the laser frequency is set, with the consequence that the beam passing through the prism monochromator slightly deviates from its original position. The prism monochromator is automatically adjusted by maximizing the laser intensity detected by a power meter after the unused beamsplitter output in the microscope setup. A power meter and a pinhole in front of it are placed at a large distance from the beamsplitter achieving a larger sensibility on the deviations.

Model numbers and specifications of the mentioned instruments can be found in table 2.1.

2.2 Samples

The self-assembly of semiconductor quantum dots is an elegant and simple method to fabricate strained, defect free nanometer-sized structures with fully confined electronic states. However, such strain-induced dots are not the only method for dot fabrication. In the following, different approaches are introduced and finally the sample used in this thesis is described.

2.2.1 Introduction

Various fabrication techniques are employed in order to fabricate nanostructures with 3D confinement, which can be categorized into two different approaches:

(i) The *top-down approach* is based on the high-resolution patterning [52] of larger structures, principally quantum wells, by e-beam lithography and dry etching. A main advantage of this technology is the scalability and the site-control. The main drawback of this method is that the lowest size limit is approximately 100 nm. Surface defects and processing-induced inhomogeneities also constitute a problem for optical applications as they affect the optical properties, and diminish luminescence efficiency.

(ii) The *bottom up approach* refers to the spontaneous assembly of nanostructures under specific conditions during epitaxial growth. Self-assembly is a strain-driven process due to the lattice mismatch of different materials used (Stranski-Krastanow growth mode). This is a direct and easy fabrication method for nm-sized structures in the sense that no post-growth processing has to be done, except for the structuring of masks or mesas that may be necessary for single dot spectroscopy. Epitaxially grown self-assembled islands are very small (a few nanometer) leading usually to large level spacings ΔE ($\Delta E > k_B T$, $\Delta E > \hbar\omega_{LO}$ (LO phonons)) [44]. A disadvantage of this method is that dot formation occurs at random sites, but some site control can be achieved with pre-patterned substrates [53–55]. A strict distinction into these two approaches is not always possible, since combinations of both exist: For example, the dot growth on pre-patterned substrates combines self-assembly and lithography. Strain-induced dots can be formed in quantum wells (QWs) by lateral strain modulation by self-assembled QD stressors on top of the well [56–58]. For example InP stressor on InGaAs/GaAs QW [58] result in a large size homogeneity, lack of dislocations, surface states and impurities and a parabolic potential. A disadvantage

of these type of dots is the large size, i.e. quantization energies of only a few meV. Other types of quantum dots include monolayer fluctuations at a GaAs/AlGaAs QW interface [59], known also as natural QDs, disorder induced dots by laser beam [60] or by ion beam [61], and cleaved-edge-overgrowth (CEO) QDs [62]. Furthermore, nanocrystals or colloidal quantum dots can also be prepared chemically. They have a small size distribution but sometimes surface states and defects diminish their optical efficiency [63].

The nanostructures investigated in the present thesis are self-assembled InAs/AlAs dots grown by the Stranski-Krastanow method using molecular beam epitaxy (MBE). The growth method consists in the deposition of material with a lattice constant a_0 different from the lattice constant a_S of the substrate. For the InAs/AlAs system the lattice mismatch $\Delta a/a_S = (a_0 - a_S)/a_S$ is 7.0 %, very close to value of 7.2 % of the widely studied InAs/GaAs system, since both AlAs and GaAs have very similar lattice constants of 5.66139 Å and 5.65359 Å, respectively (InAs $a_0 = 6.0583$ Å) [64]. When InAs is deposited, first a 2D pseudomorphic layer, named wetting layer, grows up to a critical thickness of a few monolayers, depending on the growth conditions. When the critical thickness is reached, the accumulated strain in the 2D layer is relaxed by the formation of 3D islands resulting in an reduction of the elastic strain energy. Island formation starts consuming both material being deposited and material from the wetting layer. During further growth a 1-2 monolayer thick wetting layer is conserved and only deposited material is incorporated into the dots [24]. For optical applications the dots are overgrown usually with the same material as the substrate. During this stage dots can change shape and composition. Details on the QD size, shape and composition depend on the growth conditions like substrate temperature, pressure and deposition rate, growth interruptions, and other parameters.

The formation of partially strained 3D islands was first demonstrated in lattice-mismatched Ge/Si(100) [65] and InGaAs/GaAs(100) [66]. Since then epitaxially grown self-assembled QDs (SAQDs) include a wide range of II-VI and III-V, group IV binary, ternary and quaternary materials. The most commonly studied system is InAs/(100)GaAs. Other III-V SAQDs include III-arsenides (InAs, AlAs on GaAs, AlAs, AlGaAs, and other ternaries[67]) III-antimonides (InSb, GaSb, AlSb QDs [68–70]) and III-phosphides (InP on AlGa0InP/AlInP [71]).

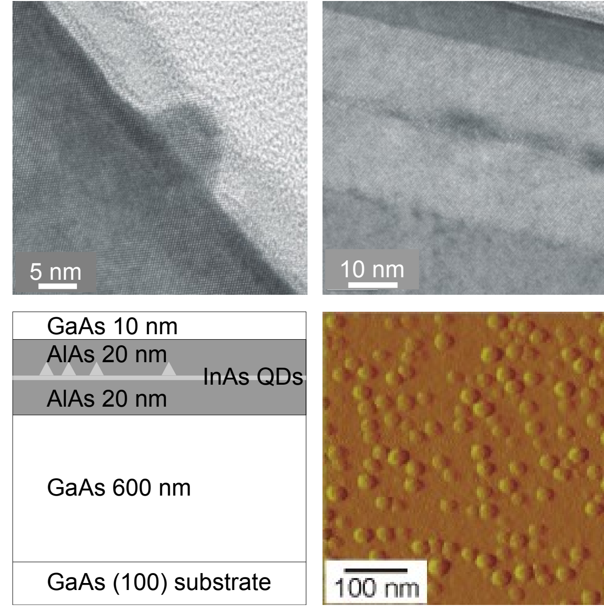

Figure 2.5: The InAs/AlAs QD sample: The top images are transmission electron microscope images of the QD region of the sample. The bottom left scheme shows the layer structure. An atomic force microscope image of an uncapped reference sample is shown in the bottom right panel.

2.2.2 InAs/AlAs quantum dot sample

The growth of InAs islands on AlAs (similar to those investigated in the present study) and GaAs substrates (the commonly studied system) show the following similarities and differences: (i) The critical thickness of InAs layers is identical for growth on both GaAs and AlAs. The transition from 2D layer growth to 3D formation of self-assembled islands is a strain-driven process and is consequently comparable on both cases due to their similar lattice constants [29]. (ii) The dot density on AlAs is initially very high (in the order of 10^{11} cm^{-2}) compared to the InAs/GaAs system [24, 27]. and independent of InAs coverage from 1.6 to 2 ML, in contrast to the growth of InAs/GaAs QDs, where the dot density depends on InAs coverage [27]. (iii) The island size increases with increasing InAs supply and exhibits a larger size inhomogeneity compared to dots on GaAs [29]. (iv) Growth of InAs QDs on AlAs is slower. This is explained by a reduced In surface mobility on the AlAs surface, due to the large Al-In bond strength and therefore results in an higher dot density and smaller QDs [29]. (v) For high growth temperatures $T_S = 530 - 540$ ℃, i.e.

increased In diffusion on the surface, the dot density depends on InAs coverage [29], similarly to the growth of InAs dots on GaAs [72]. This dependence is crucial for the fabrication of low density samples suitable for single QD spectroscopy, as carried out in the present thesis. (vi) The aspect ratio (height/diameter) increases with coverage (or QD volume) in the initial stage of QD growth [24] similarly to InAs/GaAs QDs [73]

K. Pierz of the Physikalisch Technische Bundesanstalt Braunschweig, Germany, grew the InAs/AlAs QD samples investigated in the present thesis by molecular-beam epitaxy (MBE) [67]. The layer structure of the samples is shown in Figure 2.5. First a GaAs buffer layer was deposited on a (100)-oriented GaAs wafer, followed by a 20 nm AlAs layer, grown at a substrate temperature of T_S = 600 ℃. Then the substrate temperature is lowered to 530 or 500 ℃ (sample A and B, respectively) during a growth interruption of 1 minute and stabilized for another minute. InAs was deposited in a cycled mode (5 s pause and 5 s InAs growth) at a slow rate of nominal 0.046 ML/s. A gradient in the InAs coverage of about 30 % corresponding to 1.4-2.0 ML across the 2 inch wafer is achieved due to the In source cell position in the MBE chamber and the substrate rotation interruption during InAs deposition. In this way a low dot density region is achieved in the case of high growth temperatures.The onset of island formation is observed with RHEED and occurs after the deposition of about 1.6 monolayers InAs [29]. The islands are covered with another 20 nm thick AlAs barrier and finally a 10 nm GaAs cap layer was grown on top of the sample in order to prevent oxidation of the AlAs surface.

An AFM study before capping shows that at high T_S = 530 ℃ (sample A) the QD density increases with increasing InAs coverage and the QD size is nearly constant with InAs coverage. At low InAs coverage the QD density is very low. In contrast, the other sample grown at low T_S = 500 ℃ (sample B) resulted in an almost constant QD density for all InAs coverages and in an increasing QD size with increasing InAs coverage. Figure 2.5 shows transmission electron microscopy (left and right top images) and atomic force microscopy (right bottom) images of the sample. The quantum dots used in this study have a typical diameter in the range of 20 nm, and a typical height of 2-4 nm. The dot density is up to 10^{11}cm^{-2}.

A more detailed description of the samples can be found in Ref. [67].

	Step	Details
1	Clean samples	On spinner, acetone and isopropanol, blow with N_2.
2	Layer I	Copolymer 10% in ethylene lactate: MMA(8,5) EL 10,
		Company MicroChem, rotate 60 s, 4000 rpm,
	Bake	Hot plate 180 ℃, 10 min
3	Layer II	PMMA 950k 2% in Anisole, rotate 60 s, 4000 rpm,
	Bake	Hot plate 180 ℃, 10 min
4	E-beam lithography	Write with 30 keV
5	Development	60 s in Methyl Isobuthyl Cetone (MIBK) : Isopropanol 1:3
6	Stop	Isopropanol bath, blow with N_2
7	Deposition	Sample mounted with angle of 45°,
		Evaporate 4 times 50 nm Al from all the 4 the directions
8	Lift-off	Acetone bath, some seconds ultrasound

Table 2.2: Details of the recipe for the lift-off process for e-beam defined openings in metal masks. EL = Ethylene lactate, MIBK = Methyl Isobuthyl Cetone, MMA = Methyl methacrylate, PMMA = Poly-methyl-metacrylate.

2.3 Masks

In order to measure the PL emission from a single QD it is necessary to employ appropriate experimental techniques like near field scanning optical microscopy, micro-PL, or cathodoluminescence spectroscopy. In micro-PL experiments, single dot spectroscopy can be realized in low density samples due to the small laser spot size. If the average distance between neighboring QDs is smaller than the spatial resolution of the microscope set-up, then the sample size has to be reduced. Usually the probed sample size is made smaller by fabricating metal masks on top of the sample with small openings allowing optical access only to a few dots, or by etching small mesas that contain only a reduced number of QDs. The use of masks has important advantages compared to mesas: The freestanding surfaces of the mesas can influence the optical properties of the QD. Minimum QD PL-linewidths larger than 0.1 meV are reported for mesas of lateral sizes below 100 nm containing InGaAs/GaAs QDs [74]. Although the minimum linewidth decreases for increasing lateral size of the mesa, no saturation is observed even for 500 nm large mesas. Consequently even in large mesas the lateral surfaces influence the QD confinement potential. This effect is related to spectral jitter, which is discussed in section 3.5. Another study on InAs/GaAs QDs [75] showed that scattering of phonons from the lateral sidewalls influences the temperature dependence of the zero-phonon linewidth and is relevant for mesa sizes up to a few µm. More details on the zero-phonon linewidth are given in chapter 3.4.

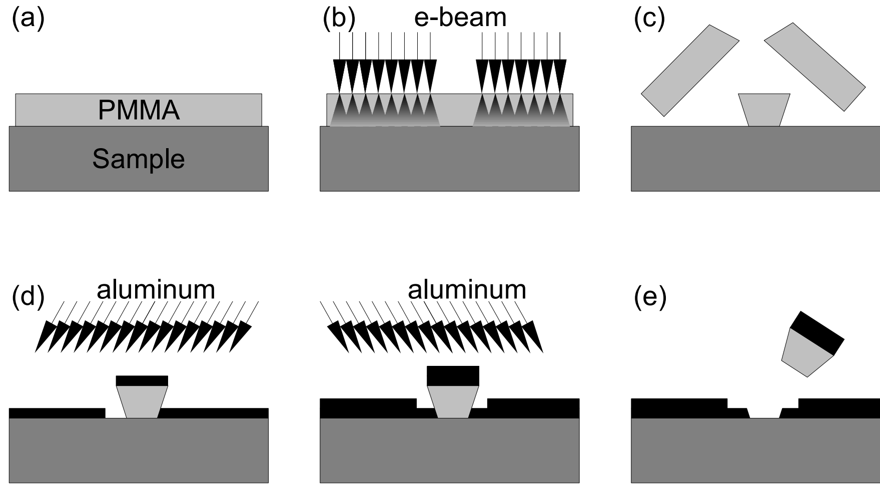

Figure 2.6: Steps of the mask fabrication by e-beam lithography and lift-off process. (a) Resist deposition, (b) e-beam writing, (c) development, (d) metal deposition and (e) lift-off.

However, as dots are close to the surface (30 nm in the present case) masks do not constitute a disadvantage for light collection.

Opaque aluminum masks on top of the samples were fabricated in collaboration with the group of Prof. R.J. Haug at the Leibniz University of Hannover, Germany. They consist of several series with square apertures ranging from 10 down to 0.2 μm. The fabrication techniques employed include e-beam lithography with a lift-off process. An etching step as required for mesa production is not necessary.

The fabrication procedure is the following (see Figure 2.6): First, the sample is cleaned and the poly-methyl-metacrylate (PMMA) resin is applied in two steps onto the sample and baked (see table 2.2 for details of these steps). Then, the patterns are defined in the PMMA resin with the e-beam unit of a scanning electron microscope. Proximity effects have to be considered, when very small structures are defined in e-beam lithography. Furthermore, large undercuts prevent the fabrication of small freestanding structures. Structures were designed almost an order of magnitude larger than the real final size and the undercut was exploited in the evaporation step in order to achieve small openings.

Next, the exposed PMMA resin is removed in the development step. Figure 2.7 shows a microscope image of the sample surface with two fields of masks after the

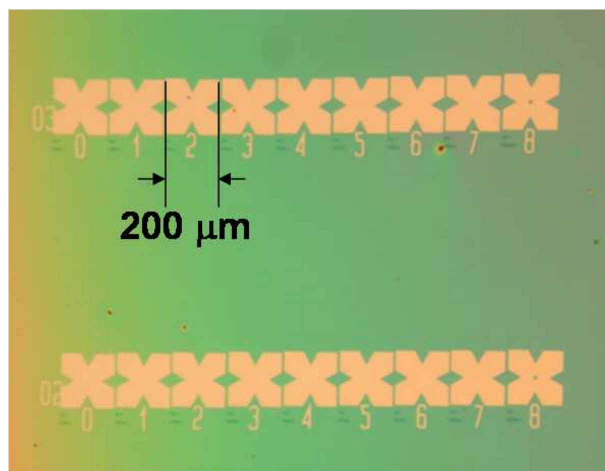

Figure 2.7: Optical microscope image of the sample surface after the development step. Green areas are unexposed and still covered with PMMA resin, yellow areas were exposed by the e-beam and left blank after development. The latter areas will be covered with aluminum afterwards. In the middle of the masks numbered 8 the resin post can be perceived, and will result in an 10 µm wide opening.

development and stop bath. The yellow area was exposed with the e-beam and is left blank after development, while the green area is still covered with PMMA resin. The resin posts in the middle of the 200 µm wide masks can be perceived in the masks number 8, and will result in openings of 10 µm. Afterwards, aluminum is deposited with a metal evaporating machine. Evaporation is not done vertically to the sample surface, but under an angle of 45°, taking advantage of the undercut of the resin posts. By evaporating 50 nm metal in each of the four steps from all sides of the square post, the sample surface is completely covered also below the undercut of the resin posts. Finally, in the lift-off step the remaining PMMA resin with the aluminum on top of it is removed. Figure 2.8 shows a scanning electron microscopy image of a completed mask with an opening with a lateral dimension of 250 nm. In each of the four evaporation steps, the larger top of the resin post left a rectangular shadow opposite the position of the metal source. Further details (times, chemicals) on the fabrication process are summarized in table 2.2. Several series of masks have been fabricated with the lateral size of the apertures varying from 10 down to 0.2 μm, allowing the optical access to a very reduced number of QDs. With these masks individual QDs can be investigated also in high density areas of the samples. With the highest densities of 10^{10} cm^{-2} the smallest apertures of 200 nm have about 40

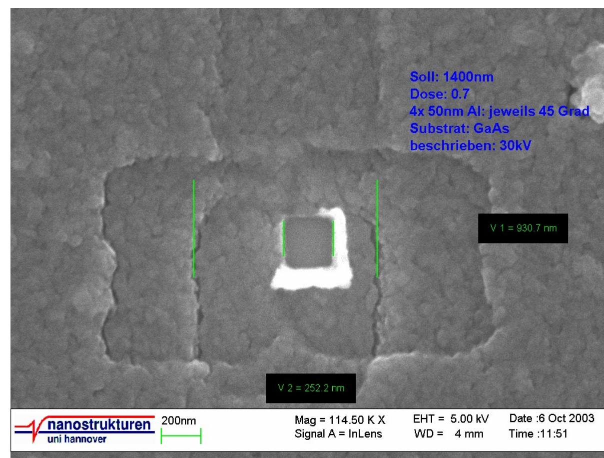

Figure 2.8: Scanning electron microscopy image of a completed mask with an opening of lateral dimension of 250 nm. Four layers of aluminum are evaporated in an angle of 45°with respect to the sample surface in order to exploit the undercut of the resin post. In each of the evaporation steps, the larger top of the resin post leaves the rectangular shadow opposite to the position of the metal source.

dots inside. Experiments have been performed in apertures down to 500 nm.

Chapter 3

Basic properties of InAs/AlAs QDs

Available data on *single* InAs/Al(Ga)As QDs are scarce in contrast to the widely studied In(Ga)As/(In)GaAs QDs. So far, most structural and optical investigations [1] realized on dot systems containing aluminum are done on high density samples probing therefore a large dot ensemble, where coupling effects play possibly an important role. Some of the previous results are given below:

(i) Morphology: Growth conditions for island formation (critical thickness, etc.) have been studied in situ by relection high-energy electron diffraction (RHEED) [29]. In and ex-situ structural (size, shape, composition) characterization has been realized by scanning microscope techniques as STM [24, 33], AFM [27–29], TEM [19, 20, 23, 25, 26, 30–32] and XSTM [33]. Some details are given in section 2.2.2.

(ii) Band structure and decay times: The main difference of the InAs/AlAs QD band structure compared to InAs/GaAs system is the indirect band gap of the AlAs barrier. Its influence on the optical properties has been addressed in several time-resolved measurements. It has been proposed that electrons confined in localized X-states of the matrix give rise to large decay times [36], whereas indirect intra-dot transitions are made responsible for varying decay times by other authors [35] As mentioned already, large decay times were observed and interpreted differently: They were interpreted as the spatial separation of charge carriers in high density samples [34]. Alternatively, electrons confined in localized X-states of the matrix were proposed [36]. An alternative explanation was attributed to the large dark-bright

[1] Other types of spectroscopy include, for example, transport spectroscopy on InAs/AlAs/GaAs tunneling diode structures, allowing the access to single QDs, too [27, 76].

exciton splittings due to increased electron-hole exchange interaction [77]. Indirect intra-dot transitions were made responsible for varying decay times [35].

(iii) Blue-shift: Several macro-PL studies [20–23, 25, 27, 28, 39] emphasize the blue-shifted emission energy into the visible spectral range, but no sharp peaks revealing the 0D-density-of-states of the dot are shown. However, PL of QD ensembles with a small number of AlInAs/AlGaAs QDs in mesa structures exhibit sharp peaks of less than 0.4 meV width at 1.88 eV emission energy [16], but properties of individual dots are not investigated.

(iv) Dot coupling effects: Several papers investigate coupling effects in high dot density samples by PL and time-resolved PL. In high density InAs/AlAs QD samples a temperature-induced red-shift of the macro PL stronger than of the InAs QD band gap dependence is attributed to activation-energy differences between QDs of different size [23]. Alternatively the anomalous redshift is explained by carrier thermal coupling and redistribution among QD ground and excited states [25]. In this context also large decay times were observed and attributed to the spatial separation of charge carriers [34].

(v) Phonons: Vibrational properties have been studied on dot ensembles with varying composition by Raman and IR spectroscopy [30–32, 37, 78]. Barrier and QD InAs-like, AlAs- like, and interface optical phonon modes were identified and deviations from the bulk phonon frequencies were explained by strain-induced and confinement-induced shifts of the phonon energies [32, 37, 78].

(vi) Exciton-phonon coupling: PLE measurements on a AlInAs/AlGaAs QD ensemble [38] and InAs/AlAs QDs [39] reveal exciton-phonon coupling involving InAs- and AlAs-like LO and IF phonon modes due to resonant phonon relaxation.

(vii) Single dots: Regarding micro-PL on single QDs containing aluminum in the barrier or the dot, only very little work has been realized. Sharp PL lines around 1.88 eV were observed from small ensembles of AlInAs/AlGaAs QDs [16]. Single peaks at high emission energies around 1.8-1.9 eV are attributed to single QD exciton emission. However, the observed peaks exhibit a very large width of about 15 meV [18, 19]. Furthermore, the exciton fine-structure has been investigated in InAs/$Al_{0.6}Ga_{0.4}As$ QDs (1.5-1.8 eV) and show very large splittings up to 1 meV [17], an aspect that is discussed in more detail in chapter 3.7 and chapter 4.

The above list demonstrates that dots embedded in barriers containing aluminium

exhibit interesting and new features, but results are still controversial. In these experiments often high density samples were investigated, which exhibit coupling effects. Above all, very scarce data are available on single dots, which could lead to a deeper understanding of the specific properties of InAs/AlAs dots.

In order to obtain information on the basic properties of InAs dots embedded in an AlAs matrix, various types of experiments were carried out in the present thesis and their results were compared to the information available for dots in GaAs barriers. This chapter begins with three sections on macro-PL measurements, micro-PL of the ensemble and micro-PL of a single QD. The following sections show the dependencies of the PL spectra of single QDs on the temperature, excitation intensity, polarization, magnetic field and time.

Apart from gaining information on basic properties, these experiments provide tools necessary for further investigation of the dots, principally the identification of the transitions of a single QD. The micro-PL spectra usually exhibit several peaks, even if small openings in the mask are used or regions with a low QD density are investigated. Not all of them are necessarily from different dots, as the emission of the exciton, biexciton, charged exciton complexes and excited states of a QD are usually observed in a PL spectrum. A common procedure to identify exciton and biexciton transitions belonging to the same QD consists of three criteria [79]: First, peaks belonging to a single QD are identified by their spectral jitter pattern, what is treated in section 3.5. Secondly, polarized spectra allow the assignment of emission lines of exciton and biexciton transitions due to the fine-structure splitting of the exciton state, see section 3.7. Thirdly, power dependent measurements allow to distinguish between exciton and biexciton peaks; details are given in section 3.6.

3.1 Macro-photoluminescence

Macro-photoluminescence spectra of both samples (A and B, see section 2.2.2) for various positions across the samples are shown in Figure 3.1 (for details on the macro-PL setup, see chapter 2.1). The temperature was $T = 10$ K and excitation power and energy of a few mW and 2.41 eV, respectively. The position on the sample corresponds to varying InAs coverage due to asymmetric growth conditions (see chapter 2.2.2). Both QD samples emit at energies of around 1.7 eV, which are higher than those

of the widely studied InAs/GaAs system. The inhomogeneous broadening of about 100 meV is large compared to the typical broadening of 30-50 meV for (annealed) InAs/GaAs QDs [43].

The peaks at 2.0 eV, shown in the insets of Figure 3.1 are the PL emission from the wetting layer states. The doublet structure of the peak is due to monolayer fluctuations in the wetting layer (WL) thickness. The luminescence intensity of these peaks is stronger in the low dot density region of the sample, and cannot be observed in areas of high dot density. This demonstrates that charge carriers relax efficiently into the QD states from the WL states or the AlAs barrier bands (X band for electrons).

For both samples A ($T_S = 530$ ℃) and B ($T_S = 500$ ℃) the PL intensity increases as the spot position is varied across the wafer, corresponding to increasing QD density. Also the PL peak shifts to lower energies across the sample, corresponding to an increasing QD size for increasing InAs coverage [67]. Comparing the macro PL of both samples one notes an additional blue-shift for sample A, which is attributed partly to a decrease of the average QD height with increasing growth temperature [67]. QDs grown at higher temperatures can contain a higher concentration of aluminum [19], giving rise to an extra blue-shift. The blue-shift is increased by growth interruption indicating a slow QD formation on AlAs [19, 29]. The principal origin of the extra blue-shift for sample A is therefore assigned to a higher aluminum content due to an increased aluminum and indium diffusion at the interface for higher growth temperatures [67]. Intermixing for high growth temperatures has been reported also for InAs/GaAs QDs [80, 81].

Emission in the visible region has been reported previously for QD systems containing aluminum [22, 23]. Among the various combinations of the In(Al)As/(Al)GaAs system [20] investigated, visible emission is achieved already with InAs/AlAs QDs, but the PL emission energy is further increased for InAlAs/AlGaAs and InAlAs/AlAs QDs. The latter combinations demonstrate that strong confinement leads to higher quantization of the states and therefore higher emission energies. Besides, aluminum incorporation into the dot itself increases the QD gap energy, although simultaneously lowers the confining potential compared to the InAs/AlAs system [2]. Emission of InAs/GaAs QDs with a thin AlAs cap layer [21] grown at low temperature is also

[2]The composition dependent InAlAs E_0 band gap energy ($T = 300$ K) is given by [82] $E_0(x) = 0.37 + 1.91(1-x) + 0.74(1-x)^2$. Therefore, already 10 % aluminum concentration in the InAs QD will blue-shift the emission energy about 200 meV.

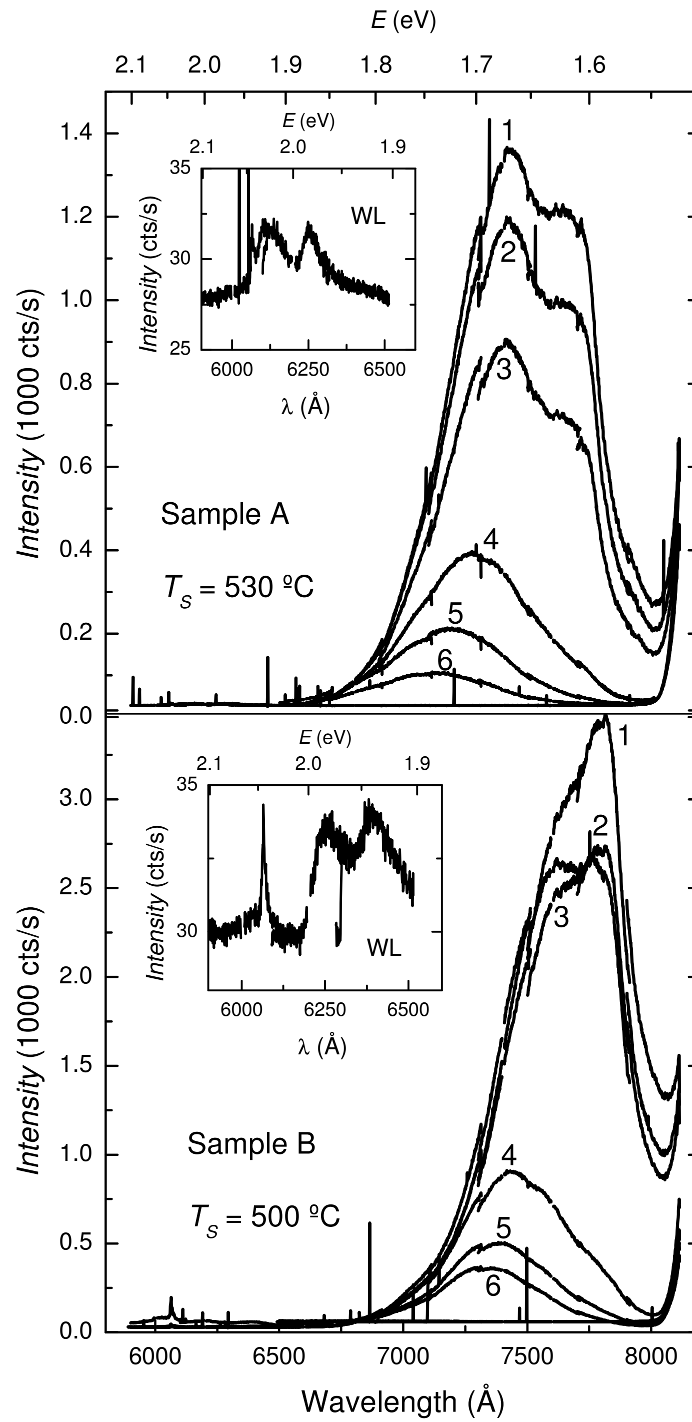

Figure 3.1: Macro-photoluminescence spectra of sample A (top panel) and B (bottom panel) are shown for various positions across the wafer.

blue-shifted due to the increased top potential barrier.

In summary, the macro-PL emission of both studied samples is in the visible spectral range due to increased confining potential barriers and aluminum incorporation into the dot, increasing the dot band gap. The latter conclusion is supported by the results of chapter 5.1 where intermixing is estimated from the frequency of the QD phonon modes coupled to the exciton state. The wetting layer states are observed around 2 eV, a critical value for efficient free carrier generation, as shown in chapter 5.3 in the context of screening of the exciton-acoustic phonon interaction. Sample A was selected for single dot spectroscopy, because of the low dot density for low InAs coverage. Additionally metal masks were produced an top of this sample (see chapter 2.3), restricting optical access to only a few dots even in high density areas. These masks serve also as markers to facilitate spot relocation at the same QD after misalignment (vibrations, temperature drift, etc.) or after a repeated cool down cycling.

3.2 Micro-photoluminescence of the quantum dot ensemble

A micro-photoluminescence study of the QD ensemble emitting over a large spectral range is presented in this section, which permits an important insight into the specific electronic structure of the InAs/AlAs QD system. The energy range covered by the emission of the ensemble of dots is interpreted as equivalent to a variation in size, at least in first approximation, as shape and composition fluctuations also change the emission energy. Below about 1.8 eV the PL spectra exhibit typical sharp lines, corresponding to transitions between fully confined states. Above this energy the sharp peaks disappear and a continuous spectrum is observed. This is interpreted as a quantum confinement driven type-I - type-II band alignment transition with a simultaneous direct-indirect transition in reciprocal space. For small dots electrons are delocalized in the X band of the AlAs matrix and recombine with holes confined in the InAs QD. [3]

[3] Part of these results were published in Phys. Rev. B 71, 81302(R) (2005) and AIP Conf. Proc. 772, 715 (2005)

3.2.1 Introduction

The indirect nature of the AlAs band gap has a strong influence on the optical properties of the InAs/AlAs QD system. For example, long decay times due to carrier separation via AlAs X-band scattering [34] or due to localized X-band states [36] were discussed recently. For InAs/AlGaAs QDs [17] efficient electron capture due to resonant X-band and wetting layer states are made responsible for the appearance of negatively charged excitons for non-resonant excitation. Also, transport spectroscopy on InAs QDs embedded in AlAs/GaAs resonant tunneling diode structures [76] exhibit features due to the AlAs X-band.

However, the details of the electronic properties of InAs/AlAs hetero- and nanostructures are still investigated experimentally [19, 83] and theoretically [19, 84]. The case is especially complicated for quantum dots with their complex strain distributions, as well poorly known shape and composition variations. Two questions have to be addressed regarding the electronic structure of the InAs/AlAs nanostructures: (i) the type of band alignment and (ii) the symmetry of the states involved in the transitions. Both the band lineup and the state symmetry have consequences for the optical efficiency as symmetry of the states and wave function overlap (localization of the carriers) determine the oscillator strength.

(i) The type of band alignment at the interface of two different semiconductors depends on the materials, strain, external fields (pressure, electric field) and the size of the structure (confinement-driven band gap increase). The band alignment determines the localization of the CB and VB charge carriers: If the band alignment of the materials is straddled (type I) then the electrons and holes are confined in the same space. For staggered band lineup (type II) charge carriers in CB and VB are spatially separated.

(ii) The character (Γ, X or L-like) of the states can also depend on the QD size, strain and composition, and is still investigated. The VB maximum (VBM) is always Γ-like, but the CB minimum (CBM) may also be X or L-like, in which case the lowest energy transition is indirect in reciprocal space.

Combining both aspects (band alignments and character of the states) leads to different possible situations for QDs:

(a) Direct type-I QDs: Both the electron (Γ-like CBM) and the hole are localized inside the QD. The commonly studied InAs/GaAs QD system is a typical example.

(b) Indirect type-I QDs: The QD lowest CB state is originated from is X (or L) CBM. Then the transition is spatially direct but indirect in k-space. Such a situation is theoretically predicted for freestanding GaAs nanocrystals [84, 85]. For InAs/AlAs self-assembled QDs [19] this type of band structure has been proposed, too.
(c) Direct type-II QDs: The electrons and holes are spatially separated in Γ-like states. Type-II excitons in indirect band gap materials have been observed in antimony based QDs like AlSb/GaAs [69, 70], GaSb/GaAs [68], and InSb/GaAs QDs [69, 70].
(d) Indirect type-II QDs: Indirect transitions in real and reciprocal space have been investigated theoretically [84] in GaAs/AlGaAs nanocrystals and experimentally InAlAs/AlGaAs self-assembled QDs [83]. For the latter QDs the quantum confinement effect is strong enough to push the the Γ-like electron QD state above the matrix X-type CBM. This is verified by excitation power and pressure dependent PL measurements.
(e) Other, special situations can occur: Delocalized electrons, with a resonance at the QD are predicted for GaAs nanocrystals [86], and InAs/AlAs QDs [19].

A transition from one of the above mentioned types to another can occur in the same material system by varying an external parameter. Such level-crossings are known in pressure induced shifts for several material systems. For example, for bulk GaAs the Γ-X crossing, corresponding to a direct-indirect transition in k-space has been investigated theoretically [87] and experimentally. In the case of quantum dots, real and/or reciprocal space direct-indirect transitions are driven by the size of the structure, but also strain can be significant. The quantum-confinement shift depends on the effective mass. The X band electron effective mass is larger than the Γ-band mass and this results in the crossing of the Γ and X states for decreasing QD size, corresponding to a direct-indirect (Γ-X) transition. A spatial direct-indirect transition (type I-type II transition) occurs when the QD level is shifted by quantum confinement above the CBM of the matrix.

Figure 3.2 gives a rough idea of the size dependence of the band structure of the presently investigated InAs/AlAs QDs. On the left panel the energies of the InAs CB states $E_\Gamma(r)$, $E_X(r)$ and VB state $E_{VB}(r)$ are shown as a function of the dot size. They are modeled by a 1D infinite quantum well [88]: $E_\Gamma(r) = E_\Gamma + \hbar^2\pi^2/2m_\Gamma r^2$,

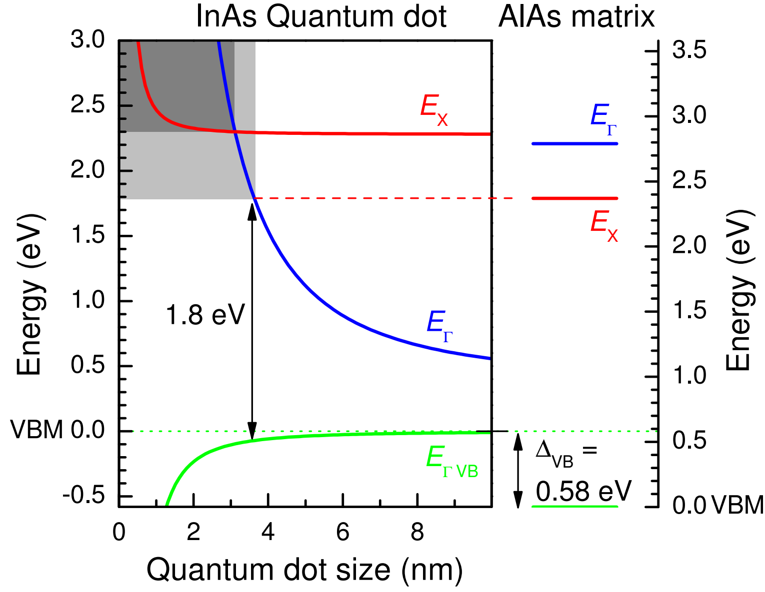

Figure 3.2: Left: The energy of the relevant CB and VB states of the InAs/AlAs QD system is shown as a function of the QD size. Right: Quantum confinement in small QD shifts the QD Γ state above the AlAs X conduction band valley.

$E_X(r) = E_{X^+} + \hbar^2\pi^2/2m_X r^2$, $E_{VB}(r) = E_{VB} + \hbar^2\pi^2/2m_{VB}r^2$. $E_\Gamma(r)$, E_X , E_{VB} are the bulk values for the band edges, r is the QD size, and m_i the effective masses. The quantum confinement effect is modeled by the second terms, i.e. by the ground states of a infinitely high 1D quantum well potential. The right panel shows bulk values of the AlAs CB and VB valleys. The VB offset of the InAs/AlAs heterojunction is still controversial; here the unstrained VB offset value of $\Delta_{\mathrm{VBO,InAs/AlAs}} = 0.58$ eV [89] is used. For decreasing QD size the quantum confinement effect pushes the Γ-state above the AlAs X CB edge at a QD height of 3.7 nm (light gray area). This type-I - type-II transition takes place together with a Γ-X crossover, as electrons will be localized in the AlAs X band, i.e. the dot becomes indirect both in real and reciprocal space. Within this very simple model one can expect a quantum confinement driven direct-indirect (in real and reciprocal space) transition for decreasing QD size for dots emitting around 1.8 eV. An intra-dot level crossing occurs for even smaller QDs at an emission energy of about 2.4 eV (dark gray area). This transition is irrelevant here since electrons scatter already to the lower lying X band edge. Detailed calculations for InAs/AlAs QDs have been realized [19, 35].

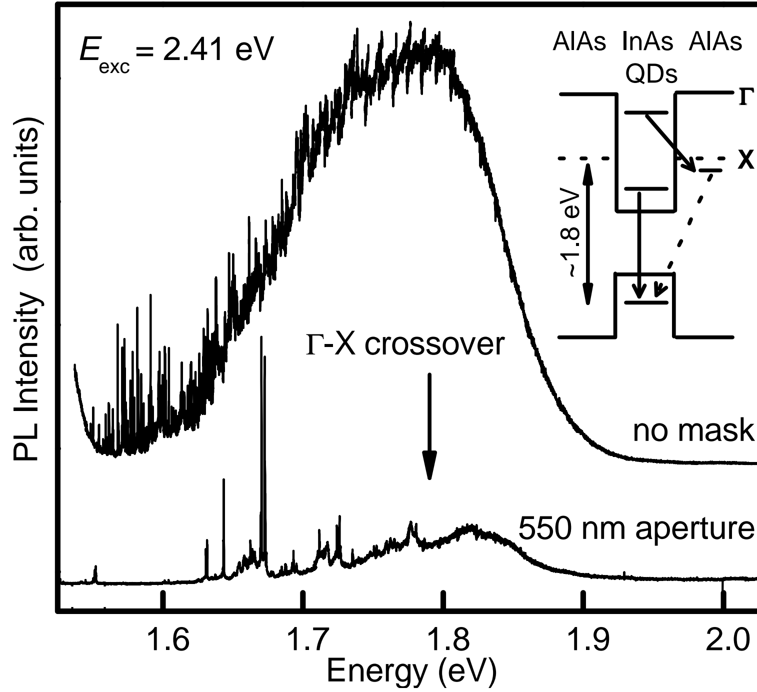

Figure 3.3: PL with and without mask. PL from confined states is observed only below 1.8 eV as a consequence of the $\Gamma - X$ crossover with the AlAs barrier. Inset: Band sketch illustrating transitions between fully confined QD states and recombination of electrons scattered into the AlAs X band.

3.2.2 Results

Micro-PL measurements on a QD ensemble (in the high dot density region of the sample) were realized. For details on the micro-PL setup, see chapter 2.1. The spectra are taken at a temperature of $T = 8$ K, excitation power of about 1 mW and excitation energy of 2.41 eV. In Figure 3.3 spectra are shown for a large ensemble of QDs taken outside the metal mask (top curve) and for smaller number of QDs through one of the 550 nm apertures in the mask (bottom curve). In contrast to the macro-PL spectra shown in the previous section, one observes sharp peaks corresponding to totally confined states in individual QDs below 1.8 eV, even in the spectrum taken outside the mask due to the high spatial resolution of the microscope setup. This spectrum contains the emission of around one thousand QDs.

For all PL spectra the emission above 1.8 eV is continuous and sharp peaks cannot be observed even in the high energy tail, where only a small number of dots should emit. A continuous PL emission indicates that electrons (or holes) are delocalized.

In the case of high QD density one might observe an apparent continuous spectrum at the center of the macro photoluminescence emission due to the overlapping PL peaks. But in this case individual peaks should be observed also at the high energy tail, as occurs at the low energy tail. The PL spectra shown in Figure 3.3 *only* show sharp peaks in the low energy tail, disproving the existence of fully confined states at high energies. Furthermore, at low QD numbers (lower curves) the continuous band does not disappear. This indicates that in this spectral region at least one of the charge carriers is not fully confined. The inset in Figure 3.3 shows a sketch of the band alignment and the PL transitions for large dots (solid arrow), where the confined state is below the conduction band minimum of the AlAs barrier (at the X point of the Brillouin zone). As discussed in the introduction, decreasing the QD size originates a quantum-confinement driven type I - type II transition: In smaller dots, the higher confinement energy brings the state above the CB minimum of the barrier and consequently, the electron is no longer confined inside the dot, but spatially separated from the hole. Further, the CB minimum of the AlAs barrier has X symmetry, i.e. the transition becomes also indirect in reciprocal space. Recombination in this case involves a dispersive electron state and no sharp peaks are visible (dashed arrow) in the spectral region above 1.8 eV.

Thus, the single dot emission in the visible spectral range from 1.55 up to 1.8 eV is limited by the crossover. The crossover energy value of 1.8 eV is determined, by the strain in the InAs dot, the band offsets between AlAs and strained InAs, the confinement energy of electrons and holes, as well as by some possible diffusion of aluminum into the dot and indium into the barrier. The present suggested explanation rises the question of why peaks corresponding to fully confined states have been observed at higher energies near 1.9 eV, as reported by other authors for QD systems containing aluminum:

-(i) PL spectra of few $Al_{.45}In_{.55}As/Al_{.35}Ga_{.65}As$ QDs in mesa structures exhibit sharp peaks of less than 0.4 meV width at 1.88 eV emission energy [16]. In this case, the emission energy is principally blue-shifted due to the high Al content increasing the QD band gap ($Al_{.45}In_{.55}As$ gap = 1.38 eV), and not due to confinement, as in our case. Besides, the barrier band gap is direct for the 0.35 Al concentration (crossover at x=0.405 for 295 K). Electron states will be fully confined inside the dot up to the edge of the barrier (band gap near 1.98 eV at 10 K). Type-II alignment is impossible

in this system.

-(ii) Single QD peaks at high emission energies around 1.8-1.9 eV were observed for QDs with pure AlAs barriers [18] and attributed to single QD exciton emission. However, the observed peaks are particularly broad with widths of about 15 meV at 60 K [18, 19]. These authors [19] investigated also theoretically the electronic structure in similar InAs/AlAs QDs but question a type I - type II transition as it is suggested here. They propose that decreasing QD size leads to a direct - indirect transformation of the lowest lying conduction band state within the QD, but keeping up the type I band alignment [19]. Furthermore, they propose that the continuous band is due to the overlap of broad bands of a few QDs with a indirect band gap (X-hh intra QD transitions). However, their calculations do not contradict our results but indeed do corroborate the interpretation given above. Apart from the already given arguments for a type I - type II transition (sharp peaks only at the low energy tail, continuous spectrum and no sharp peaks at the high energy tail), their calculations (Figure 5 of [19]) indicate that for 1.8 eV emission energy, the X states of the QD and the X minimum of AlAs conduction band are practically degenerate. Therefore the real presence of bound X states is not evident, because even small changes due to the inclusion of exciton corrections and a more realistic composition distribution could easily produce a type II alignment for the X band. One possibility for X-hh intradot transitions could perhaps be the comparatively broad peaks observed in the lower curve of Figure 3.3 (just below 1.8 eV) near the continuum onset. If so, the origin of the broadening could be due to hybridization with the barrier continuum, but this is just a speculation. All in all, the calculations of Ref. [19] do support the conclusion that above 1.8 eV transitions occur between extended electron states and localized holes in InAs/AlAs QDs.

In summary, the micro-PL spectra of QD ensembles over a large spectral range reveal an energy threshold at 1.8 eV for sharp emission lines between fully confined states. Above this energy, $\Gamma - X$ scattering of the electron into the barrier due to type-II alignment results in a continuous emission spectrum.

3.3 Micro-photoluminescence of single quantum dots

Properties derived from experiments on QD ensembles are averaged and obscured due to the inhomogeneous size and composition broadening. Furthermore, many of the experiments on InAs/AlAs QDs carried out so far [23, 34] were realized with samples grown at low temperature (around $T_S = 500$ ℃) leading to a high density of small QDs. Therefore enhanced coupling between neighboring QDs has to be considered. In order to obtain a detailed understanding of the electronic and vibrational properties, *single* dot spectroscopy performed on *low density* samples is indispensable. From now on, all the work shown in the present thesis refers to the sample grown at 530 ℃ (sample A, see details in chapter 2.2.2), and most of the single dot spectra were obtained in the low density region of the sample.

The microscope objective is mounted on a motor-driven stage that allows to scan automatically the sample surface in the search of dots. Figure 3.4 shows the intensity map of a 10 µm opening in the low QD density area. The abscissa is the emission energy. For each block the position of the microscope objective is shifted in the y-space direction. Inside a block each line corresponds to a displacement of the objective in the x-direction. [4] The map shows only few different QDs in the scanned spatial and spectral region. Several peaks might be from the same dot, when they appear together during the mapping.

The polarization-resolved micro-PL spectra of one of these dots (QD1) is shown in Figure 3.5. Temperature was 10 K, excitation energy 2.54 eV and excitation power is 1 mW. The spectrum exhibits only a few peaks, which belong to the same QD as verified by their jitter pattern, see sections 3.5. The doublets labeled X and XX are the emission of the neutral exciton and biexciton complexes, respectively. The identification of these peaks is done by their polarization and power dependence, (see sections 3.7 and 3.6, respectively). Electron-hole pairs are created in the wetting layer or the AlAs barrier (indirect gap, X-hh), which scatter into the dot forming an exciton and subsequently recombine radiatively, giving rise to the peak X. For larger excitation powers a second electron-hole pair with opposite spins for both charge carriers is captured before the first one recombines radiatively. In a sequential process first this biexciton complex decays into an exciton, which recombines afterwards. For increasing excitation power further multi-excitons are created, but due to Pauli-

[4] 4D-plot: PL Intensity versus x, y, and energy.

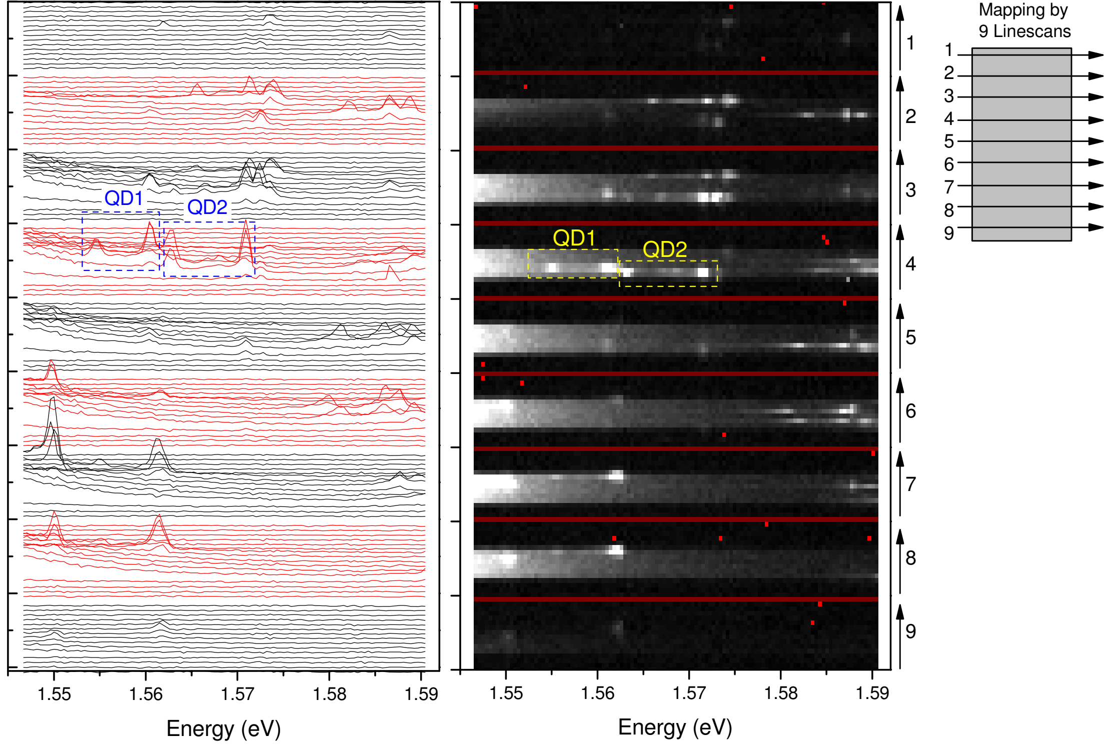

Figure 3.4: Photoluminescence mapping of a 10x10 μm square opening. The scheme on the right shows the scanning sequence of the opening. Left panel: Each block shows PL spectra as a function of photon energy and x-position along a line across the opening. Blocks 1-9 correspond to a displacement along the y-position. Right panel: The PL intensity from the spectra of the left panel is shown in a gray scale plot.

blocking they fill excited states, also named shells in analogy with the energy structure of atoms. More details on the power-dependence are given in section 3.6. Other peaks in the spectrum are attributed to positively (X^+) or negatively (X^-) charged excitons. In the PL spectra neutral and charged exciton complexes can appear simultaneously, due to the random electron and hole capture processes from the surrounding material: The quantum dot may contain either a neutral exciton or an electron-hole pair with an additional electron or hole. After the recombination of the electron-hole pair the dot is left with the excess carrier, which can either tunnel out of the dot, or form again an exciton if another carrier of opposite sign is captured by the QD. In continuous-wave measurements the PL spectra are averaged over time and therefore exhibit lines that represent emission from different initial charge states of the dot.

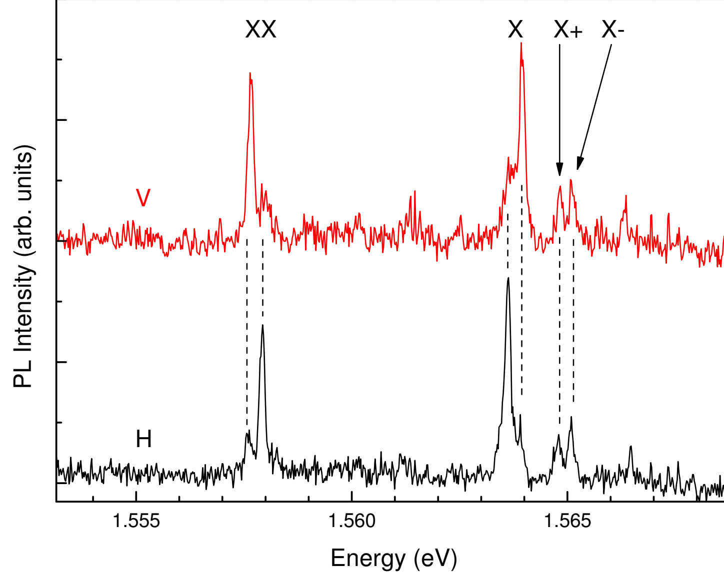

Figure 3.5: Polarization-resolved photoluminescence spectra of a single QD. The peaks labeled X, XX, X^+ and X^- are attributed to the exciton, biexciton, positively charged trion and negatively charge trion emission, respectively.

Differences in the charging mechanisms for electrons and holes are responsible for the different observed initial charge states of the QD. In general, the capture of carriers is a diffusion process, which depends on the effective mass and the excess energy of the photo-created charge carriers, resulting in different populations of the dot, (see for example the studies on GaAs QWs [90] or InAs QDs [91]). For indirect AlGaAs barriers it was proposed that a negatively charged exciton is more likely than an positively charged one, due to the indirect character of the barrier, which provides a rapid X-Γ transfer only for electrons but not for holes [17]. This was verified by quasi-resonant excitation below the X minimum, where the X^- peak disappears. In the present case, two unpolarized lines (X^+, X^- in Figure 3.5) shifted to higher energies with respect to the exciton transition energy are observed. They belong to the same QD as shown by their jitter pattern (see section 3.5). The one at higher energy disappears on lowering the excitation energy below the AlAs X-band (quasi-resonant excitation). It is therefore tentatively assigned to the negatively charged exciton X^-. The other peak does not disappear and is tentatively attributed to a positively charged exciton X^+. There are two possible objections to this assignment: First, it is unclear, which details of the charging mechanisms and excitation conditions would

favour the formation of a positive trion compared to a negative one for quasi-resonant excitation. Secondly, the negatively charged exciton is usually reported to be shifted to lower energies with respect to the exciton. However, recombination energies of the different complexes depend sensitively on size, shape and composition. Theoretical studies on InGaAs/GaAs QDs [92] demonstrate that for decreasing QD height the X^- recombination energy red-shifts strongly, while the X^+ energy blue-shifts. As a result X^- can appear at higher energy than X^+. Our dot emits at the very low-energy tail of the ensemble PL, therefore it is one of the larger ones, which have generally larger vertical to lateral aspect ratios [24, 73] This corresponds to an X^- emitting at higher energy than X^+ [92]. To the best of my knowledge there are no theoretical studies on recombination and binding energies of exciton complexes and their dependence on size, shape and composition for dot systems containing aluminum, so that the cited work only gives a rough qualitative idea about the trends. Altogether, the large size of the dot, the unpolarized emission, and the disappearance for quasi-resonant excitation point to a X^- emission for the highest energy peak. The other unpolarized peak may be due to the emission from the X^+ complex, although these assignments are not conclusive.

3.4 Temperature dependence

Temperature effects include spectral shifts of the dot PL due to the expansion of the crystal lattice, quenching of the luminescence due to scattering of charge carriers into higher energy states and activation of non-radiative recombination paths. However, special interest is addressed to the width and shape of the emission, as it gives information about the dephasing processes of the confined exciton. The understanding and control of phase coherence is of fundamental importance for the development of future quantum devices, as it determines the time scale of coherent logic operations.

Strong red-shifts are observed in temperature dependent macro-PL studies for temperatures above about 80 K. They are attributed to differences in the activation energy for QDs of different size [23]. Alternatively, thermally excited charge carrier transfer between coupled QDs in high density samples has been proposed as an explanation [25]. In high dot density samples thermally activated electron-hole separation due to electron transfer between neighboring QDs has been suggested to explain long

decay times, too [34]. In single dot spectroscopy, the main attention is directed to the temperature-induced broadening of the PL peak, or the evolution of the lineshape in general. The lineshape of the presently investigated InAs/AlAs QDs consists of a central narrow peak (the zero-phonon line, ZPL), broad wings and narrow sidebands. In this section, temperature dependent PL spectra of a single QD are presented, and the main attention is paid to the temperature-induced central ZPL broadening. Interactions with phonons are discussed in chapter 5. Broad wings and especially the narrow low-energy sidebands, are discussed in section 5.3.

The linewidth is given by several contributions corresponding to different dephasing processes. Two questions arise in this context: (A) What are the contributions to the ZPL width (dephasing processes) and (B) What is the physical origin of the temperature-induced broadening of the ZPL?

(A) Dephasing processes. The dephasing processes can involve [93] (i) change in the carrier occupation of the exciton state (also called inelastic scattering processes) and (ii) unchanged dot population, in which case they are named pure dephasing processes. (i) Inelastic scattering processes that involve a population change include the radiative recombination (which gives rise to the intrinsic, radiative lifetime limited, broadening), phonon-assisted transitions to the ground, excited, wetting layer, or other confined electronic states, as well phonon-assisted charge transfer to other QDs. (ii) Pure dephasing is introduced by the elastic phonon scattering, via virtual transitions, without population change. The fluctuating electrostatic environment also may introduce pure dephasing, if the fluctuations happen on a timescale shorter than the radiative lifetime (called motional narrowing regime) [94–96]. A slow varying environment (compared to lifetime) does not produce pure dephasing, but spectral wandering (jitter) increases the measured linewidth. This is known as dynamical broadening and depends on the integration time. These processes contribute to the ZPL broadening and may give rise to a non-Lorentzian lineshape.

(B) Thermal broadening. The temperature dependence of the QD-emission linewidth is qualitatively described in several studies by

$$\gamma(T) = \gamma_0 + a\, n_{ac} + b\, n_{LO}$$

, where γ_0 is the intrinsic lifetime-limited linewidth at zero-temperature, a and b are constants, $n_{ac} = 1/(exp(E_{ac}/k_BT) - 1) \approx k_BT/E_{ac}$ $(E_{ac} << k_BT)$ and

$n_{LO} = (exp(E_A/k_BT) - 1)$ are Bose-Einstein functions for the acoustic and optical phonons. However, this relation describes the homogeneous linewidth of bulk and QW emission, and relies on the existence of a continuum of electronic states subject to one-phonon processes [97]. Consequently, although experiments in QDs may exhibit similar temperature dependence, a direct comparison is not straightforward due to the lack of a continuum. The physical origin of the ZPL width in QD and its temperature dependence are not fully understood and are currently subject to controversy. Linear and non-linear temperature-induced broadening was reported in several studies, including time-resolved PL, Fourier-transform, four-wave-mixing, and micro-PL spectroscopy. A similar behavior is observed for a variety of systems, while different interpretations are given. Most values reported for the linear broadening coefficient are around 1 µeV/K typically for temperatures up to 50 K, while above 50 K usually an activated behavior is observed with activation energies near the LO phonon energies of the QD and matrix material. Some examples are give:

- For epitaxially grown ZnCdSe/ZnSe QDs ($a = 20$ μeV/K, $E_A = 26 - 28$ meV) [98, 99] the linear broadening is attributed to virtual emission and absorption of acoustic phonons coupled to the exciton state (this would mean pure dephasing) and activation energies are in the range of the CdSe LO mode.
- For CdSe/ZnSSe QDs ($a = 1.2$ μeV/K) [100] the smaller a compared to QWs is attributed to a reduced number of final states (thus implying inelastic scattering).
- For InAs/GaAs QDs in a field-effect structure ($a = 2 - 2.8$ μeV/K) [101] the linear behavior is attributed to the proximity of a continuum of states.
- For InAs/GaAs QDs ($a = 0.5 - 3.5$ μeV/K) increasing a is found for decreasing lateral mesa sizes from 5000 down to 200 nm [75]. The influence of the sidewalls on a is attributed to the interaction of confined excitons with phonons, whose lifetimes are given by scattering from nearby surfaces.
- For InAs/GaAs QD ($a = 3.5$ and 1.3 μeV/K) [95] changes in a for different cool down cycles are found and it is concluded that the decoherence dynamics giving rise to the ZPL width is governed by the carrier dynamics in the QD environment, i.e. by the interaction of phonons with carriers outside the dot.
- For InGaAs/GaAs QDs ($a = 0.5$ μeV/K) scattering of holes, which are energetically closely spaced, was proposed [102].
- For InGaAs QDs ($a = 0.12 - 2.1$ μeV/K and $a = 0.05 - 0.1$ μeV/K, $E_A =$

$21-30$ meV) [103, 104] both acoustic- and optical-phonon-assisted inelastic scattering into the WL band tail states is made responsible for the temperature dependence of the linewidth.

- For InAlGaAs QDs ($a = 0.5$ μeV/K, $E_A = 30...31$ meV) the linear term is attributed to inelastic acoustic phonon scattering and virtual acoustic phonon scattering within the exciton ground state (pure dephasing), while the activation behavior is attributed to LO phonon-assisted scattering of holes into the WL [105].
- For strain-free GaAs/AlGaAs QDs grown by modified droplet epitaxy ($a = 0.2 - 1.1$ μeV/K, $E_A = 35 - 38$ meV corresponding to the GaAs LO phonon) [106] the origin of the linear term is left open and temperature activated broadening is found to be independent of dot size and hence, of dot's electronic structure. This thermal broadening is attributed to pure dephasing by elastic LO phonon scattering, which does not depend on the exact electronic structure, and is regarded as the most likely processes for exciton decoherence.
- Similarly, for InAs QDs ($a = 0$, no linear term is found, $E_A = 37 - 38$ meV) [107] the temperature-broadening is not size dependent, i.e. the broadening cannot be attributed to a lifetime effect due to transition of an exciton state to another one with emission or absorption of an optical phonon. The authors attribute it then to pure dephasing.

3.4.1 Results

In Figure 3.6 micro-PL spectra of a single QD for temperatures from 10 up to 80 K are shown for constant excitation power about $P_0 = 0.5$ mW, except for the bottom spectrum ($T = 80$ K), which is taken at $4P_0$. The spectra are vertically shifted for clarity and the dashed lines indicate the baselines of the respective spectra. X, XX, X^+ and X^- are the exciton, biexciton and charged exciton complexes of an individual QD, respectively. This attribution is confirmed by the spectral jitter pattern, power and polarization dependence, as explained in sections 3.5, 3.6, and 3.7. X (QD2) is the exciton emission of a different QD.

With increasing temperature one observes that (i) the emission lines shift to lower energies, (ii) the PL intensity quenches at high temperatures, (iii) the narrow peaks (ZPLs) broaden, (iv) the broad wings at the low-energy side of the exciton (arrows 1) increases and also appears on the high energy side, and (v) a second low-energetic

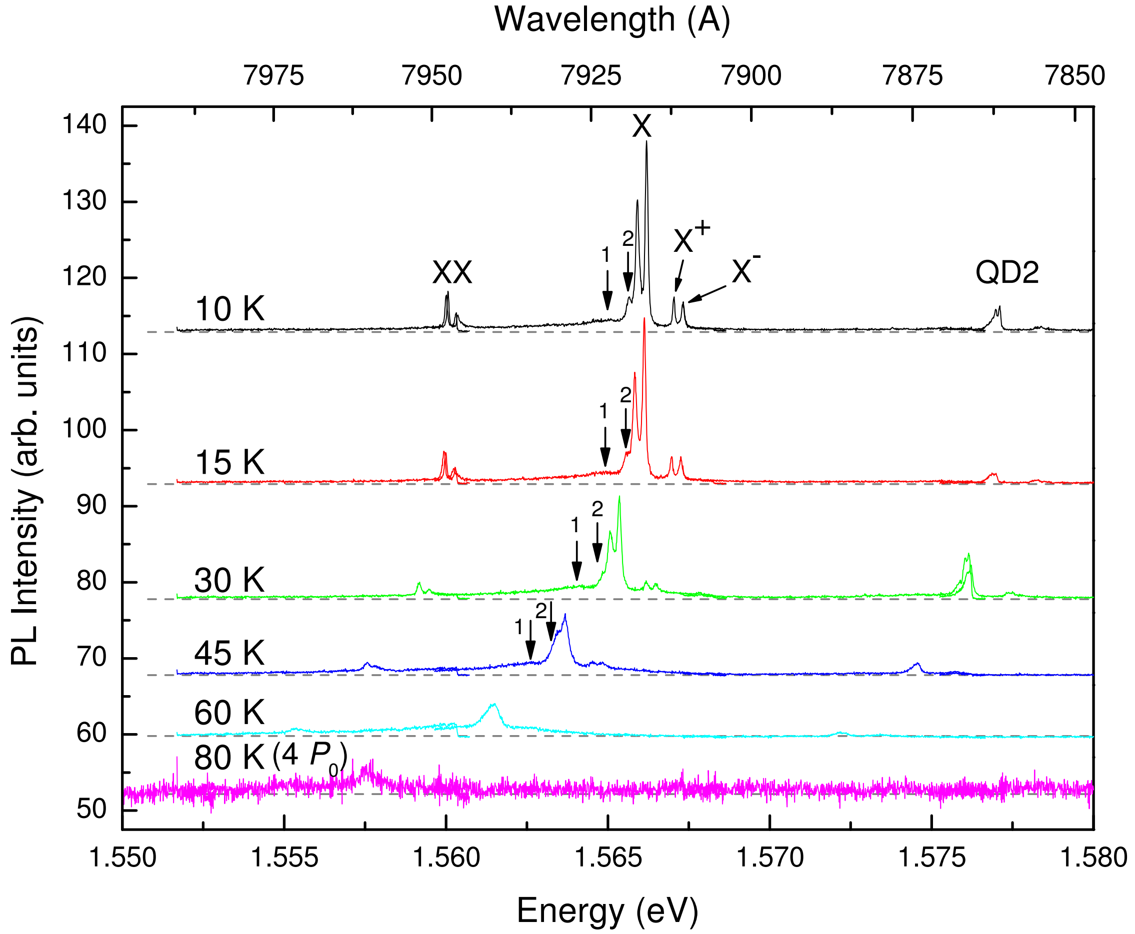

Figure 3.6: PL spectra of a single QD for a series of temperatures. Spectra are taken for constant excitation power P_0, except for the spectrum taken at 80 K and excited with $4P_0$. X, XX, X+ are the emission of the exciton, biexciton, charged exciton complexes of the same QD, respectively. For increasing temperature the emission peaks red-shift due to the band gap dependence on temperature. Further observations are described in the text.

sideband close to the exciton (arrows 2) similar but narrower also broadens and smears out. We analize now these experimental results in detail:

(i) Red-shift: In Figure 3.7 the energy of the center of the exciton doublet (circles) is shown versus the temperature. The temperature-induced red-shift can be explained by the decrease of the energy gap. The physical origins of that decrease are the expansion of the crystal lattice and the change of electron-phonon interactions [109]. An empirical relation for the temperature dependence of the band gap

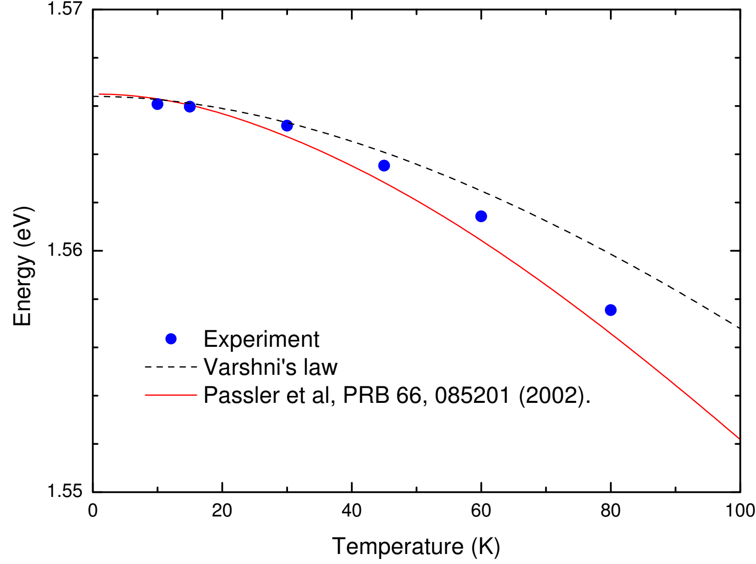

Figure 3.7: Energy of the exciton line of Figure 3.6 versus temperature. The dotted and straight lines describe the bulk band gap energy dependence of InAs by Varshni's law and the model of Ref. [108], respectively.

$E_g(T)$ is given [109] by

$$E_g(T) = E_g(0) - \alpha\ T^2/(T + \beta) \tag{3.1}$$

with the empirical parameters [110] $\alpha = 3.35\ 10^4$ eV/K and $\beta = 248$ K for InAs (Varshni's law). Here, the exciton transition energy $E_g(0) = 1.5664$ eV at zero-temperature has to be used, instead of the value for the bulk InAs band gap energy. The dotted line in Figure 3.7 shows the temperature dependence of the band gap described by the Varshni's law. Other models including interactions with phonons have been developed [108, 109] which describe more precisely the energy shift of the band gap at low temperatures. The gap energy is given by

$$\begin{aligned} E_g(T) = &\quad E_g(0) - \alpha\Theta[\tfrac{1-3\Delta^2}{\exp(2/\gamma(T))-1} + \tfrac{3}{2}\Delta^2(\sqrt[6]{1+\beta(T)} - 1)], \quad \text{with} \\ \gamma(T) = &\quad 2T/\Theta \quad \text{and} \\ \beta(T) = &\quad \tfrac{\pi^2}{3(1+\Delta^2)}\gamma^2(T) + \tfrac{3\Delta^2-1}{4}\gamma^3(T) + \tfrac{8}{3}\gamma^4(T) + \gamma^6(T). \end{aligned} \tag{3.2}$$

Θ is an effective average phonon temperature, Δ is related to the phonon disper-

sion and α is the high-temperature limiting magnitude of the slope [109]. This function is plotted in Figure 3.7 (straight line) using the parameters of bulk InAs $\alpha = 2.85 \times 10^{-4}$ eV/K, $\Theta = 147$ K, $\Delta = 0.68$, and the exciton emission energy of $E_g(0) = 1.567$ eV. Comparing both models with the experimental data, one observes that both Varnish's law (equation 3.1) and the equation 3.2 roughly reproduce the experimental trend. However, equation 3.2 describes slightly better the temperature-induced shift of the exciton peak. Deviations could be partly due to a difference in the band gap dependence of the dot and barrier material, what results in a temperature-dependent confinement potential. However, this effect is expected to be small, as the temperature dependence of the band gap of InAs and AlAs (AlAs, indirect gap: $\alpha = 3.6 \times 10^{-4}$ eV/K, $\beta = 204$ K [111]) are very similar. For strain-free GaAs/AlGaAs QDs [106] no deviations from the bulk band-gap temperature dependence are observed. However, in another study [112] deviations from bulk behavior are found and related to size-dependent renormalization of the band gap energy by electron-phonon interaction.

(ii) PL intensity quenching: The PL intensity of the QD quenches for temperatures around 80 K. Quenching is generally attributed to thermal carrier escape out of the dot into the WL and barrier states, and to non-radiative recombination centers as defects [113]. Additionally, for increasing temperature phonon-assisted optical transitions dominate progressively the lineshape and lead to a reduction of the ZPL intensity (see also iv and v).

(iii) ZPL broadening: The lineshape of the exciton emission consists of a narrow zero-phonon line, broad wings and in the presently studied dots also of narrow sidebands. The details of the exciton ZPLs are shown in Figure 3.8 for varying temperature from 10 to 60 K. The upper parts of the narrow ZPLs were fitted to double Gaussians for the lowest three temperatures (10, 15, and 30 K). For the lowest temperature the ZPL width is 90 µeV. The right bottom panel of Figure 3.8 shows the peak width of the Gaussian peaks (both peakwidths are supposed to be equal). The width of the Gaussian peaks was linearly extrapolated for the higher temperatures (45 and 60 K, circles) and corresponding Gaussian peaks were plotted in the PL spectra for 45 and 60 K. The linear extrapolation is justified by the above cited reports [75, 95, 98–107] on self-assembled QDs, where linear ZPL-broadening is usually observed in a similar temperature range. It is therefore reasonable to conclude that

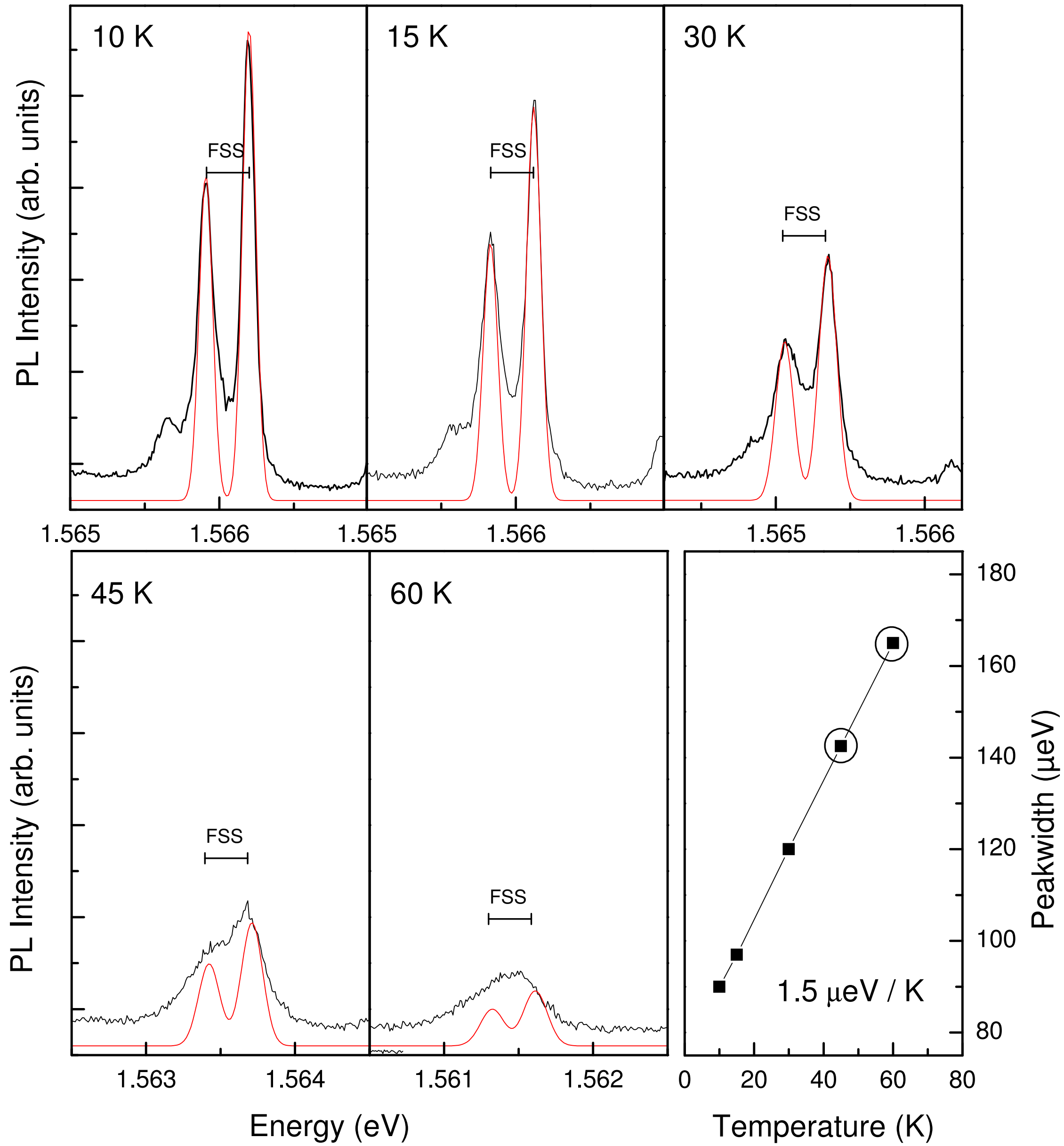

Figure 3.8: (a)-(e) Detail of the PL spectra of the exciton doublet (see Figure 3.6) for various temperatures. Gaussian double peaks are plotted at the position of the ZPLs. The bottom right panel shows the width of the Gaussian peaks in function of the temperature.

for the investigated InAs/AlAs QDs the linear thermal broadening factor is around $a = 1.5$ µeV/K. This is in the range of the values (but slightly higher) cited above.

A possible explanation of this difference is the small distance (30 nm) of the dots from the sample surface: A study on InAs/GaAs QDs [75] showed that scattering of phonons from the lateral sidewalls influences the temperature dependence of the zero-phonon linewidth and is relevant for mesa sizes up to a few µm. For large mesa sizes > 1000 nm the scattering from the smoother top surface located at 100 nm dominates, and gives a minimum value of $a = 0.5$ μeV/K. Since in the present case the dot is much closer to the surface, a larger a can be expected. Other studies relate the distance of the free surfaces to the dot with the linewidth and attribute the effect to spectral jitter: Both the distance from sample surface in the case of natural QDs [114] and the mesa size of InGaAs/GaAs QD samples [74] influence the linewidths. Generally there is a trend of larger a for large linewidths. Altogether, the linewidths and their temperature-dependence do show similarities to the cited systems, but the detailed understanding of the physical origin needs further investigation.

(iv) Broad wings: The broad wings at the low-energy side of the exciton (arrow 1 in Figure 3.6) increases and also appears on the high energy side when the temperature is increased. At the same time the ZPL loses weight compared to the wings. These wings are attributed to the coupling of the exciton to acoustic phonons by the deformation potential mechanism. Similar wings are often observed in single QDs, and are discussed together with the narrow sidebands (next paragraph) in section 5.3.

(v) Narrow sidebands: The narrow, low-energy sideband close to the exciton (arrow 2 in Figure 3.6) broadens and smears out with increasing temperature. In section 5.3 it is demonstrated that this feature is due to the interaction of the QD exciton with acoustic phonons via the piezoelectric coupling mechanism.

In summary, the temperature dependent spectra show a redshift of the emission peaks that follows the bulk band gap dependence. In the investigated temperature range a linear linewidth broadening of $a = 1.5$ μeV/K is found, similar to values of In(Ga)As/GaAs QDs. Broad and narrow low-energy acoustic phonon wings gain weight on increasing the temperature and will be further discussed in section 5.3.

3.5 Time evolution

Although solid-state QDs are often considered as artificial atoms due to their delta-like density of states, the comparison is rather inaccurate. Apart from the differences

in size scale and confining potential, atoms are structureless, usually isolated objects, whereas dots are nanocrystals embedded in a surrounding crystalline matrix. Both dot and barrier crystals exhibit elementary excitations other than the QD exciton, which may couple to it. The interaction of the confined exciton with the environment gives rise to phenomena without an analogy in atomic physics. The QD exciton can interact with other elementary excitations, like optical and acoustical phonons, both discussed in chapter 5. This section comments on the influence of surrounding charges or defects on the QD states, which leads to spectral shifts of the emission peaks over time. The specificity of the spectral jitter pattern for each individual dot is used in the present thesis for the unambiguous identification of emission lines belonging the same single QD [79].

Various phenomena observed in time-resolved spectra for different systems are related to random changes in the PL emission energy or intensity: Spectral diffusion (jitter) including continuous and/or discontinuous shifts have been reported [79, 115–119]. Discrete jumps between two different emission frequencies (also named two-color/bistability) has been observed [120]. Furthermore some systems exhibit on/off behavior (named as blinking, switching, intermittency) [115, 121–123], or switching between three [122] different levels of intensity instead of emission frequency changes. Discrete jumps in the luminescence intensity or frequency are sometimes compared with random telegraph noise (RTN) due to their stochastic properties [124, 125]. The on and off times (or the switch times between the two different emission energies) have independent characteristic timescales and the length of the "on" and "off" intervals shows an exponential distribution. Furthermore, the length of the "on" intervals is strongly excitation power dependent.

Time-integrated continuous-wave PL measurements consist of an average of many recombination events, so that the spectral jitter may lead to a broadening of the peaks in the spectra, when the integration time is not short enough. For natural QDs the measured linewidths depend on the distance of the dot from the sample surface. A narrower linewidth for deeper lying dots was interpreted as a reduced influence on the exciton state of varying surface charges and/or defects [47, 114]. Also, for InP/GaInP SAQDs the unusual temperature dependence of the linewidth, going from several meV broad peaks at low temperatures to narrow peaks at high temperatures was attributed to the fluctuating charge occupation in the dot surrounding [126]. Thus, jitter on a

timescale longer than the radiative lifetime has impact on the measured linewidths and depends on integration time [115, 117]. This has to be considered when discussing the emission linewidth.

Large emission linewidths of several meV were observed by NSOM in InP-stressor-induced GaInAs/GaAs QDs [127] and also attributed to fluctuating surface impurity states. However, since the emission lineshape was Lorentzian it was proposed that charge fluctuations are faster than the intrinsic (radiative) lifetime (and therefore should contribute to pure dephasing Recently, it has been demonstrated [94, 96], that fast environmental fluctuations lead to a Lorentzian emission lineshape (effect of motional narrowing), instead of a Gaussian one, expected for fluctuations slower than the radiative lifetime. The former situation gives rise to pure-dephasing broadening, while the latter to spectral-jitter broadening

Spectral diffusion, including continuous and discontinuous shifts as well blinking, refers to slow (timescale of fluctuation > radiative lifetime) changes, in the emission energy of the emitter. Generally, it is attributed to the quantum-confined Stark effect on the electronic states, similarly to quantum wells when an external electric field is applied. A time-dependent internal electric field is produced by charges in the vicinity of the QD, which are trapped in defects, localized states of the WL or the barrier. For high excitation power excess charge carriers are trapped and released on a large timescale of 0.1 to tens of seconds, creating randomly fluctuating electric fields, which shift the QDs electronic states by the quantum-confined Stark effect. Apart from Stark effect, other mechanisms have been proposed for blinking and switching. A photoionization mechanism based on Auger ionization was proposed for blinking CdSe/ZnS NC [121], whereas switching behavior of InP/GaInP SAQDs was attributed to mobile photocreated non-radiative recombination centers [122].

Spectral jitter and blinking has been observed in a variety 0D dimensional systems: Direct observation of spectral jitter (discrete jumps) was reported for impurity molecules embedded in a crystal using micro PL [124]. In artificially confined systems, the effect was first reported for different types of nanocrystals, namely colloidal CdSe/ZnS and CdSe/ZnSe nanocrystals (NC) (blinking and jitter by imaging and PL) [115, 128] and CdSe/ZnS NC (blinking, PL) [121]. For epitaxially grown dots spectral diffusion or switching behavior was also demonstrated, although it was expected that they should not exhibit such phenomena due to their high

crystal quality. Referring to the II-VI semiconductor materials these effects were observed for MOCVD grown CdSe/ZnSSe QDs (by cathodoluminescence) [79], epitaxially CdSe/ZnSe SAQDs (in 50-nm mesas, micro-PL) [117] and epitaxially grown CdTe/ZnTe QDs (by micro-PL) [118]. Among SAQDs made of III-V compounds the effect was reported for MBE grown InAlAs/AlGaAs SAQDs (by NSOM) [116], MOVPE InP/GaInP SAQDs (RTN, micro-PL and imaging) [122] and MBE GaN/AlN QDs (micro-PL) [119]

Typical shifts are in the range from less than one meV up to several meV for the cited examples. For a jitter amplitude in the order of several meV the involved electric fields are in the range of several 10^5 V/cm. In samples with gates allowing the application of an external electric field, comparable redshifts of the QD emission energy are obtained for similar magnitudes of the field [115, 128]. Internal generation of electric fields of this magnitude imply one or several charge carriers located in the vicinity of the dot at distances from approximately 5 to 10 nm.

The jitter frequency reflects the timescale of these processes. The characteristic timescales range from a fraction of a second to several seconds or even minutes. The involved processes are light-induced, since jitter amplitude and frequency depend on the excitation intensity. For the above cited examples defect states are in general made responsible for charge carrier trapping. More specifically, thickness variations of the wetting layer form large number of shallow potential traps with localized states in which charges can remain very long time [116, 126]. Also stacking faults were proposed, whereas in the same study charges at the etched sidewalls of mesa structures were excluded [117].

Spectral jitter may present an undesired effect as it leads to a broadening of the measured linewidths [115, 117]. It is even worse in quantum information applications, as it introduces further decoherence into the system (pure dephasing for fast/strong interaction) [94, 96]. However, jitter is very useful for identification of QD spectral peaks, because groups of peaks with synchronous shifts or jumps in the emission energy must originate from the *same* single QD [79]. Not always positively correlated jitter is observed, but anti-correlated jumps in energy were observed for the negatively charged trion of epitaxially grown CdTe/ZnTe QDs (by micro-PL) [118].

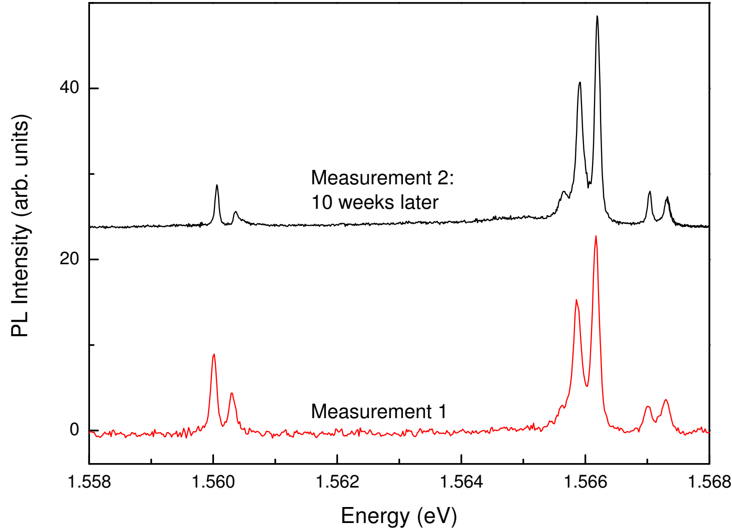

Figure 3.9: Photoluminescence spectra of a single QD for different cool down cycles. Spectra a shifted horizontally since lack of absolute spectrometer calibration.

3.5.1 Results

In Figure 3.9 PL spectra of the same QD taken for different cool down cycles are presented. The top curve was measured 10 weeks after the bottom spectrum. All the spectra are essentially identical, indicating that the near surrounding of the QDs is stable and the charge configuration around the dot does not change dramatically due to different cool-down cycles. However, a small spectral jitter of the QD peaks can be observed on a timescale of seconds to minutes and is attributed to fluctuating local changes in the charge carrier distribution around the dot. An example for such an measurement is shown in Figure 3.10 as an intensity grayscale plot. The time-evolution consists of 30 spectra of one minute integration time each, recorded consecutively. These measurements require high spectral resolution (double spectrometer), and integration time shorter than the jitter fluctuation. Excitation power and energy are $P_{Excit} \approx 1$ mW and $E_{Excit} = 2.41$ eV, respectively. The PL spectrum shown in the bottom panel of Figure 3.10, exhibits several emission peaks. The time-evolution, shown in the top panel of the Figure, reveals that some of the emission peaks (orange colored) exhibit correlated shifts. Another group of peaks (green colored) has its own jitter pattern. Each group of peaks belong to separate individual QDs. Throughout the present thesis, the jitter pattern is used to identify the

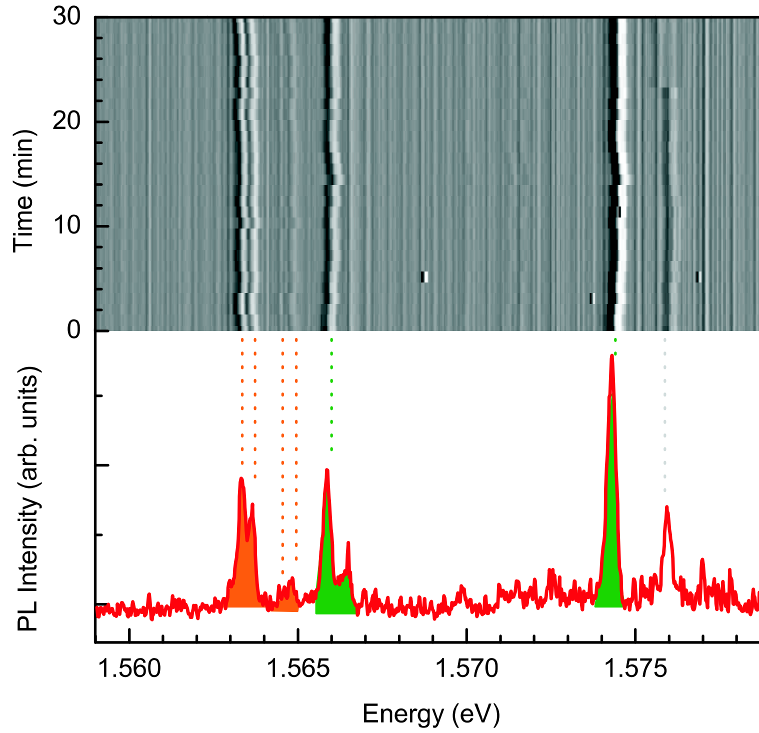

Figure 3.10: The bottom panel shows a photoluminescence spectrum of a 10 μm aperture. The top panel shows the time evolution of the spectrum in a intensity scale plot. It consists of 30 consecutively recorded spectra of one minute integration time each.

peaks belonging to the same QD [79]. Shifts less than one meV, i.e. of the order of magnitude of the linewidth and the fine-structure splitting, are observed on a time scale of seconds to minutes. These results are similar to those obtained on other self-assembled QDs, cited above.

Spectral diffusion energy and time fluctuations depend on the material system. Strong spectral jitter in II-VI structures has been explained by a larger (several orders of magnitude) number of charged defects in II-VI structures than in comparable III-V systems [79]. However, no direct observation of spectral jitter has been reported in micro-PL experiments on the traditional III-V In(Ga)As/GaAs SAQDs. Probably spectral jitter is less pronounced and therefore more difficult to observe, at difference with the presently investigated system. In fact, jitter was reported previously for dots with barriers containing aluminum, namely MBE grown InAlAs/AlGaAs SAQDs (by NSOM) [116]. This indicates that Al(Ga)As barriers favor the observation of spectral

diffusion. Growth studies show that In mobility on AlAs is reduced and leads to a higher density of smaller QDs [24, 29, 129]. Reduced In mobility may also lead to a more corrugated InAs WL in comparison with growth on GaAs barriers. These WL thickness fluctuations probably provide additional trap states near the dot.

In summary, spectral diffusion is a source of peak broadening in time-integrated PL measurements. It provides a way to identify transitions belonging to a single QD. For the presently investigated InAs/AlAs QDs spectral diffusion can be observed in the time-evolution of the micro-PL spectra. A more corrugated wetting layer in comparison with GaAs barriers may provide an increased number of confined states at monolayer fluctuations, which result in a more pronounced jitter pattern.

3.6 Excitation power dependence

In the present section the power dependence of the PL spectra of single InAs/AlAs QDs is investigated. In the low excitation power regime (linear regime) the single exciton peak dominates the PL spectrum. For increasing pumping power more peaks are observed simultaneously in the time-averaged PL spectra, originating from the decay of mutually excluding complexes (charged excitons, biexcitons and probably higher order multi-excitons). The main focus in this section is the intensity dependence of the emission peaks on the excitation power, since it provides a tool to identify the origin of the PL peaks [79, 118, 130], besides the analysis of the jitter pattern (see section 3.5) and the polarization properties (see section 3.7). In particular, power dependent measurements allow the identification of the biexciton transition among the several peaks belonging to the same dot. Further details, in particular the biexciton binding energy and its dependence on the QD size will be discussed in section 4.3.

In QDs one can create and investigate the optical emission of stable biexciton states due to their 3D confining potential [131]. This is in contrast to bulk systems or QWs, where formation and dissociation of exciton-molecules (a bound biexciton state formed from two single uncorrelated excitons) take place. In the latter systems the biexciton binding energies are fairly low (0.2 meV GaAs bulk [132, 133], and about 1 meV GaAs/AlGaAs QW [132]). Biexcitons localized by alloy fluctuations have been observed also for II-VI QWs [134] with binding energies up to 10 meV. Biexcitons can be generated by increasing the excitation intensity and consequently

raising the probability of capture of two excitons by the dot. Biexciton emission peaks appear often red-shifted with respect to the exciton emission energy due to Coulomb interactions. Furthermore, one observes that the exciton intensity increases linearly with the excitation power, while the biexciton intensity increase is super-linear. Both peaks experience a saturation effect, which occurs for the biexciton at higher pump levels and is less pronounced compared to the exciton. However, biexcitons can not only be generated by strong pumping. Another possibility are gated, charge tunable structures with InGaAs/GaAs QDs, allowing the formation of biexcitons and charged exciton complexes [135]. Alternatively, the direct occupation of the biexciton ground state was demonstrated by two-photon resonant absorption in natural GaAs/AlGaAs QDs [46].

For stronger excitation levels the PL spectra exhibit also the emission of higher multi-excitons [136], in addition to the biexciton emission. The biexciton, which consists of two excitons with opposite total angular momentum in the two-fold degenerate single exciton states (s-shell). Due to Pauli-blocking higher excitons fill excited states of the QD, giving rise to groups of emission peaks at higher energies in the PL spectrum (p-d-shells). Such shells have been reported, for example, for InAs/AlGaAs QDs [136] and InAs/GaAs QDs [43] as well InAs/InGaAs [137], with level splittings in the range of several tens of meV.

Several models have been developed in order to understand the power dependence of the exciton and biexciton emission intensities. A rate equation system was proposed [46] based on a four-level model including the empty QD ground state, two degenerate bright exciton states $X_\uparrow$, $X_\downarrow$ and a higher state, which is pumped by the laser. The steady-state population [46] of the two exciton states $X_\uparrow$, $X_\downarrow$ is given by

$$N = N_\uparrow = N_\downarrow = N_{pump}/(N_{pump} + \tau/\tau_r),$$

with the occupation of the pumped state $N_{pump} = bP$. b is the creation efficiency, τ is the relaxation time of the pump state - exciton state transition, P is the pump power and τ_r is the radiative lifetime of the exciton states. The intensities of the exciton and biexciton transitions are then given by

$$I_X = 2cN(1 - N)/\tau_r$$

and

$$I_{XX} = 2cN^2/\tau_r,$$

with the collection efficiency c. For low excitation power P the occupation of the exciton states is approximately $N \propto P$ and the intensities behave nearly as

$$I_X \propto N \propto P$$

and

$$I_{XX} \propto N^2 \propto P^2.$$

This model simulates well the behavior of the investigated natural GaAs/AlGaAs QDs (micro-PL) [46], following the linear and quadratical increase of the emission intensities of the exciton and biexciton peaks, as well the saturation behavior for high excitation levels, which is less pronounced for the biexciton. Another approach is based on the hypothesis that the formation of biexcitons is due to simultaneous random capture of two excitons by the dot [131]. In the high excitation limit of this model, the ratio of the intensities tend to unity $I_{XX}/I_X \rightarrow 1$, due to the inhibition of the capture of an exciton during the sequential decay cascade (biexciton $\rightarrow$ exciton $\rightarrow$ empty QD ground state). This model was applied to the power dependence of the exciton and biexciton emission of CdSe/ZnSe QDs (micro-PL) [131].

The random capture model [131] does not include complexes higher than the biexciton. However, it was extended by including the generation of an electron-hole plasma for high pump intensities [138]. Such an electron-hole plasma, which forms first in the QD, but then becomes increasingly delocalized with increasing excitation power, was made responsible for a broad background emission at higher excitation levels observed in natural GaAs/AlGaAs QDs (SIL-PL) [138]. This model exhibits differences in the exciton and biexciton saturation behavior and it does not predict a constant intensity-ratio at high excitation power, in contrast to the initial random capture model [131].

Besides the above mentioned examples and their interpretations, exciton-biexciton peak pairs with super-linear power dependence for the biexciton and saturation behavior for both at high pump levels have been reported for CdSe/ZnSSe SAQDs (by cathodoluminescence) [79], CdSe/ZnSe QDs (micro-PL) [130, 139], CdTe/ZnTe QDs (micro-PL) [118], InAs/InGaAs DWELL (micro-PL) [137], InAs/GaAs QDs (micro-

PL) [140], InGaAs/GaAs QDs (micro-PL) [141], and large InGaAs/AlGaAs QDs (micro-PL) [142]. Often, the excitation power dependence of the exciton-biexciton peak pair is the only criterion applied to identify the biexciton state [46, 131, 137–140, 142].

Apart from the generation of higher complexes, other effects can occur under strong pumping. The emission peaks usually broaden with increasing pump intensities, what is attributed to exciton-exciton or exciton-carrier scattering [142]. Interestingly, in the presently investigated InAs/AlAs QDs, linewidth narrowing is observed for increasing excitation powers contrary to the above mentioned effect. This is attributed to screening of the exciton-acoustic phonon interaction by free charge carriers. However, in the data presented in this section, this effect is not resolved due to the low spectral resolution of the experiment carried out here. The effect is investigated in detail in section 5.3.

3.6.1 Results

An example of power dependent micro-PL spectra for a typical single InAs/AlAs QD studied in the present thesis are shown in Figure 3.11 for varying laser power ranging from 0.01 to 2 mW. The spectra were recorded in the low density region of the sample using a mask with 10 µm opening, excitation energy of 2.41 eV, at a temperature of around 10 K and integration times from seconds to several minutes depending on excitation power. The PL spectra are normalized by the excitation intensity and vertically displaced for clarity. For the lowest pump levels (around some tens of µW) only a single prominent peak labeled X can be observed at 1.571 eV in the otherwise almost flat PL spectrum. The observation of a single peak in the spectrum at low laser intensity allows its assignment to a neutral exciton. Other small peaks observed at low pumping belong to charged excitons or other QDs.

For laser power exceeding $P = 100$ µW additional emission lines arise. Increasing further the excitation power the peak labeled XX at 1.563 eV grows rapidly and dominates the spectrum for the highest pump level. The broad background emission raising towards lower energies for strong excitation is due to the GaAs bulk exciton recombination. No evidence of a background emission below the group of QD PL peaks is found, as reported for natural GaAs/AlGaAs QDs at high excitation levels, attributed to the formation of an electron-hole plasma [138]. Linewidth broadening

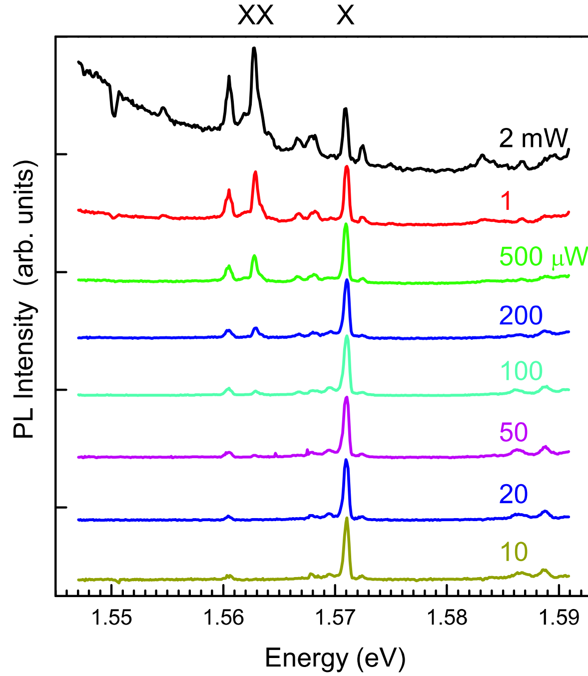

Figure 3.11: PL spectra of a single QD for varying excitation intensity from 0.01 to 2 mW. Spectra are normalized by the excitation power. For low excitation power only a single peak dominates the PL spectra, which is attributed to the exciton emission. With increasing laser power additional peaks appear. The dominating XX peak is attributed to the biexciton. The background emission is due to the GaAs bulk exciton.

due to exciton-exciton or exciton-carrier scattering for high excitation power reported for large InGaAs/AlGaAs QDs [142] is not observed for the spectral resolution of this experiment (0.35 meV, corresponding to a spectrometer's entrance slit of 0.4 mm).[5] The peak at 1.560 eV is probably a charged exciton complex.

The intensity evolution of the peaks labeled X and XX is shown in a double-logarithmic plot (Figure 3.12) as a function of the power of the exciting laser beam. By increasing the excitation power over more than one order of magnitude the intensity of the exciton peak X increases linearly. At intense pump levels above 0.2 mW the exciton transition begins to saturate and for further pumping the exciton peak intensity even starts decreasing. The peak labeled XX can be observed already for low pump intensities well below the onset of saturation of the exciton transition. Its intensity increases quadratically with laser power, and even continues growing further

[5] For the same reason the large fine-structure splitting of this dot cannot be resolved here, too.

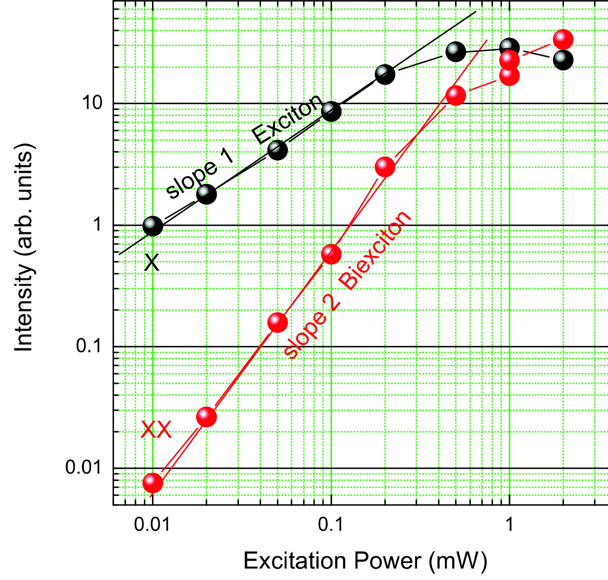

Figure 3.12: The photoluminescence intensities of the exciton X and biexciton XX transitions of Figure 3.11 are shown as a function of the excitation power. Their intensities grow linearly and quadratically with the excitation power, respectively.

while the exciton line decreases in intensity. The XX-intensity evolution exhibits also saturation, which is less pronounced at similar pump intensities in comparison with the exciton transition. The linear and quadratic intensity increases and the saturation behavior are considered as the fingerprint of the exciton and biexciton emission [46], thus confirming the attribution of the X and XX peaks to the exciton and biexciton recombination, respectively. Such power-dependent PL spectra were used throughout the present thesis in order to identify the transitions after assigning peaks to the same single dot by the jitter pattern, see section 3.5. An unambiguous distinction of the biexciton from other super-linear growing peaks is made by polarization dependent spectra, see section 3.7. The theoretically predicted power exponents of one and two have been not always observed. An example is given by the QD investigated in section 5.2, whose power-dependent PL spectra are shown in Figure 5.7. With increasing laser power P the intensities $I_{X,XX} \propto P^n_{X,XX}$ grow with the exponents $n_X = 0.7$ and $n_{XX} = 1.4$ for the exciton and biexciton peaks, respectively. Deviations from the ideal behavior of these kind with $n_{XX}/n_X = 2$ ($I_{XX} \propto I_X^2$) have been reported for MBE grown InAs/InGaAs DWELL structures with exponents $n_X = 0.77$ and $n_{XX} = 1.5$ [137] as well as for MBE grown InAs/GaAs QDs (exponents $n_X = 0.71$

and $n_{XX} = 1.4$) [140]. These deviations are attributed to fast non-radiative scattering processes induced by defects and impurities [143].

Excited states of InAs/AlAs QDs are expected at least 40 meV above the ground state [26, 39], and consequently they are not observed in the small spectral range recorded here.

Figure 3.11 shows that for this particular dot the biexciton emission is 8 meV below the exciton transition energy. The difference is regarded as the biexciton binding energy, that is the energy difference between biexciton complex and two uncorrelated excitons. This value is extremely large compared to binding energies of bulk GaAs (0.2 meV [132, 133]) and QWs (1 meV for GaAs/AlGaAs QW [132]). It also exceeds by far typical values reported for III-V semiconductor QDs (maximum values: natural QDs 4.2 meV [46], 3.3 - 4.8 meV for MBE InAs/InGaAs DWELL [137], up to 5 meV for InGaAs/GaAs QDs [144]). Very large values (around 20 meV) have been found for II-VI QDs [145]. Large values of binding energies are usually attributed to strong confinement in nanostructures. Correlations play also an important role in the biexciton binding energy of our quantum dots, as discussed in more detail in section 4.3.

In summary, the biexciton peak appears under strong pumping in the single dot spectrum several meV below the exciton transition energy. This is a very large value in comparison with the 1-2 meV typically observed for the well studied InAs/GaAs QDs. Details on the biexciton binding energy can be found in section 4.3, where the dependence on the emission energy is studied. The main purpose of the power dependent PL measurements in this work is the distinction of the exciton and biexciton emission by the linear and super-linear intensity increase, respectively. The excitation power dependent screening of the exciton- acoustic phonon interaction is studied in section 5.3.

3.7 Polarization dependence

In general, the exchange interaction lifts the degeneracy between bright and dark excitons (see below) and particularly for low-symmetry dots, the bright exciton state is split, too. The latter is known as "fine structure splitting" (FSS) of the exciton. In view of the creation of polarization-entangled photon pairs for quantum information

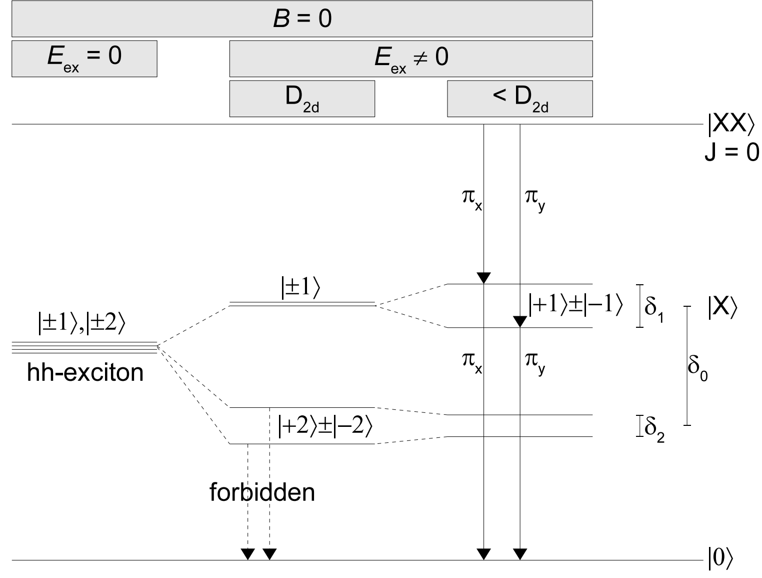

Figure 3.13: Exciton level scheme: For vanishing exchange energy the exciton state is four-fold degenerate. Finite exchange interaction splits these states into dark and bright exciton states. For assymetric confining potentials the bright exciton states are split due to the asymetric exchange interaction. The biexiton state does not split, but the transition exhibits the fine-structure splitting of the exciton state. In this case the optical transitions are linearly polarized along the crystallographic axes [110] and [1$\bar{1}$0].

applications, such splitting is undesired as it provides "which-path" information, preventing a superposition state. [146]. In this section the fine structure splitting of the exciton level is addressed using polarization-resolved PL. The lifting of the degeneracy is reflected by doublets in the exciton and biexciton transitions and their mirror-like polarization properties. These counter-polarized doublets support the identification of the exciton-biexciton pair. The dependence of the bright exciton fine-structure splitting on the QD size and the details of the different contributions to the splitting (structural anisotropy in the lateral plane, atomistic asymmetry of the crystal structure and piezoelectric effects) are discussed in section 4.4.

The optical properties of a direct-band-gap bulk semiconductor are strongly determined by band-to-band transitions at the Γ-point between the CB and the degenerate hh and lh VBs. The optical selection rules of the four optically allowed transitions are governed by the total (spin+orbital) angular momentum of the carriers and its projection J, j_z, which reduce to spin numbers (s, s_z) for electrons: The electron

($s_z = \pm 1/2$) $\rightarrow$heavy-hole ($j_z = \pm 3/2$) optical transitions are $\sigma^{\mp}$ circularly polarized and the electron ($s_z = \pm 1/2$) $\rightarrow$light-hole ($j_z = \mp 1/2$) optical transitions are $\sigma^{\pm}$ polarized. However, in the following discussion of possible QD exciton configurations the light-hole states $|J = 1/2, j_z = \pm 1/2\rangle$ can be neglected, since both strain and quantum confinement split the light-hole (lh) and heavy-hole (hh) bands, which are degenerated at the Brillouin zone center in bulk semiconductors. [6] InAs dots embedded in a GaAs or AlAs matrix are compressively strained. For a quantum well with full biaxial strain, a large lh-hh band splitting of up to 0.5 eV can result. This number can be smaller in QD, as they form by partial strain relaxation of the deposited layer [147]. [7] Additionally, the quantum confinement effect leads to a further splitting of the lh and hh states due to the difference of effective masses, and is estimated for a finite QW to be in the order of 0.020 eV. [8] Thus, the lh-hh splitting is considerably larger than the other relevant energies of the system, as exchange energy, Zeeman energy, (see section 3.8), and thermal energy. Consequently lh states will not be populated by holes at low temperatures.

Figure 3.13 shows an energy level diagram useful in the following discussion. The left level scheme refers to the system without exchange interaction, where the quantum dot exciton state is four-fold degenerate, since four different electron-heavy hole angular momentum configurations are possible by combining the electron with spin $S = 1/2$ and hh with angular momentum $J = 3/2$. The four hh-exciton states are

---

[6] Magnetic fields lift the degeneracy, too.

[7] The hydrostatic strain component only produces a rigid shift of all the hh,lh and so VB bands, and consequently do not split the lh and hh bands. However, in order to perform an estimation of the order of lh-hh band splitting a fully biaxial strained layer is supposed: For biaxial strain generated by a lattice-mismatched layer on a [001] oriented substrate, the strain components become [109, 148] $\epsilon_{xy} = \epsilon_{yz} = \epsilon_{zx} = 0$, $\epsilon_{xx} = \epsilon_{yy} = (a_{subtrate} - a_{QD})/a_{QD}$ and $\epsilon_{zz} = -2C_{12}\epsilon_{xx}/C_{11}$. At the Brillouin zone center the biaxial strain-induced splitting becomes then $E_{hh} - E_{lh} = 2Q\epsilon = -b(\epsilon_{xx} + \epsilon_{yy} - 2\epsilon_{zz}) = -0.493$ eV. The following material parameters are used: the lattice constants $a_{QD} = a_{InAs} = 6.058$ Å, $a_{substrate} = a_{AlAs} = 5.661$ Å. the InAs stiffness constants $C_{11} = 0.833$ Mbar, $C_{12} = 0.453$ Mbar, and the InAs Pikus-Bir (optical) deformation potential constant $b = -1.8$ eV. For biaxially compressive strained layers on [001] substrates the 6x6 matrix representation (basis states: 2 hh, 2 lh, 2 so) of the strain-Hamiltonian, the hh-lh sub-matrix has block-diagonal form, i.e. hh and lh do not mix. lh and so sub-matrix has not block-diagonal form, therefore these bands do mix, but for large so-splitting mixing can be neglected. However, for tensile strain lh and hh bands would mix up strongly.

[8] The estimation is done for a $L = 3$ nm wide and $V_0 = 0.06$ eV deep (InAs/AlAs VB offset) finite QW with the InAs effective masses at the Γ-point in [001] direction $m_{lh} = 0.026m_0$ and $m_{hh} = 0.26m_0$. With $k = \sqrt{2m_{lh,hh}E}/\hbar$, and $\kappa = \sqrt{2m_{lh,hh}(V_0 - E)}/\hbar$, the confinement-induced shift of the lh and hh gound states are the smallest zeros of $f_{lh,hh}(E) = k\tan(kL/2) - \kappa$.

characterized by their total angular momentum components $m = s_z + j_z = \pm 1, \pm 2$, with $s_z = \pm 1/2 = \uparrow, \downarrow$, and $j_z = \pm 3/2 = \Uparrow, \Downarrow$. The $|m = 1\rangle$ ($\downarrow\Uparrow$) and $|m = -1\rangle$ ($\uparrow\Downarrow$) states can couple to the light field and are therefore named bright excitons, in contrast to the states $|m = 2\rangle$ ($\uparrow\Uparrow$) and $|m = -2\rangle$ ($\downarrow\Downarrow$), which are dipole-forbidden and named dark exciton states.

The spin-spin interaction Hamiltonian, also named exchange interaction Hamiltonian, is given by [17, 145, 149] $H_{spin} = a_z j_z s_z + \Sigma_{i=x,y,z} b_i j_i^3 s_i$ with the electron, and hh angular momentum components s_i , j_i and the spin-spin coupling factors a_z and b_i. The exchange interaction has several consequences on the exciton states, that can be understood by examining the structure of the matrix representation of the spin Hamiltonian on the $|\pm 1\rangle, |\pm 2\rangle$ basis:

$$H_{spin} = \begin{pmatrix} \delta_0 & \delta_1 & & \\ \delta_1 & \delta_0 & & \\ & & -\delta_0 & \delta_2 \\ & & \delta_2 & -\delta_0 \end{pmatrix}$$

(i) For a QD with D_{2d} symmetry the exchange interaction splits (see center level scheme of Figure 3.13) the fourfold exciton state into two doublets (named also exchange interaction splitting, singlet-triplet splitting and dark-bright splitting), namely the $m = \pm 1$ radiative (bright) and the $m = \pm 2$ non-radiative (dark) exciton states: Both doublets are separated by $E_{ex} = \delta_0 = 3/2(a_z + 9/2b_z)$. The spin Hamiltonian exhibits a block form for the bright $|m = \pm 1\rangle$ and dark exciton states $|m = \pm 2\rangle$. Therefore bright and dark exciton states are not mixed. A further discussion of the dark-bright exciton splitting and examples are given in the section 3.8 in the context of magnetic fields.

(ii) Inside each block the states are mixed up when the off-diagonal elements are non-zero. This is always the case for the dark exciton state, even for a dot with D_{2d} symmetry. The cubic term in the Spin-Hamiltonian splits the triplet $|\pm 2\rangle$ states by $E_{as,\pm 2} = \delta_2 = 3/4|b_x + b_y|$ and also mixes them ($|+2\rangle \pm |-2\rangle$).

-(iii) In contrast to the dark exciton states, the bright states $|\pm 1\rangle$ are degenerated for D_{2d} symmetry (symmetric confining potential, $b_x = b_y$). By lowering the symmetry of the QD below D_{2d} ($b_x \neq b_y$, see right level scheme in Figure 3.13), the bright states are split by $E_{as,\pm 1} = \delta_1 = 3/4|b_x - b_y|$ and become mixed, too. The anisotropy mixed states $|+1\rangle \pm |-1\rangle$ are dipole active along two orthogonal principal axes of

the nanostructure and give rise to linearly cross-polarized transitions along the [110] and [$1\bar{1}0$] crystallographic directions (polarization anisotropy). In the following of the present thesis the term fine-structure splitting refers in general to the splitting of the bright exciton states (anisotropic exchange splitting).

The biexciton state is a singlet state with total angular momentum $J = 0$, since it is formed by pairs of electrons and holes with opposite angular momentum projection, respectively, and therefore they are not affected by the exchange interaction. Nevertheless, the biexciton emission experiences also the lifting of the degeneracy of the exciton state with the same amount of fine-structure splitting. Consequently, similarly to the exciton emission, the biexciton emission is also a doublet consisting of two orthogonally linear polarized peaks along the [110] and [$1\bar{1}0$] crystallographic directions. The spectral order of the polarized peaks of the biexciton emission doublet is reversed with respect to the sequence of the exciton transitions.

Exchange interaction effects were observed also in QW with symmetry lower than D_{2d} and. Optically detected magnetic resonance measurements on type-II GaAs/AlAs QWs revealed a zero-field splitting (0.35 - 1.5 µeV) of the bright exciton state with linear polarization along the [110] and [$1\bar{1}0$] crystallographic directions, interpreted as symmetry lowering from the D_{2d} symmetry of QWs [150]. Further, it was found, that for a fraction of excitons in type-I GaAs/AlGaAs QWs (measurement of the circular polarization degree of magneto-PL) [151] the optically allowed states are non-degenerate at zero field and have [110] and [1-10] symmetry. Growth steps in the interfaces were proposed as the anisotropy source along the [110] and [1-10] directions [151]. Fine-structure splitting values of 20-60 µeV and linear polarization was observed in natural QDs in GaAs/AlGaAs QWs (PL) [59, 152], for the ground and excited states. [9] Other values measured for the bright exciton splitting include: 0.15 meV for InGaAs/GaAs SAQDs [149], 0.15-0.35 meV for MOCVD InAs/InGaAs/GaAs DWELL [154], and extreme large splittings of 0.5-1 meV for InAs/$Al_{0.6}Ga_{0.4}As$ SAQDs [17]. This large FSS is tentatively attributed to shape anisotropy and enhanced confinement due to the Al containing barriers but the precise origin is left open. A large range of splittings is observed for II-VI semiconductor QDs: 13 μeV [155], 0.2 meV [156], 0.04-0.45 meV [155], 0.3-0.8 meV [145] for CdSe/ZnSe QDs, and 0.17 meV for natural QDs in CdTe/CdMgTe QW [157]. Several

[9] Similar values were calculated [153] for 42-48 nm large asymmetric islands.

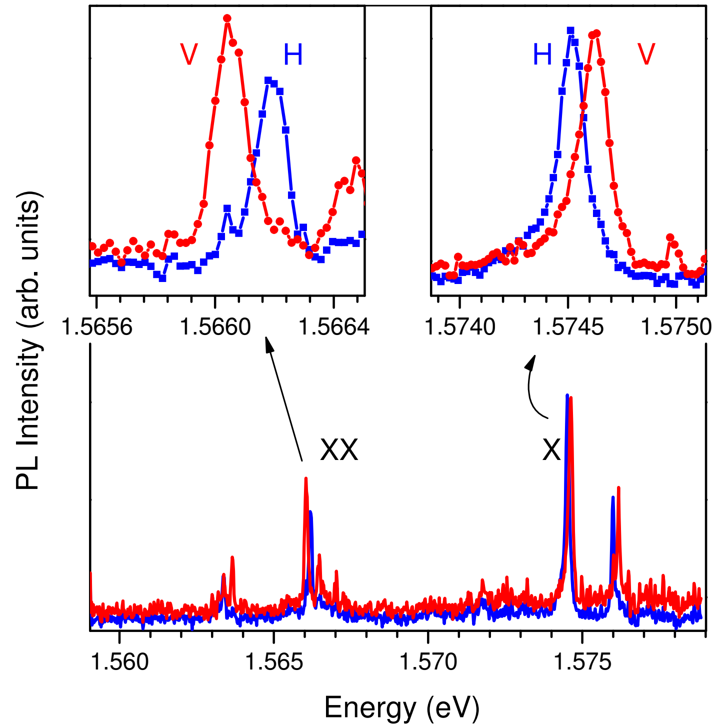

Figure 3.14: Photoluminescence spectra of a single QD: The exciton (X) and biexciton (XX) emission lines consist of fine-structure split doublets with linear cross polarization along the crystallographic axes [110] and [1$\bar{1}$0]. The insets show details of the X and XX peaks.

authors also report the biexciton fine structure and its mirror symmetric polarization to the exciton doublet [130, 145, 154, 157].

3.7.1 Results

Figure 3.14 shows polarization resolved spectra of a single QD. The spectra were taken at a temperature of 10 K and excited with an energy and intensity of 2.54 eV and 1 mW, respectively. The entrance slits of the spectrometer were set to 50 µm and short integration times were used in order to reduce jitter-induced broadening. In the bottom panel of the Figure mutually orthogonal linear polarized PL emission along the laboratory axes H (horizontal) and V (vertical) are shown as blue and red curves, respectively. H and V correspond to the [110] and [1-10] crystallographic directions. The PL spectra exhibit two doublets X and XX, which are shown in the

upper enlarged left and right insets, respectively. The exciton peak X at 1.5745 eV consists of two orthogonally polarized components with the H-polarized emission about 0.3 meV below the V-polarized emission line. A more detailed discussion and a systematic study of the bright exciton fine-structure splitting in function of the exciton emission energy follows in section 4.4. The biexciton emission XX at 1.566 eV (about 8.5 meV below the exciton peak) exhibits a similar large splitting, but the sequence of the linearly polarized peaks is reversed compared to the exciton doublet. The polarization properties therefore confirm the assignment of the PL peaks to the exciton and biexciton emission, which can be distinguished by their excitation power dependence, see section 3.6.In this measurement the splittings of the exciton and biexciton are slightly different, due to spectral wandering between consecutive measurements of the two orthogonally polarized spectra.: If the second recorded PL spectra, say the H-polarized one, is shifted to higher energies by the jitter amount, the splitting of the biexciton peak increases and simultaneously the splitting of the exciton doublet decreases. The effect of jitter can be eliminated by time-averaging both splittings, at the price of a higher linewidth.

In summary, lowering of the QD symmetry lifts the angular momentum degeneracy of the bright exciton state due to the asymmetry of the electron-hole exchange interaction. The exciton states become mixed with the consequence that both the biexciton and exciton emission split and their emission polarization becomes linear. The observation of such orthogonally polarized doublets with opposite order for the biexciton and exciton, along with the power dependence and jitter pattern allows their assignment. A large fine structure splitting is observed compared to the widely studied InAs/GaAs QDs, and attributed to piezoelectric fields. The size dependence of the splitting is further discussed in section 4.4.

3.8 Magnetic field dependence

Magneto-PL spectroscopy is a very powerful tool for the investigation of the fine-structure of electronic states since the magnetic field couples to the electron and hole spins and lifts existing spin-degeneracies. The following discussion complements the one in section 3.7 on the exciton levels splitting by exchange interaction. For the investigated InAs/AlAs dot the Zeeman splitting of the bright exciton state gives

a g-factor of 1.7. The observed diamagnetic shift of 1.4 µeV/T^2 is extremely small indicating strong localization of the exciton wavefunction by the high AlAs barriers. Furthermore, the magneto-PL measurements reveal narrow sidebands observed below the bright exciton doublets. As shown later on, they are unlikely to be due to dark exciton states becoming "bright" by the field. The physical origin of this low-energy sidebands is investigated in section 5.3.

The coupling of the electron and hole spins via the electron-hole exchange interaction for zero magnetic field has been discussed in section 3.7. It gives rise to splitting of the four-fold degenerated exciton level into two bright and two dark exciton states. Here, the inclusion of an external magnetic field, which couples to the electron and hole spins, is studied. As discussed in 3.7 confinement and strain split the heavy and light hole states by a large amount. This strongly reduces mixing of these states, allowing to neglect the light hole states. Recalling the notation from section 3.7, the four exciton states are described by the sum of the angular momenta projections of the electron and hole that form the exciton $M = S_z + J_z$. This result in heavy hole excitons with total angular momenta $M = \pm 1$ and $M = \pm 2$, being $S_z = \pm 1/2$ and $J_z = \pm 3/2$ the electron and hole angular momenta projections, respectively.

Zeeman splitting

Figure 3.15 shows the evolution of the exciton states energies in a magnetic field and helps in the following discussion. The Hamiltonian, which couples the magnetic field B with the electron $S = 1/2$ and hole $= 3/2$ angular momenta (also named Zeeman interaction) is given by [150, 151, 158] $H_{Zeeman} = \mu_B \Sigma_{i=x,y,z}(g_{e,i}S_i - g_{h,i}J_i/3)B_i$ with the Bohr magneton $\mu_B = e\hbar/2m_e$ and the anisotropic electron and hole g-factors $g_{e,i}$ and $g_{h,i}$. The matrix representation in the basis of the exciton states (m=$|\pm 1\rangle$, $|\pm 2\rangle$) is given in Ref. [102, 158] for an arbitrary oriented magnetic field. For a field applied parallel to the growth axis z (Faraday configuration) the matrix is diagonal, so that states are shifted but not mixed. For electron g_e and hole g_h g-factors in the z-direction the bright- and dark- exciton g-factors are: $g_B = g_e + g_h$, $g_D = g_e - g_h$, respectively, and the Hamiltonian matrix takes the form [102]:

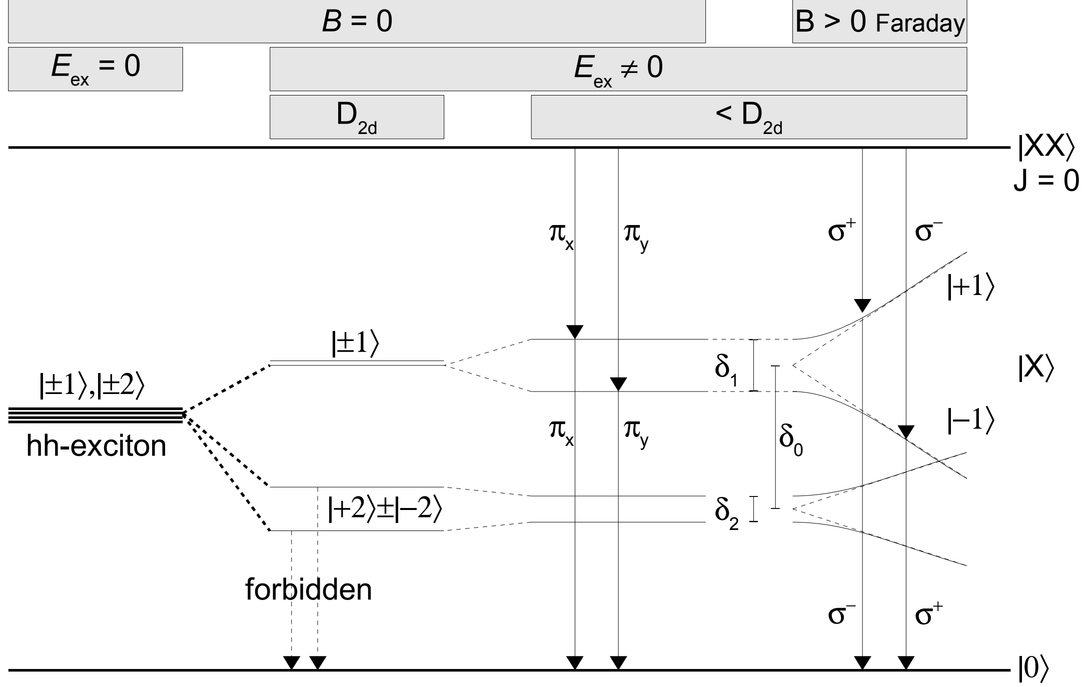

Figure 3.15: Exciton level scheme: The exciton state splits by applying a magnetic field (Faraday configuration) due to the Zeeman interaction. For high magnetic fields the Zeeman interaction dominates over the exchange interaction, i.e. mixing of the states is negligible and the transitions become circularly polarized.

$$H_{Zeeman,B||z} = \mu_B B_z/2 \begin{pmatrix} +g_B & & & \\ & -g_B & & \\ & & +g_D & \\ & & & -g_D \end{pmatrix}.$$

This matrix is similar to the exchange interaction Hamiltonian. Consequently, the in-plane symmetry (if present) of the QD is preserved, bright and dark states are not mixed and angular momentum remains a good quantum number. For magnetic fields applied perpendicular to the growth axis (Voigt configuration) the matrix has not a block-diagonal form anymore and bright and dark states get mixed. In Voigt configuration the matrix is [102]

$$H_{Zeeman,B||x} = \mu_B B_z/2 \begin{pmatrix} & & g_{e,x} & g_{h,x} \\ & & g_{h,x} & g_{e,x} \\ g_{e,x} & g_{h,x} & & \\ g_{h,x} & g_{e,x} & & \end{pmatrix}.$$

Thus, in Voigt configuration, the dark states become optically active allowing their study by PL spectroscopy. In Faraday configuration dark excitons have been observed, too, what has been attributed to a slightly tilted magnetic field that mixes dark and bright [102]. Due to the mixing, magneto-PL measurements are often employed for studies involving the dark exciton: Bright-dark exciton splittings δ_0 of one and two orders of magnitude larger than the bulk values were reported (20 µeV for bulk GaAs [151] and 4.3 µeV for bulk $In_{0.6}Ga_{0.4}As$ [102]). Measured values for QDs include 100 - 250 µeV [102, 149, 158] for InGaAs/GaAs QDs (systematically increasing for decreasing QD size [102]), 4 meV [159] and 0.4 - 0.45 meV [102] for InAs/GaAs QDs, 1.5 - 5 meV for InP/GaInP QDs [160], 0.13 meV for CdSe NC [161] and 1.7 - 1.9 meV [156] and 3.2 meV for CdSe/ZnSe QDs [145].

The energy of the two bright and two dark eigenstates is given as a function of the magnetic field B oriented in Faraday configuration by [102]

$$E_{\pm 1} = 1/2(\delta_0/2 \pm \sqrt{(g_e + g_h)^2 \mu_B^2 B^2 + \delta_1^2})$$

and

$$E_{\pm 2} = 1/2(\delta_0/2 \pm \sqrt{(g_e - g_h)^2 \mu_B^2 B^2 + \delta_2^2}),$$

respectively. For low magnetic fields the states shift quadratically with the magnetic field. For high magnetic field one can neglect the asymmetry splittings δ_1 and δ_2 of the bright and dark exciton doublets and the states shift linearly with the magnetic field according to

$$E_{\pm 1} \approx 1/2(\delta_0/2 \pm |g_e + g_h| \mu_B B)$$

and

$$E_{\pm 2} \approx 1/2(\delta_0/2 \pm |g_e - g_h| \mu_B B).$$

The Zeeman splittings of the bright and dark states are then given by

$$\Delta E_{\pm 1} = |g_e + g_h| \mu_B B \texttt{ and } \Delta E_{\pm 2} = |g_e - g_h| \mu_B B. \tag{3.3}$$

These splittings add to the exchange one, which usually can be neglected at high magnetic fields. Absolute bright exciton g-factors $|g_e + g_h|$ around 2 are usually reported: For example, 2.4 [162], 3 [141, 149, 158], and 2 - 3 [163] for InGaAs/GaAs QDs, 1 - 2 [163], 0.6 (tall) - 2.8 (flat) [164] and 3.23 [165] for InAs/GaAs QDs, 0.5

- 1.5 for InAs/InGaAs/GaAs DWELL [154] as well 1.56 for CdSe/ZnSe QD [145]. Some authors report a tendency [164, 166] of decreasing g values for decreasing dot size.

Diamagnetic Shift

Apart from the Zeeman splitting, which reflects the breaking of the spin degeneracy, there is an overall shift to higher energies of the electronic levels. In contrast to free carriers, whose levels shift linearly in a magnetic field (named Landau-levels), in structures restricting the cyclotron motion, the effect is reduced to a quadratic shift for low magnetic fields (named diamagnetic shift). Thus, the recombination energy exhibits a quadratic shift for small magnetic fields, which becomes linear for high magnetic fields, as the electronic system approaches the Landau-level behavior. The diamagnetic shift can be approximated for strong geometric confinement by [141]

$$\Delta E_{diamag} = e^2/8(< r_e^2 > /m_e + < r_h^2 > /m_h)B^2,$$

where m_e, m_h are the electron and hole effective masses, and $< r_e^2 >$, $< r_h^2 >$ the mean square lateral extensions of electron and hole wavefunctions. Assuming similar wavefunction extensions for the electron and hole $< r_e^2 > \approx < r_h^2 > \approx < r_X^2 >$, the diamagnetic shift becomes

$$\Delta E_{diamag} = e^2 < r_X^2 > B^2/(4\mu) = \gamma_2 B^2,$$

with the in-plane reduced mass $\mu = m_e m_h/(m_e + m_h)$ and the diamagnetic coefficient $\gamma_2 = e^2 < r_X^2 > /4\mu$. Thus, the diamagnetic coefficient γ_2 is a measure of the exciton wavefunction extension. The stronger is the localization, the weaker is the shift. A systematic study on InGaAs/GaAs QDs [167] shows decreasing diamagnetic coefficients for decreasing structure sizes down to $\gamma_2 = 10$ μeV/T^2 for 20 nm wide deep etched QDs and $\gamma_2 = 20$ μeV/T^2 for 30 nm wide modulated barrier QDs. For self-assembled QDs the diamagnetic coefficient γ_2 has typically values near 10 μeV/T^2. For example, the following values were reported for In(Ga)As/GaAs QDs: 7.8 [141] [10] 6.3 [162], 9.22 [163], 10.7 [165], 6.4-16 [164], 6.5-8.5 [154] and 25-12 μeV/T^2

[10] Not all cited authors give the number. Then is extracted from the Figures, see for example Figure 3 of [141]: The diamagnetic coefficient is $\gamma_2 = 0.5$ meV $/8^2$T$^2 = 7.8\mu$eV/T^2.

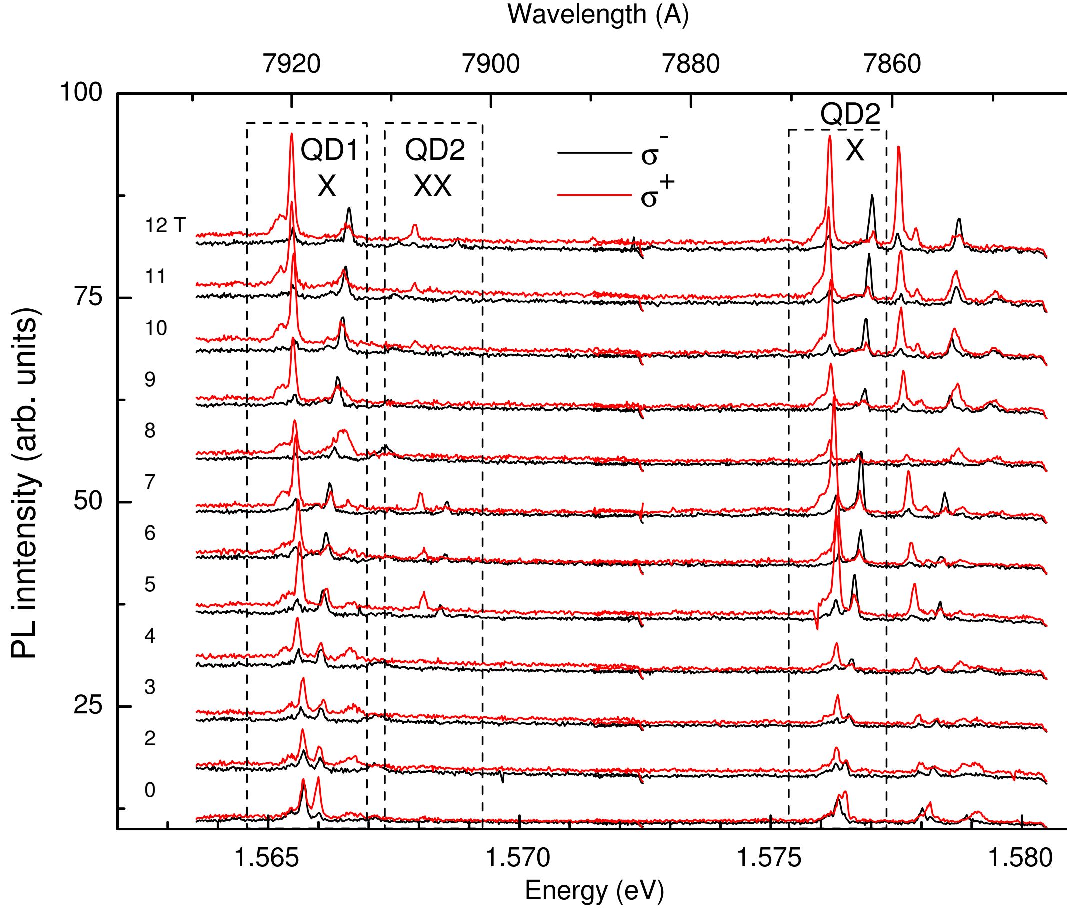

Figure 3.16: Polarized PL spectra of the exciton doublet for a series of magnetic fields up to 12 T. Red and black curves show right and left circularly polarized emission, respectively. The emission of two individual excitons QD1 and QD2 is observed. Low-energy sidebands accompany the ZPL doublets up to 12 T. Already for low magnetic fields (> 4 T), the magnetic field restores D_{2D} symmetry and emission transforms from linear to almost fully circularly polarized. Spectra are taken at 10 K.

(systematically decreasing with exciton emission energy from 1.34-1.41 eV) [168].

3.8.1 Results

The magneto-PL setup described in section 2.1 was used. It is necessary to make a dot re-alignment for each magnetic field because of the high sensibility of the setup to magnetostriction. The polarization of the luminescence was analyzed by a quarter-

wave retarder and a linear polarizer. A scrambler was placed in front of the spectrometer's entrance slit, in order to get rid of the polarization sensibility of the gratings. The dots are excited non-resonantly above the wetting layer with the 514 nm line of an Ar+ ion laser at a temperature of about 2 K. Figure 3.16 shows circularly polarized micro-PL spectra for varying magnetic field up to 12 T of two individual QD excitons emitting near 1.566 eV (QD1) and 1.576 eV (QD2) at zero-field, respectively. Spectra are vertically shifted for clarity. Red and black curves show σ^+ and σ^- polarized spectra, respectively. For increasing magnetic fields the energy separation of zero-field split exciton doublets increases due to the Zeeman interaction. For both excitons the σ^+ polarized low-energy component first shifts slightly to lower energies and is nearly constant for higher magnetic field, since the diamagnetic shift to higher energies compensates the Zeeman shift to lower energies. In contrast, the σ^- polarized high-energy emission peaks experience a strong shift to higher energies, as both contributions have the same sign. Furthermore, both exciton doublets exhibit narrow sidebands, which remain close to the Zeeman-split exciton peaks for all magnetic fields.

For low magnetic fields both components of the exciton doublets are observed in both circular polarizations, since both are linearly cross-polarized. For increasing fields the emission turns gradually circularly polarized. In-plane isotropy can be restored by comparatively small magnetic fields of $B > 4$ T, indicating a only a small geometric in-plane anisotropy. Interestingly, a very large zero-field fine-structure splitting of about 0.28 meV is observed, while our magneto-PL results indicate only a small lateral asymmetry. This suggests that the large fine-structure splitting is not originated by geometrical asymmetry. In section 4.4 the origins of the large fine structure splittings are discussed.

The doublets around 1.568 eV in the spectra taken at 5 - 7 T correspond to the biexciton emission of QD2. The magnetic field does not split the $J = 0$ spin-singlet biexciton state, but the biexciton transition inherits the splitting from the final exciton state. Both the biexciton and exciton doublets have the same circular polarization sequence, in contrast to the mirror-like linear counter-polarized doublet at zero-field (see Figure 3.16).

Figure 3.17 (a) shows the energy positions of the main exciton transitions, (which will be called zero-phonon-lines (ZPLs) for reasons given below) and the sidebands of

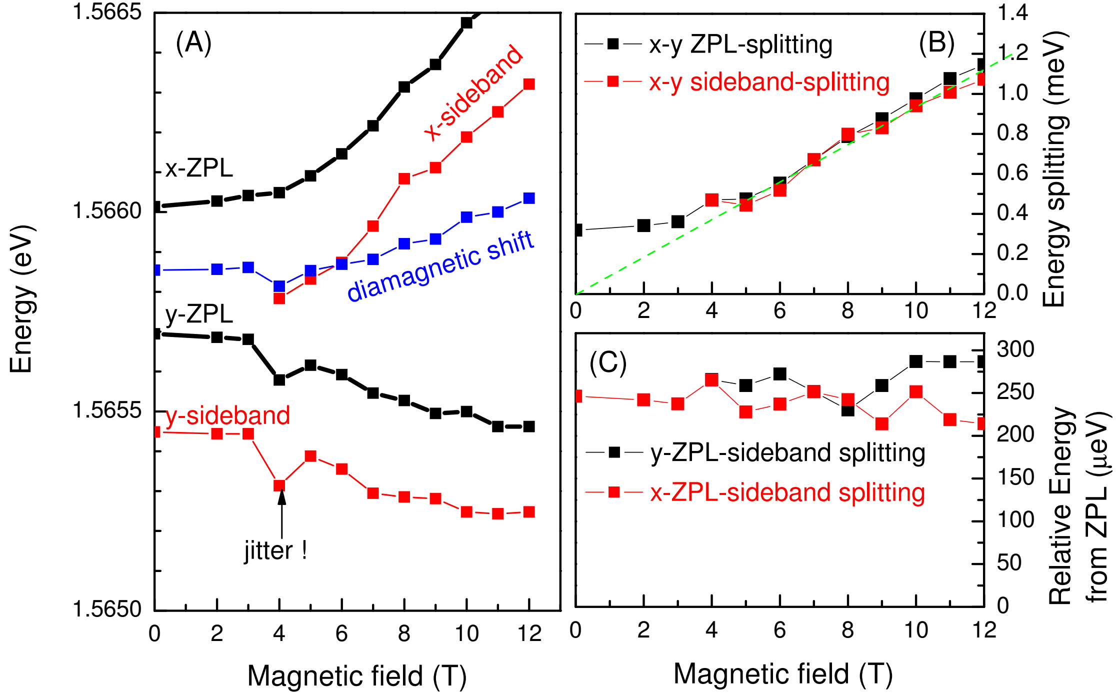

Figure 3.17: Magnetic field dependence of peak positions and splittings: (a) The energy position of the (zero-phonon lines) ZPLs and the narrow sidebands are shown in black and red curves, respectively. The blue curve is the center of the ZPL doublet, i.e. it shows the diamagnetic shift. (b) The black and red curves show the splittings between the ZPLs and sidebands, respectively. (c) The red (black) curve show the energy separations between the x (y)-sideband and the x (y)-ZPL.

QD1 as a function of the magnetic field. The energy difference of the bright exciton doublet (black curve) is shown in Figure 3.17 (b). For fields up to 5 T the splitting deviates significantly from the linear Zeeman splitting due to the large fine-structure splitting. For fields above 5 T the splitting increases linearly with increasing magnetic field. At 12 T the Zeeman splitting amounts to 1.2 meV corresponding to an exciton g-factor of 1.7, what is in the range of the values cited above. A study on dots with AlGaAs barriers [17] gives a g-factor of 2.25. Since the dark exciton is not observed in the spectra (see discussion below), the electron and hole g-factors cannot be determined separately.

The narrow sidebands are 0.25 meV below the exciton ZPLs. Since similar splittings were reported for the bright-dark exciton splitting in self-assembled QDs, one

might tentatively attribute the sidebands to the emission of the dark exciton states. Several arguments contradict this hypothesis: (i) Dark exciton states observed at zero-magnetic field due to a strongly broken symmetry of the dot are not described in the framework of the exchange interaction Hamiltonian introduced in section 3.7. (ii) Furthermore, a large range of values up to several meV were observed, see the values cited above. For InAs dots embedded in AlAs barriers an one order of magnitude larger bright-dark exciton splitting in the meV-range was estimated [33, 77]. (iii) The magneto-PL measurements contradict the dark-exciton hypothesis. The red curve in Figure 3.17 (b) shows that the splitting between the two narrow sidebands is essentially the same as the bright exciton Zeeman splitting. Figure 3.17 (c) demonstrates that the separation between the ZPLs and its sidebands is approximately constant for magnetic fields up to 12 T. From the equations 3.3 follows that only in the unlikely case that either the electron or the hole g-factor is zero, both bright and dark exciton Zeeman splittings are the same, what would lead to the behavior observed in panels (b) and (c). This excludes that the sidebands are due to dark exciton states, but rather seem to be a feature of the ZPLs itself. In section 5.3 it is demonstrated, that the narrow sidebands are due to the interaction of the QD exciton with acoustic phonons.

The blue curve of Figure 3.17 (a) is the center of the Zeeman split doublet, and it therefore shows the diamagnetic shift of the exciton level. The diamagnetic coefficient of the quadratic shift to higher energies is extremely small with $\gamma_2 = 1.38\ \mu\text{eV/T}^2$ and fairly below the typically reported values cited above for the commonly studied In(Ga)As/GaAs QDs. This indicates the extremely strong localization due to the high AlAs barriers. In agreement with that, a likewise small value of 3.5 μeV/T^2 [17] was reported for InAs QDs in InAs/$Al_{0.6}Ga_{0.4}As$ barriers. The shift is quadratic with the field up to 12 T. This shows that, due to the strong confinement, the system does not approach the linear Landau-level behavior in the available magnetic field range.

In summary, at high magnetic fields the Zeeman splitting corresponds to a bright exciton g-factor of 1.7, which is close to the widely reported value around 2. An extremely small diamagnetic shift of 1.4 μeV/T^2 points to strong localization due to the high AlAs barriers. Circular polarization is restored for small fields, indicating only small structural dot asymmetry. The magneto-PL measurements reveal that the narrow sidebands below the ZPLs are likely not due to dark excitons emission.

The origin of these sidebands is discussed in section 5.3 in terms of exciton-acoustic phonon coupling.

Chapter 4

Electronic properties

In this chapter the exciton and biexciton emissions of a series of single quantum dots of InAs in an AlAs matrix are studied. As discussed in chapter 3, these emissions consist of linear cross-polarized doublets showing large values of both the biexciton binding energy and the fine-structure splitting. At increasing exciton emission energy, corresponding to decreasing dot size, the biexciton binding energy decreases from 9 meV down to zero, reflecting a possible crossover to an antibinding regime. Simultaneously the fine-structure splitting diminishes from a value of 0.3 meV down to zero, at the same energy, suggesting a common origin for the two effects. [1]

4.1 Introduction

Semiconductor quantum dots are important for production of single photons [169] and entangled photon pairs [7, 170] for quantum information processing, due to the discrete and tunable electronic structure of zero-dimensional systems. Confinement of carriers in QDs at distances smaller than the Bohr radius increases electron interactions, which are crucial to determine the electronic structure and the optical properties of the QD. Electron interactions determine the relative alignment and the eventual coherent coupling of excitons and biexcitons [171], which has been proposed as a suitable system for quantum gate operations [172]. Both the biexciton binding energy (BBE) and the fine-structure splitting (FSS) are basic features of QDs

[1]Part of these results were published in J. Appl. Phys. 100, 023109 (2006) and Physica E 32, 111 (2006)

caused by Coulomb interactions, which depend on the QD shape, size, composition and strain.

The biexciton binding energy ΔE_{XX} is the difference in energy needed to create a second electron-hole pair in a QD with already one pair present, and corresponds therefore to the energy difference between two separated excitons $2E_X$ and the biexciton complex E_{XX}: $\Delta E_{XX} = E_{X-emission} - E_{XX-emission} = 2E_X - E_{XX}$. The biexciton binding energy depends on the details of the Coulomb interaction and it can become negative (antibinding) when confinement is reduced in small dots [144, 173, 174], in contrast to the always positive exciton binding energy. [2] An anti-binding biexciton is a stable configuration in spite of the repulsive Coulomb interactions, since the 0D confinement potential prevents the separation of the charges. In principle one would expect the interaction between two neutral excitons to be weak, but localization of the electron and hole wavefunctions leads to a complicated interplay of the various Coulomb interactions, including direct repulsive Coulomb contributions between the two electrons and two holes, respectively. This interplay depends sensitively on the details of the QD size, shape and composition and results in scatter of the observed BBE values [146, 173, 175].

The BBE was studied as a function of the exciton emission energy. An enhancement of the BBE for decreasing QD size was predicted theoretically [176] and observed in CuCl QDs [177] as well as in etched QDs [167].

In very small QDs an antibinding biexcitons have been predicted as the repulsive Coulomb interactions overcome other contributions [178]. In a series of annealed InGaAs/GaAs QDs [175] an increment of the BBE was initially observed, followed by a BBE decrease, for increasing exciton emission energy (i.e. for decreasing dot size). The increment was attributed to the reduction of the asymmetry of the In distribution upon annealing of the samples. Annealing converts the initial asymmetric indium distribution into a Gaussian-like distribution. The asymmetric distribution favors electron-hole charge separation [179] and therefore increases repulsive contributions [180]. The BBE decrease observed for smaller dots [181]is attributed to the decreasing confinement energy, due to finite barriers. In a PL study on InAs/GaAs QDs [146] no correlation between the BBE and the exciton emission energy was found. In contrast, a cathodoluminescence study likewise on InAs/GaAs QDs [173] reports

[2] The exciton binding energy is given by attractive direct Coulomb interaction between charge carriers of opposite sign, exchange interaction and correlation.

a decreasing BBE for increasing exciton recombination energy, which is explained by a dominant contribution of correlation terms in the electron-hole interaction. Correlation is reduced in smaller QD due to their smaller number of confined states.

The origin of the fine-structure splitting (FSS) is the asymmetry of the electron-hole exchange interaction along the (110) and (1-10) crystallographic directions, which leads to the splitting of the degenerate bright exciton states (see also section 3.7). This asymmetry has been initially attributed to a QD lateral elongation along these directions [17, 59, 145, 157]. In addition to that, the asymmetric piezoelectric potential associated to shear strain [182–184] and the intrinsic atomistic asymmetry of the zinc-blende lattice [174, 185] can also produce a splitting even in a cylindrical QDs. The control of the FSS is important because the possibility to make it smaller than the homogeneous emission linewidth of the QD is a crucial step to obtain entangled pairs of photons.

Several studies have been performed in order to correlate the FSS with the exciton emission energy. For InGaAs/GaAs QDs [102] no correlation was found between the bright exciton fine-structure splitting (0-0.15 meV) and the dot emission energy in the range of 1.30-1.33 eV. The same holds for InAs/GaAs QDs [102] for the emission energy range of 1.295-1.315 eV (FSS = 0.1-0.18 meV). Also for InAs/InGaAs/GaAs DWELL [154] the magnitude of the FSS of 0.15-0.35 meV is independent of the exciton emission in the energy range of 0.94-0.975 eV. These studies cover only a small emission energy range of 20-35 meV and scatter of the data might obscure any existing trend. However, studies extended over a larger emission energy range in series of annealed InGaAs/GaAs QDs [175], uncovered a systematic trend of the FSS, namely, a decrease of the FSS from 96 to 6 μeV with increasing emission energy. The effect is interpreted in terms of a symmetrization of the in-plane exciton confinement due to indium diffusion. A similar study was performed on InGaAs QDs [186] and InAs/InGaAs/GaAs DWELL [187] revealing the same trend. In this case the FSS reduction is attributed to a reduction of strain due to In/Ga intermixing, what results in a more s-like exciton wavefunction and hence weaker electron-hole exchange interaction. Decreasing FSS by repeated annealing steps of the same individual InAs/GaAs QD is also attributed to a symmetrization of the wavefunctions [188]. Recent results reveal a sign reversal of the fine-structure splitting for increasing photoluminescence (PL) emission energy in InAs/GaAs dots [146, 184].

While the vast majority of systems studied so far are InAs QDs with GaAs or AlGaAs [17] barriers, the use of AlAs barriers has some advantages: (i) stronger carrier confinement leading to visible emission and enhanced electron interactions, (ii) longer lifetimes [34] due to the poorer phonon coupling to the barriers, and (iii) strong reduction of intermixing between the QD and the barriers [33, 129]. In addition, the higher confinement leads to a different mixing of heavy and light holes, which in turn affects the electronic and optical properties of the QD. In the following the results of a PL study of the biexciton binding energy and the fine-structure splitting in single InAs/AlAs QDs is presented. Both quantities have larger values than in InAs/GaAs dots and decrease monotonously with increasing QD emission energy, i.e., with decreasing QD size. Both BEE and FSS vanish for emission energy around 1.63 eV, suggesting a possible sign reversal in both magnitudes. These results suggest a common origin for the size dependent reduction and vanishing of both the biexciton binding energy and fine-structure splitting. They are tentatively interpreted in terms of the changes in the exciton extension and shape as the confinement is reduced when the dot size is decreased. The results give support to the possibility to create entangled photon pairs in the visible region using InAs/AlAs QDs.

4.2 Experiment

Details of the investigated InAs/AlAs QD sample [67] can be found section 2.2.2. The PL emission was excited with an argon-ion laser with a typical power on the sample of 1 mW. All the measurements were taken at about 9 K. Further details on the experiment are described in section 2.1. Selected openings of the sample metal mask, as well as larger areas ($10 \times 10 \mu m^2$) outside the mask, were initially mapped by PL. Exciton and biexciton peaks belonging to the same QD were identified by three required conditions as discussed in chapter 3: (i) parallel random time evolution of the PL energies (jitter), (ii) linear and quadratic PL intensity dependences on excitation power for the exciton and biexciton, respectively, in the low excitation regime, and (iii) linear counter-polarization of the exciton and biexciton split emission lines along the [110] and [1-10] directions.

Exciton and biexciton emission of eleven individual QDs with different emission energies have been identified by this procedure in order to determine the dependen-

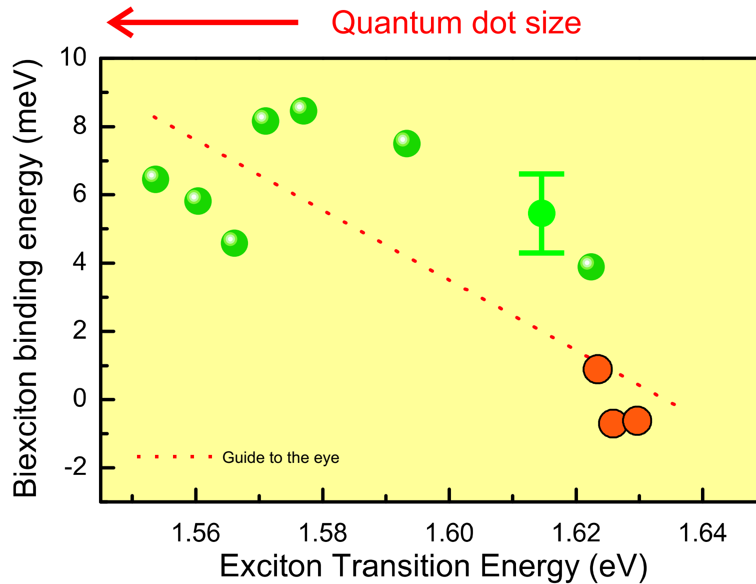

Figure 4.1: Dependence of the biexciton binding energy on the exciton emission energy. Very large values up to 9 meV are observed. The biexciton binding energy decreases with increasing emission energy, and vanishes at about 1.63 eV. For the dots marked with filled circles no splitting could be measured, making difficult the reliable assignment of the biexciton peak, which was only determined by the excitation power dependence. For the data point with an error bar, several peaks were candidates for being biexcitons. The dashed line serves as a guide to the eye.

cies of BBE and FSS on the QD exciton emission energy. It is assumed, as a first approximation, that the exciton ground state emission energy reflects the QD size.

4.3 Results: Biexciton binding energy

The results for the biexciton binding energy is shown in Figure 4.1. The main result is the decrease of the biexciton binding energy with the exciton emission energy and its vanishing at the highest exciton energy measured (1.63 eV). This trend is the same as in InAs dots with GaAs barriers [144, 173] and in annealed InAs QDs (for the high emission energy regime) [189], although the observed values for the biexciton binding energy are essentially larger (up to 9 meV) than the common values reported for GaAs barriers (2-3 meV). The three orange points at the higher emission energies correspond to QDs whose fine-structure splitting was too small to be resolved. In these cases only criteria (i) and (ii) were used to identify the exciton and biexciton

lines of a single dot. The value of the biexciton binding energy is determined by the Coulomb interactions and more specifically by correlation between electrons and holes. It has been shown experimentally [144, 173] and theoretically [144, 173, 174] that the biexciton binding energy can vanish and change its sign depending on the dot size. A state with negative binding energy can exist because of the three dimensional confinement. Antibinding of the biexciton ground state is expected to occur in small dots when the number of bound states decreases, thus reducing the correlation energy [173]. In the present case the high AlAs barriers result in a stronger exciton confinement and more bound states in the QD. Calculations show that the trend is dominated by the variation of the number of confined hole states, while the number of electron states has no impact on the BBE [173]. The observed trend in our dots can be thus attributed to varying correlation effects due to the changing number of confined hole levels.

The observed BEE values up to $\Delta E_{XX} = 9$ meV are extremely large compared to the usually reported values for the commonly studied In(Ga)As/GaAs QDs, as stated above. Comparatively large values of $\Delta E_{XX} = 4.6 - 5.14$ meV were also reported for large (30-100 nm) InGaAs/AlGaAs QDs [142] and 5 meV for $Al_{0,36}In_{0,64}As/Al_{0,33}Ga_{0,67}As$ QDs [190]. Although these systems contain aluminum in the barriers, too, correlation might be enhanced in these dots due to the lower sub-level spacing (large dots and shallow dots compared to InAs/AlAs QDs, respectively). In our dots the barriers are nominally pure AlAs. Thus the higher biexciton binding energy can be attributed to increased correlation, which in turn is enhanced due to a larger number of confined states rather than a reduced sub-level spacing.

4.4 Results: Fine-structure splitting

Large values of the FSS up to 0.3 meV are observed in our dots, similar to 0.5-1 meV for $InAs/Al_{0.6}Ga_{0.4}As$ dots [17] and to recently reported values up to 0.52 meV for InAs/GaAs QDs (CL) [184]. This is larger than the usually reported values up to 0.2 meV for In(Ga)As/GaAs QDs [59, 149, 158, 187, 189].

The variation of the fine-structure splitting Δ_{FS} with the QD exciton emission energy is shown in Figure 4.2. The value of the FSS decreases with the exciton emission energy and vanishes at roughly the same energy as the BBE. The decreasing trend

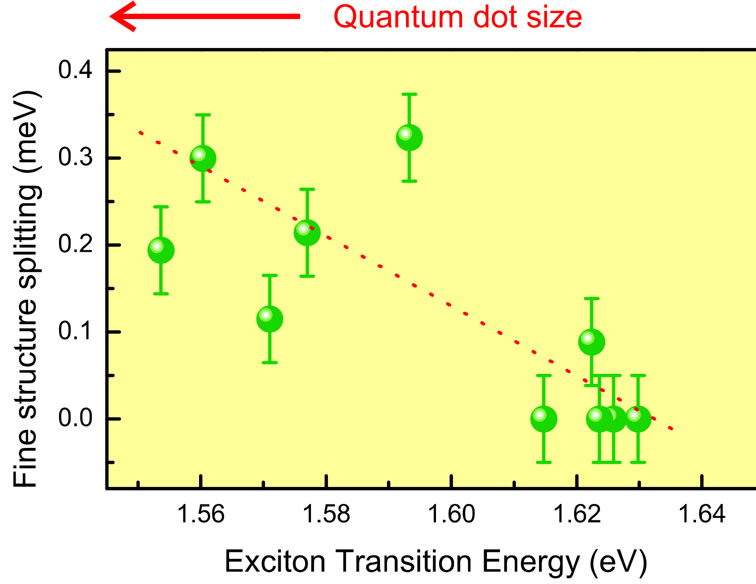

Figure 4.2: Dependence of the bright exciton fine-structure splitting on the exciton recombination energy. Large values of the splitting up to 0.3 meV are observed. The splitting decreases with increasing emission energy, and vanishes at about 1.63 eV. The dashed line serves as a guide to the eye.

suggests a possible splitting reversal for emission energies above 1.63 eV. Such sign reversal has been predicted for InGaAs/GaAs QDs [92] of changing size and recently reported experimentally in InAs/GaAs QDs [146]. No effect of the QD density on the FSS has been observed in the investigated sample, so that any influence of interdot interactions on the FSS is excluded. Three different possibilities have been given as the origin of the exciton fine-structure splitting, which are not mutually excluding: (a) electron-hole exchange anisotropy induced by lateral dot elongation [17, 145] (see also section 3.7) , (b) potential anisotropy due to strain-induced piezoelectric fields [182–184], and (c) intrinsic anisotropy of the atomic structure [92, 174, 185]. The latter is predicted to be a rather small effect in the order of few μeV and independent from the dot shape, and cannot therefore account for the trend. Although both, piezoelectricity and structural elongation introduce anisotropy in the confining potential, the influence of these mechanisms on the wavefunctions is different. Piezoelectricity accommodates the electron and hole wavefunctions orthogonally in the dot, while the elongated dot shape forces the wavefunctions to be orientated parallel [184]. Consequently different effects of both mechanisms have to be expected. The dot elongation

mechanism predicts larger FSS in smaller dots [145, 184] and is therefore unlikely to account alone for the sign reversal. The piezoelectric mechanism implies elongation of the electron and hole wave functions along (110) and (1-10) directions, respectively, for pyramid-shaped QDs [183]. As this elongation is hindered in small QDs, FSS is expected to decrease for decreasing dot size. A mixture of these mechanisms has been invoked to explain the experimental results on InAs/GaAs QDs [146]. An atomistic calculation also predicts a decrease of the FSS for decreasing dot heights in lens-shaped circular dots [185]. Similar arguments are given to explain the dependence of the FSS ($\Delta_{FS} = 0.5 - 0.1$ meV for $E_X = 1.05 - 1.35$ eV) on the exciton energy observed for InAs/GaAs dots by cathodoluminescence [184]. The calculations of [184] (8 band $\mathbf{k{\cdot}p}$ and configuration interaction method) show a decrease of the FSS for decreasing dot size for square based pyramids including piezoelectricity, whereas the FSS increases for decreasing size of [1-10]-elongated dots (negative sign for [110]-elongated dots). Therefore, the observed trend is attributed to a decisive impact of the piezoelectric mechanism on the size-dependence of the FSS.

The effect of piezoelectricity on the p-state splitting for varying size and shape was calculated for InGaAs QDs [191]. The p-state splitting is a measure of the confinement anisotropy between the [110] and [1-10] directions and thus dependencies of the p-state splitting can be applied to the FSS, too [191]. It is shown that for increasing size of pyramidal dots the p-splitting increases, and by including second order piezoelectric effect the splitting is further slightly enhanced. Furthermore, by increasing the vertical aspect ratio (height/base length) the p-state splitting increases, too. It has been shown that a larger QD volume involves larger vertical aspect ratios for both InAs/GaAs [73] and InAs/AlAs QDs [24]. Thus, both trends should combine to an increased effect.

The trend of Figure 4.2, similar to previous results in InAs/GaAs dots [146, 184], where sign reversal of FSS has been found, allows to assume that the piezoelectric mechanism is the origin of the results for the InAs/AlAs QDs, too.

Although a clear trend to vanishing FSS can be observed, the data exhibits a large scatter. The ground state emission energy does not depend on a unique parameter as the QD height or QD volume, since shape variations and composition fluctuation also alter the emission energy. The large scatter of the data in the plot as function of the exciton emission energy can be consequently attributed to the

imprecise approximation of relating the QD size with the emission energy. Similar arguments hold for the scatter of BBE data, too. Besides the common trend of the FSS for different dot samples (or sample series), there is apparently a tendency to large FSS for samples that contain aluminum in the matrix. The small number of studies on such dots include, the presently investigated InAs/AlAs QDs with FSS up to 0.3 eV, InAs/$Al_{0.6}Ga_{0.4}As$ QD with FSS of 0.5-1 meV (tentatively attributed to shape anisotropy and enhanced confinement due to the barriers) [17] and InAs/$Al_{0.3}Ga_{0.7}As$ QDs with FSS of 0.3 and 0.4 meV (the origin is left open in this work) [102]. Concerning the QD shape, in the case of InAs/GaAs QDs the top part of the dot disappears during the capping process, whereas this effect is reduced in the case of InAs/AlAs dots [33]. Therefore, InAs/AlAs dots should exhibit a larger vertical aspect ratio, what in turn also implies larger splittings due to the piezoelectric effect [191]. Reduced intermixing in InAs/AlAs QDs compared to InAs/GaAs QDs [33] also leads to higher strain fields (larger lattice mismatch) that can enhance the piezoelectric effect. Furthermore, an increased piezoelectric effect may be expected from the almost twice as large difference of the piezoelectric constants for InAs/AlAs: $e_{14,InAs} - e_{14,AlAs})/(e_{14,InAs} - e_{14,GaAs} \approx 2$ with the values for bulk $e_{14,InAs} = -0.045$, $e_{14,AlAs} = -0.23$ and $e_{14,GaAs} = -0.16$ C/m^2 [111].

Moreover, the simultaneous vanishing of the FSS and BBE around 1.63 eV strongly suggests a common origin: The spread of carriers out of small dots due to reduced confinement seems to account for a simultaneous reduction of exchange and correlation terms, leading to the decrease of the FSS and BBE, respectively.

4.5 Conclusion

In photoluminescence spectra of InAs/AlAs quantum dots both the fine-structure splitting of the exciton level and the biexciton binding energy decrease for increasing exciton emission energy (decreasing dot size), disappearing around 1.63 eV. These effects possibly originate in the spread of carriers out of small dots due to reduced confinement. In comparison with InAs/GaAs quantum dots, a larger biexciton binding energy (up to 9 meV) and a larger fine-structure splitting of the bright exciton state (up to 0.3 meV) are observed and may be attributed to a larger confinement due to the higher AlAs barriers and to increased piezoelectric effects.

Chapter 5

Vibrational properties

The understanding of exciton-phonon interactions in quantum dots is of fundamental interest for applications in both traditional optical devices and future quantum devices. These interactions influence the optical efficiency via phonon-assisted charge carrier relaxation, but also produce dephasing of the exciton states. This chapter contains three sections with experimental results in single quantum dots addressing different aspects of the interaction of the QD exciton with phonons. The first two sections present micro-PLE measurements. In the first one, broad resonances in the excitation spectra are interpreted in terms of the formation of polaron states. Secondly, all longitudinal-optical phonons of the InAs/AlAs QD-barrier system are identified in the excitation spectra. In the last section a micro-PL study for varying temperature and excitation intensity is presented. Different coupling mechanisms (namely, deformation potential and piezoelectric) for the exciton-acoustic phonon interactions are identified. In the following the common context of the different results is shortly introduced. Different effects on the interaction with phonons are expected for excitons localized in QD compared to excitons in higher dimensional systems:

(i) In higher dimensional systems lifetime shortening due to phonon-assisted scattering into higher states results in a broadening of the emission line. In QDs temperature-dependent broadening due to scattering by optical phonons is reduced due to the lack of states with suitable energy (A reduced temperature broadening coefficient is measured in section 3.4).

(ii) A reduced number of radiative transitions may be expected in 0D systems due to selection rules, which depend on the confining potential symmetry. Furthermore,

the discrete density of states of QDs compared to the continuous DOS of higher dimensional systems slows down carrier relaxation at low temperatures, due to the mismatch between the phonon energies and the energy differences between the QD excited and ground states. This is the so called phonon bottleneck effect [192–194].

(iii) Moreover, since Fröhlich coupling is proportional to the electron-hole separation, one might expect reduced exciton coupling to LO phonons due to confinement-induced local charge neutrality [195]. However, in self-assembled QDs an either vertical or in-plane asymmetric shape leads to [182] different vertical/lateral distributions of the electron and hole wavefunctions, which would enhance the exciton-phonon interaction by Fröhlich coupling (but simultaneously the oscillator strength decreases due to reduced overlap of the wavefunction) [196]. Vertical displacement of the electron and hole wavefunctions has been demonstrated for field-effect samples containing self-assembled InAlAs/AlGaAs QDs [197] and InAs/GaAs QDs [198], They exhibit nonzero Stark shifts at zero-electric field implying a permanent dipole moment of the QDs. Further enhancement of the Fröhlich coupling may be due to piezoelectricity [196]. Additionally, the failure of the adiabatic approximation, which neglects the mixing of excited states by the interaction with phonons may be relevant and lead to an enhanced coupling and even to polaron formation. The interactions with phonons are described theoretically (in the weak coupling regime) in the framework of the Huang-Rhys theory of F-centers (also named offset harmonic oscillator model, and is equivalent to the independent boson model [195, 199–201]) Processes involving phonon absorption or emission as part of the optical transition give rise to phonon replicas. For optical phonons this replicas of the ZPL are spaced by the optical phonon energy. The interaction of the QD exciton with acoustic phonons causes similar satellites, but the quasi-continuum of acoustic phonon modes overlap and give rise to broad wings around the ZPL at low temperatures or to a broad peak at elevated temperatures (this peak adds to the lifetime-broadening due to scattering). However, regarding the coupling to LO phonons, experiments often exhibit phonon satellites in the PLE but not in the PL spectra. This points to a enhanced exciton-phonon coupling in the case of the phonon-assisted generation of excitons (absorption) in comparison to phonon-assisted recombination of excitons (emission).

For example, size-selective macro-PL and macro-PLE measurements on InAs/GaAs QDs (Figure 2 of [196]) indicate a stronger coupling for phonon-assisted absorption

than emission (exciton recombination). In this experiments the excitation on the ensemble PL peak leads to a small 1LO sideband corresponding to phonon-assisted emission, but excitation at 1LO energy above the PL peak results in a strong resonance that corresponds to phonon-assisted absorption. Likewise for InAs/GaAs QD ensembles [202], the resonantly excited PL spectra exhibit sharp 1LO and 2LO phonon replicas below the maximum of the macro-PL emission, and is interpreted as phonon-assisted emission in the adiabatic regime. However, for excitation above the ensemble PL peak, broad peaks separated by multiples of the phonon energy are observed and attributed to phonon-assisted absorption with non-adiabatic coupling (mixing of states). Intense replicas of the InAs 1 LO and 2 LO phonon was observed InAs/GaAs QDs [203] in PLE (absorption) but not in PL (emission). This was interpreted by exciton mixing with nearly resonant states (i.e. breakdown of the adiabatic approximation). The authors propose that such resonant mixing cannot occur in emission since there are no states below the zero phonon line energy. This two situations are shown schematically in Figure 5.1 where only the emission of phonons is considered at low temperature.

Furthermore, strong non-adiabatic electron-phonon coupling can lead to the admixture of electrons and phonons forming polaron states. Phonon-phonon interactions on the polaron state [204] allow a large energy window for the relaxation mechanism. This large energy window around the LO phonon energy is due to the anharmonic decay of the polaron (into two acoustic phonons) and leads to an efficient carrier relaxation mechanism, circumventing the predicted phonon bottleneck [192]. Thus, also for large detuning of several meV around the LO phonon energy the carrier relaxation remains phonon assisted, and leads to broad resonances in the PLE spectra. Such broad PLE resonances have been observed in InAs/GaAs QDs, but not always they were attributed to polaron decay. Instead, contributions of different phonon modes (interface, strain inhomogeneity, wetting layer) were sometimes proposed to explain the broad PLE peaks [135, 205, 206]. Polaronic behavior has been revealed by size-selective resonant excitation in nanocrystals [207], time-resolved measurements [208–211], resonant Raman scattering [212] and far-infrared magneto-absorption [213].

To complete the above discussion related to LO phonons, the last section 5.3 of this chapter treats acoustic phonons, which indeed are observed clearly in the PL

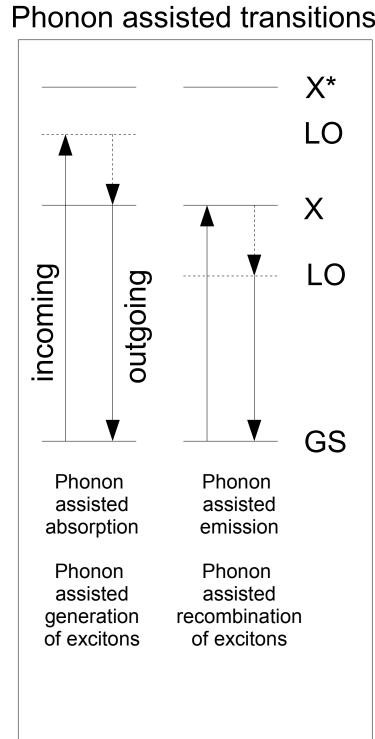

Figure 5.1: Phonon-assisted absorption and emission processes are schematically shown. Only the emission of phonons is considered at low temperature. In the absorption process the excitation is close to an excited state, whereas in the emission process no such resonance can occur. This might lead to mixing of states (non-adiabatic coupling) in the first case and explain why phonon features are seen in PLE but not in PL spectra.

spectrum (phonon-assisted emission) of a single QD. Thus the adiabatic approximation describes well the system in this case. Since at low temperatures phonons are mainly emitted, wings appear on the low-energy side, but for higher temperatures also the absorption of phonons is observed as high-energy wings.

5.1 AlAs-like LO-phonon and Intermixing

Excitations of a single InAs/AlAs self-assembled quantum dot were investigated by photoluminescence excitation spectroscopy. Resonant absorption assisted by longitudinal-optical (LO)phonons of the quantum dot and the barriers is observed. In particular, a resonance at 41 meV is attributed to the AlAs-like mode of InAlAs with low Al

content. Our results constitute a direct optical measurement of the intermixing (estimated below 10 %) in a single quantum dot. They also demonstrate that all LO phonons of this mixed quantum dot system couple to the exciton states. [1]

5.1.1 Introduction

The study of the properties of individual semiconductor quantum dots [44, 45, 59] (QDs) is of great interest for application in classical and quantum [6] light emitters and detectors as well as for the implementation of quantum information processing systems. [172] Although these applications require very different conceptual approaches toward devices, the understanding of the scattering mechanisms is of fundamental importance in all cases. Indeed, they are crucial to obtain fast carrier capture, efficient carrier relaxation, and long recombination lifetimes. In self-assembled QDs (SAQDs), the strong exciton-phonon coupling leads to the formation of polaron states, [193, 214–217] whose decay into acoustic phonons is a major contribution to relaxation (see section 5.2). Phonons in SAQDs can be studied by optical techniques, as reported in photoluminescence (PL), PL excitation (PLE), and Raman measurements. [205, 206, 218, 219]

In this work, PL and PLE data on InAs/AlAs SAQDs are reported, where strong confinement results in a single electron state localized in the QD. In these QDs, carrier relaxation would be expected only by direct scattering from the continuum of extended excited states to the ground confined state. However, it is shown that PL emission is enhanced by resonant excitation involving different longitudinal-optical (LO) phonons in the system. One of these phonons is the high-energy mode of AlInAs for low Al concentration. This result demonstrates the presence of Al intermixing in the InAs QDs, detected by means of optical measurements. The results also show that both intra dot and barrier optical phonons are coupled to the excitonic states and contribute to their relaxation.

[1] Part of these results were published in Appl. Phys. Lett. 92, 181909 (2008) and Physica E 40, 2172-2175 (2008)

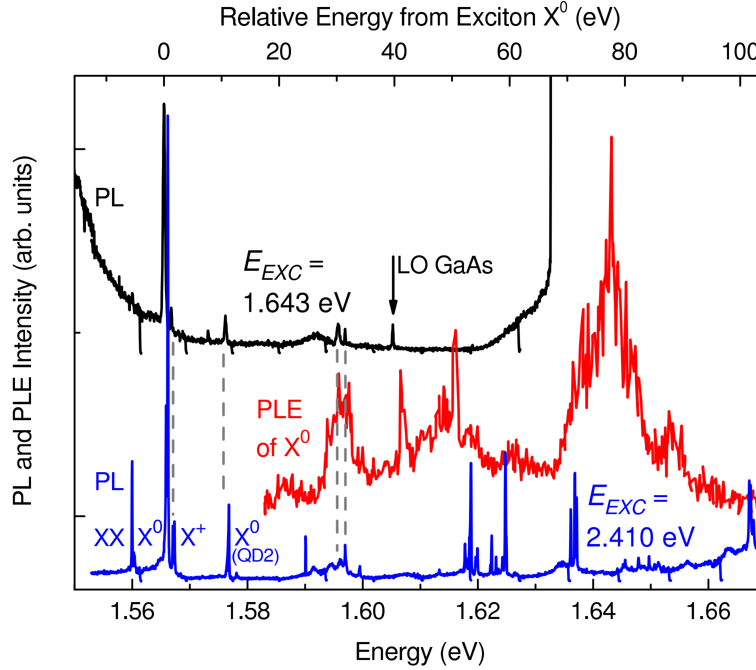

Figure 5.2: Resonantly (1.64 eV, black) and non-resonantly (2.41 eV, blue) excited PL. The marked peaks are the exciton X0, biexciton XX and probably the trion X+ of the same QD. Peak labeled QD2 comes from a different QD. The PLE spectrum of X0 (red curve) shows the phonon resonances discussed in the text.

5.1.2 Experiment

Details of the sample [67] are described in section 2.2.2. All the measurements were taken at 9 K. More details on the setup are given in section 2.1).

5.1.3 Results

The PL spectra of a single QD emitting at 1.565 eV is shown in Figure 5.2 for resonant (1.643 eV) and nonresonant (2.410 eV) excitation. The low-energy peaks in both spectra correspond to emissions of the exciton (X0), biexciton (XX) and most probably trion (X+) of a single QD, together with an exciton X0 (QD2) belonging to a different dot. Peaks of the same QD were identified by their jitter pattern, polarization, and power dependence, as described in sections 3.5, 3.7 and 3.6, respectively. The peaks at higher energies probably belong to different QDs except the ones around 1.597 eV, which also appear in the PLE spectrum shown in Figure 5.2

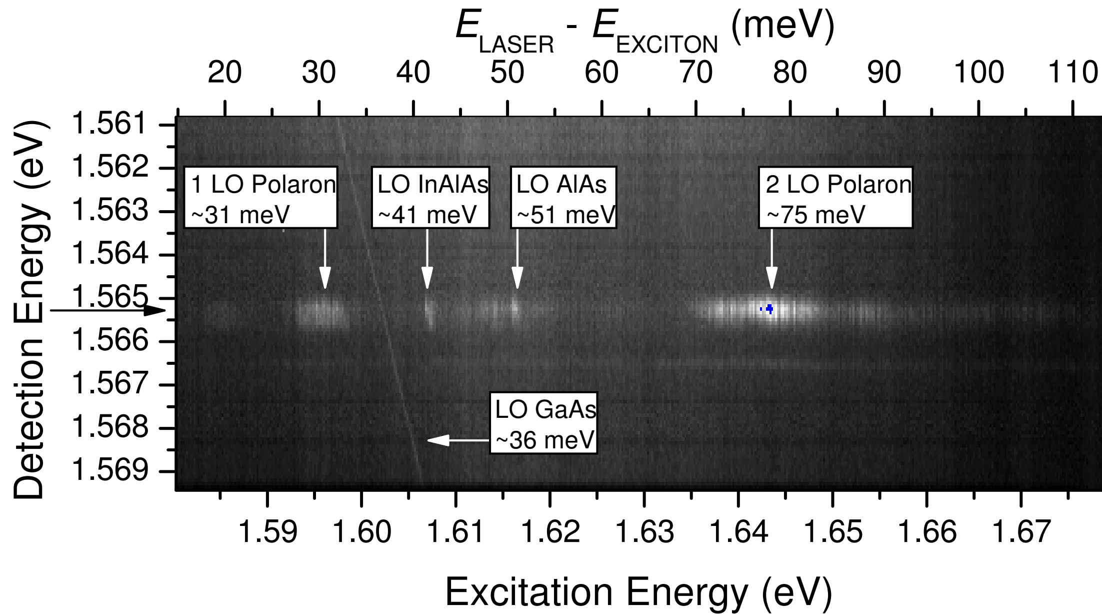

Figure 5.3: Photoluminescence intensity gray-scale plot. The y and x axes show the detection and excitation energy, respectively. The relative excitation energy above the exciton emission at 1.5655 eV (marked by a black arrow in the left axis) is shown on the top axis. Two broad and two narrow resonances can be observed. The horizontal cut at the black arrow corresponds to the red PLE curve in Figure 5.2. The diagonal line is the bulk GaAs LO phonon that shifts parallel to the laser energy.

(red curve). The PLE spectrum in Figure 5.2 corresponds to a horizontal cut at the detection energy indicated by the black arrow in the intensity scale plot shown in Figure 5.3. The PLE spectrum exhibits two broad resonances at 31 and 75 meV, as well as two narrow ones at 41.3 and 51 meV. All these resonances are attributed to phonon assisted absorption or Raman scattering processes.

The PL peaks at 31 and 32 meV (relative energy, upper scale) in the PL spectra coincide with the broad PLE resonance. In accordance to the study presented in section 5.2, they are attributed, likewise the PLE peak at 75 meV, to polaron states [193, 209, 212, 220, 221] formed by the QD InAs LO phonon [182, 205, 206, 218, 222], and perhaps interface (IF) phonons [30, 223].

In the following, the resonance at 41.3 meV is discussed. Figure 5.4 depicts a series of PL spectra obtained for excitation energies varying roughly in 0.17 meV steps from 40.5 to 42.0 meV above the fine-structure split exciton transitions at 1.5655 eV. Left and right panels correspond to polarization emissions parallel to the crystallographic

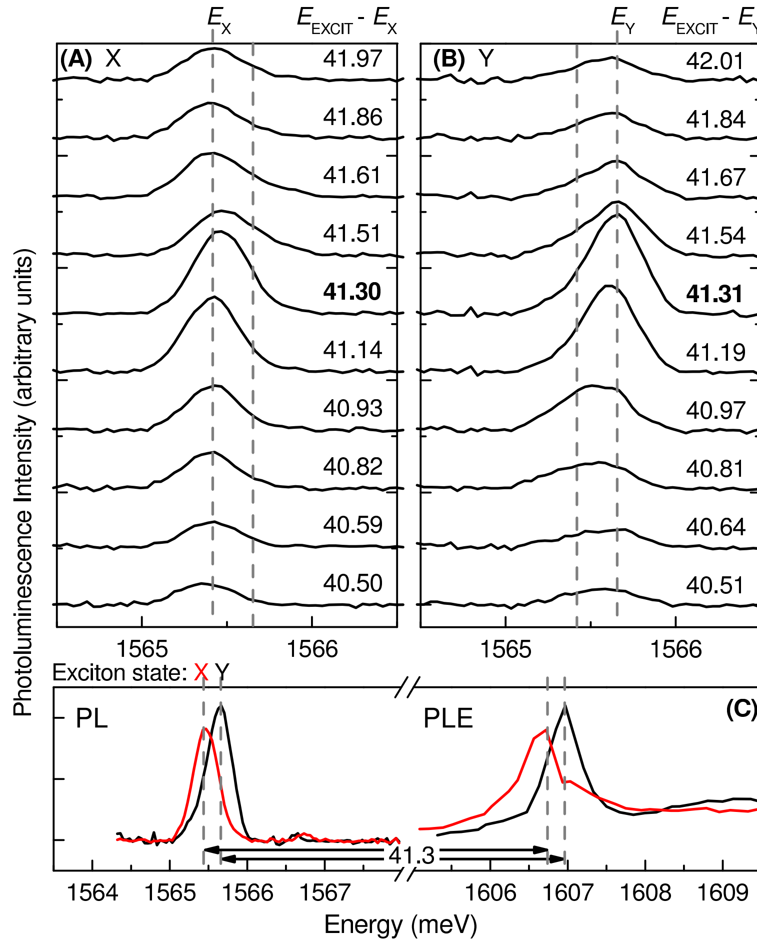

Figure 5.4: Polarization resolved PL spectra for varying excitation energies. Left and right panel show the linearly counter-polarized exciton states X and Y respectively. Bottom panel: The fine structure split exciton lines X and Y resonate for excitation at 41.3 meV above the respective emission lines.

directions (110) and (1-10) (labeled X and Y), respectively. In each panel, only the corresponding component of the split exciton (X,Y) is observed. As the laser energy is increased, both exciton PL transitions and the trion X+ at 1.5668 eV (not shown in this figure) experience successive intensity enhancements. The bottom panel of Figure 5.4 shows the PL and PLE spectra of transitions X and Y. One sees that the resonance at 41.3 meV is common for both X,Y exciton components and that the fine-structure splitting is well resolved in PLE.

The top panel of Figure 5.5 shows a waterfall plot of the unpolarized PL spectra for varying excitation energy. The unpolarized PL intensity of these spectra is plotted

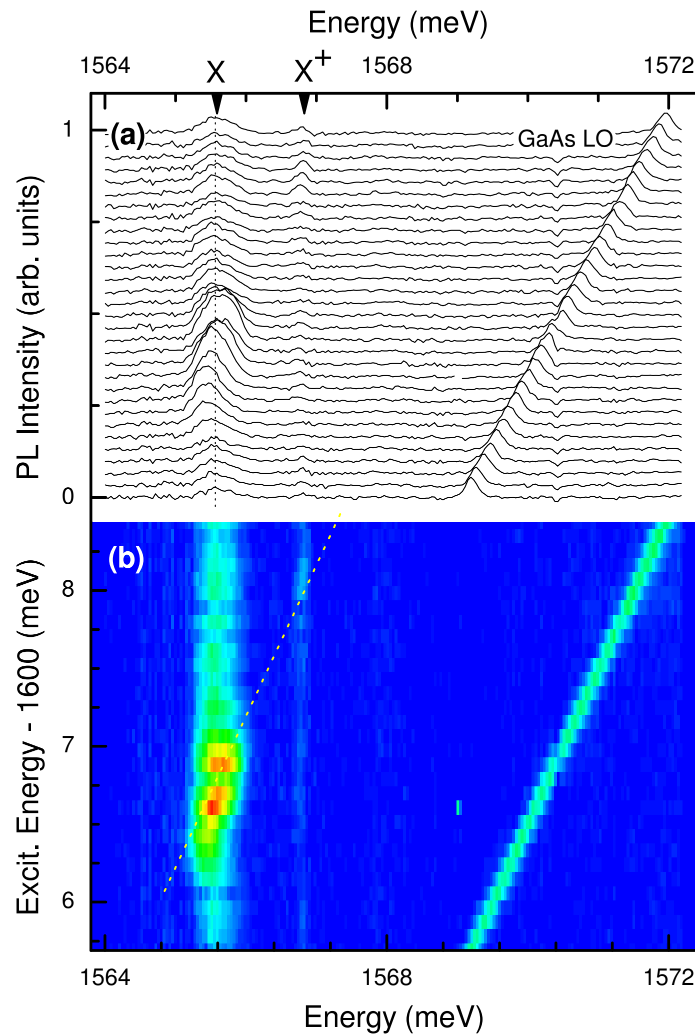

Figure 5.5: (a) Waterfall plot of unpolarized PL spectra for varying excitation energy from 1.6057 to 1.6084 eV. (b) Intensity scale plot of the PL spactra from (a) in function of excitation and detection energy. The dotted line is 41.3 meV below the laser energy. Notice that also the trion X+ resonates at the same excess energy.

as color scale in the bottom plot versus detection and excitation energy. Horizontal and vertical cuts correspond to PL and PLE spectra, respectively. The dotted line indicates an energy of 41.3 meV below the excitation energy. The resonances of the split exciton and the trion (clearly seen in this plot) are observed when the excitation and emission energies differ by 41.3 meV. The emission parallel to the dotted line at the right hand side of Figure 5.5 is the LO phonon of the GaAs substrate. Excited

states as the origin of the resonances at 40 meV (References [218] and [206]) are excluded due to the high AlAs barriers. The excitation at 41.3 meV is attributed to a phonon that "moves" parallel to the excitation energy, as the bulk GaAs-LO one, and successively resonates with the three PL lines of the QD. One might discuss whether the resonance is due to phonon assisted absorption or to resonant Raman scattering. In the latter case, one should resolve the phonon peak from the PL emission by slightly detuning the excitation energy from the resonance. However, the small width of the resonance (0.4 meV, comparable to the phonon line width) makes this impossible in the present case, and both processes become indistinguishable. The relevant phonons of InAs/AlAs QDs are LO, TO and IF modes, whose energy ranges in unstrained materials are 27-30 meV for InAs and 45-50 meV for AlAs, respectively. For fully strained AlAs (matching the InAs lattice parameter), the range is 41-43 meV (Ref. [223]) while the LO frequency for strained InAs is around 32 meV [182, 222]. The only candidate for the 41.3 meV phonon would be the TO mode of fully strained AlAs. However, this is unlikely, as the coupling of TO phonons to excitons is much weaker than the LO one and AlAs barriers are expected to be essentially unstrained. These arguments also rule out the AlAs-like IF modes [30]. Instead, the single QD excitation responsible for the PLE resonance at 41.3 meV is attributed to the AlAs-like LO mode of the InAlAs ternary compound. This implies an Al concentration of less than 10% in the here studied QDs [224]. The occurrence of Al-In intermixing in similar QDs was evidenced by tunneling microscopy [33]. This small Al concentration does not change the InAs-like phonon frequency, as it is essentially independent on composition [224]. AlAs- and InAs-like modes have been observed also in ensembles of AlInAs/AlGaAs QDs [38] by size-selective resonant phonon excitation. Finally, the resonance at 51 meV in Figure 5.2 corresponds to the unstrained AlAs LO phonon of the QD barriers. It can couple to the exciton due to the wave function leaking into the barrier. Barrier phonons have been widely reported for QDs embedded in GaAs [205, 206, 218, 219].

To get a deeper insight into the scattering mechanism, the PL polarization properties of the 41.3 meV resonance are analyzed. In Figure 5.6, the four polarization configurations are plotted for excitation near the Y exciton resonance. The emission is much more intense for Y than for X polarized excitation, regardless of the emission polarization. This difference points to a broken symmetry of the QD states in

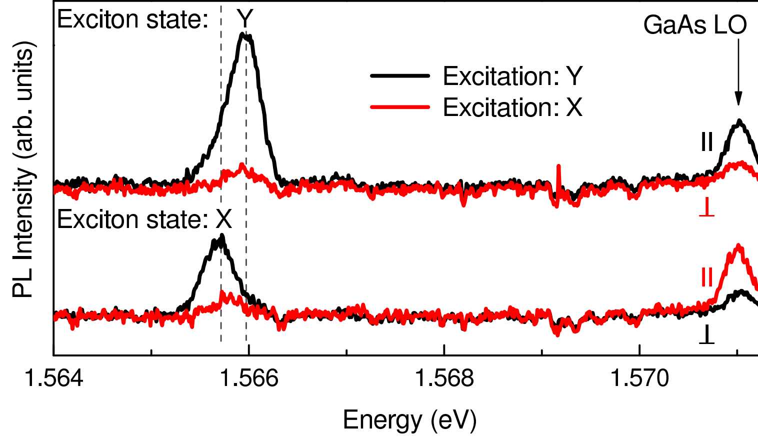

Figure 5.6: Polarization resolved PL spectra for excitation near the Y exciton resonance. Both X,Y exciton states can mostly be observed for Y polarized excitation

the (110) and (1-10) directions, probably due to the anisotropy of the piezoelectric potential. As this anisotropy can split the excited-hole states of up to several tens of meV [182], one can speculate that one of the split excited-hole states is situated closer to 41 meV, above the ground HH state than its counterpart. This would favor the excitation in a doubly resonant process for one polarization (Y), as observed. In the relaxation process, scattering by the LO phonons results in ground state excitons with both X, Y symmetries. The interpretation of a close-lying excited state is in accordance with the fact that the phonon resonance is only observed in absorption (PLE) but not in emission (PL). As discussed in the introduction of this chapter this implies an important contribution of excited states in the absorption process [203].

5.2 InAs-like LO-phonon and polarons

In this section we present evidence of polaronic coupling between the exciton and the LO phonon of an InAs/AlAs quantum dot, different from the one studied in the previous section. This is observed in the excitation spectra of the biexciton line in a single quantum dot, which shows marked maxima at the quantum dot LO frequency and at its first overtone. The quantum dot phonon energy observed is 31 meV.[2]

[2]Part of these results were published in Phys. Rev. B 71, 81302(R) (2005) and AIP Conf. Proc. 772, 715 (2005)

5.2.1 Introduction

Carrier confinement in three dimensions can give rise to strong polaronic coupling [193, 208, 221, 222, 225, 226], which has a strong influence on the QD optical properties. Strong polaronic coupling of the electronic states to optical phonons has been demonstrated to be the origin of carrier energy relaxation in QDs, even for large detuning of the electronic intersublevels from the phonon energy [208]. At difference of the pure exciton state, which would have very long decay time, the polaron [221] decays efficiently by anharmonic coupling to bulk acoustic phonons [204, 214]. Most of the work published so far on polaronic coupling in QD involves InAs QDs embedded in GaAs barriers. In these systems, phonons of the InAs or InGaAs QDs are close in energy to the GaAs-LO one, because of strain and intermixing. Therefore, interaction effects are expected between QD phonons and barrier ones, which can affect the polaron formation and its decay time. Indeed, phonons associated to InAs QDs, to its interface, to the wetting layer, and to the GaAs barrier have been reported in photoluminescence excitation [206, 222, 225] and Raman scattering [30, 227] experiments in QDs or in calculations [226].

This situation may be changed by using a higher gap barrier as AlGaAs [17] or AlAs [34, 67]. Higher barriers have several advantages, as an increase of the carrier confinement, shifting the QD emission to higher energies. Also, the use of a harder barrier material as AlAs suppresses possible coupling of the QD optical phonon to the barrier ones, what can result in a slower polaron decay. Extremely long decay times (microseconds) in ensemble-averaged InAs/AlAs QDs have been reported [34, 77] for high energy excitation. They have been attributed to spatial separation of electrons and holes in neighboring QDs caused by scattering of InAs Γ-band electrons into the AlAs X-band.

In this section PL and PLE intra-dot measurements on a single InAs/AlAs QD are presented. The PLE spectra of the exciton and biexciton lines of a single QD display strong resonances at energies multiple of 31 meV. This energy corresponds to the optical phonon confined in the quantum dot. The resonances are particularly strong for the biexciton emission and are interpreted in terms of the polaron formation in the QD.

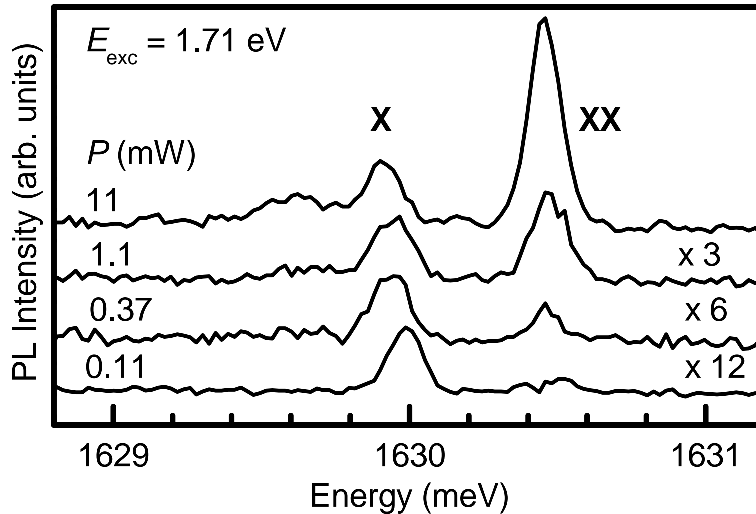

Figure 5.7: Excitation power dependence of two peaks in the PL of a single quantum dot, normalized to the X peak intensity. For excitation power below 1 mW the X and XX peaks grow as P^α with α = 0.5 and 1.5 and are attributed to the exciton and biexciton respectively (see text).

5.2.2 Experiment

The micro-PL measurements were performed with the setup described in section 2.1. The PL emission was excited with either an argon-ion or a Ti-saphire laser with a typical power density on the sample of 10^4 W/cm^{-2}. This rather large excitation power was necessary to compensate the low light intensity collected from the dots. All the measurements presented were taken at 8 K.

5.2.3 Results

The emission spectra of a single QD are shown in Figure 5.7 for different excitation power P. The enlargement factors are indicated and spectra are shifted vertically for clarity. For excitation power below 1 mW the intensities of the peaks labeled X and XX grow as P^α with α = 0.5 and 1.5 respectively. The expected exponents for the exciton (X) and biexciton (XX) lines at low excitation are $\alpha = 1$ and $\alpha = 2$ respectively, see section 3.6. These values decrease at high excitation levels [142, 144]and consequently the peaks in Figure 5.7 are assigned to the exciton and biexciton. The fact that the biexciton appears at higher energy than the exciton is related with the actual shape of the dots and with the details of the confining potential [144]. This is

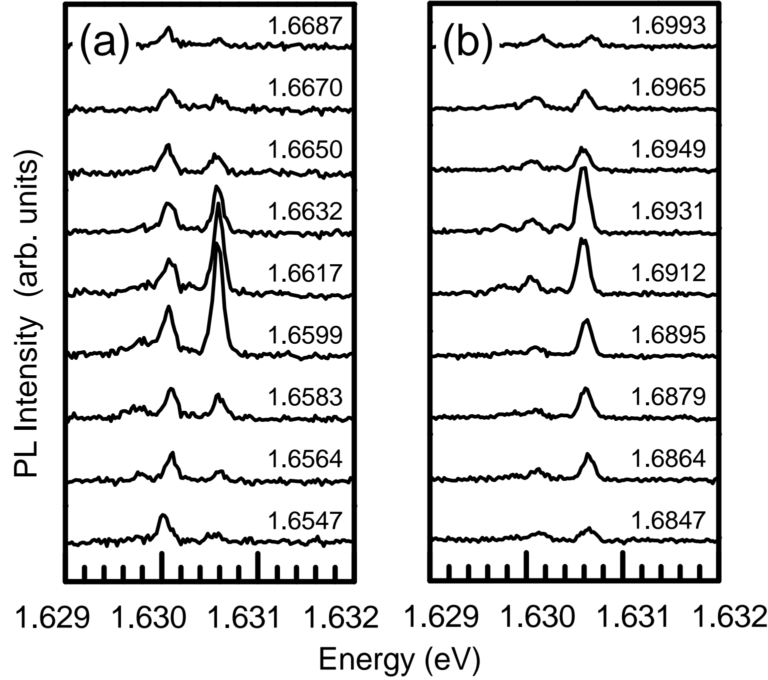

Figure 5.8: Waterfall plots of the X and XX emission (see Fig. 2) for varying excitation energy E_{exc} which is indicated in eV. In (a) the 1LO polaron state is excited, in (b) the 2LO polaron state.

discussed further in section 4.3.

The intensities of the X and XX emissions change drastically upon changing the excitation energy. This is shown in Figure 5.8, where the PL spectrum of the QD is presented for excitation energies varying from 1.655 to 1.669 (a) and from 1.685 to 1.699 eV (b) in steps of one meV approximately. Besides the small energy fluctuations due to jitter, one observes strong intensity increases, particularly in the XX peak, for certain excitation energies.

This is also clearly seen in Figure 5.9, where the PL spectrum of the dots for an intra-dot excitation energy of 1.71 eV (upper curve) is presented with the PLE spectrum of the XX line. The detection energy is indicated by an arrow. There are two strong and rather broad PLE peaks at 31 meV and 62 meV, the former also observed in the PL spectrum. Narrow PLE lines, which are frequently observed in PLE spectra of InAs/GaAs single QDs [142, 206, 219] are missing in the present case. Relatively broad (around one meV) PLE peaks in the range of 29 to 31 meV have been reported in InGaAs QDs [206] and attributed to exciton-LO phonon coupling in

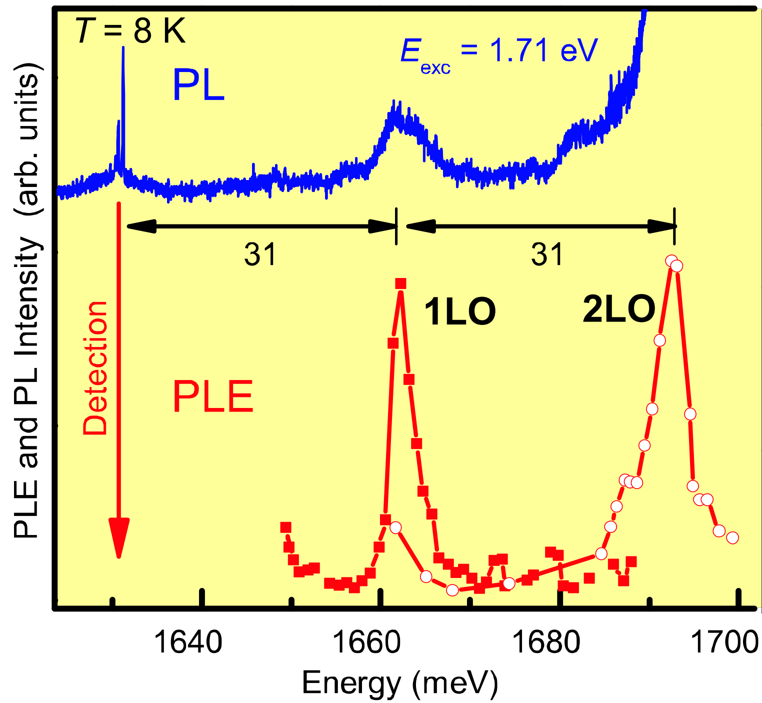

Figure 5.9: PL (E_{exc} = 1.71 eV) and PLE spectra of the XX peak (see Figure 5.8). PLE reveals polaron states, separated by the phonon energy of the dot (31 meV) which is close to the bulk InAs LO phonon frequency. Squares and circles correspond to two different experimental runs. At 1 LO the polaron state is also observed in PL.

the dots. Also ensemble-averaged PL [222, 225] and Raman [30, 227] measurements indicate phonon energies in the same energy range. Therefore the PLE peaks in Figure 5.9 are ascribed to transitions involving polaronic states due to the coupling between the QD electronic states and the phonon. The broad peaks observed at 31 and 75 meV in the PLE spectrum of the QD studied in the previous section 5.1 are attributed also to polaronic coupling. Differences in QD size, aspect ratio or strain can shift the energy of the polaron states away from exact multiples of the LO energy [216, 221] The QD phonon energy in this case is 31 meV, i.e. 1 meV above the bulk InAs LO energy. The difference can be roughly accounted for assuming full hydrostatic deformation of the QD to match the AlAs lattice parameter. Confinement is expected to have a moderate effect on the phonon energy in the investigated QD due to the slow dispersion of the InAs LO phonon at low wave-vector. A rough estimate considering the dot height of 3 nm gives an energy decrease of the order of 1 meV. Consequently, the effect of strain is probably stronger than the previous

simple estimate considering only hydrostatic deformation. Aluminum diffusion into the QD would also result in an increase of the phonon frequency. In the present case this effect is negligible due to the low growth temperature. In fact 5% of aluminum in an unstrained QD would produce an energy increase of the phonon energy in this range. This was confirmed in the previous section 5.1, where the presence of a small amount of aluminum in the QD is demonstrated by the observation of the QD AlAs-like mode in the PLE spectrum taken at higher resolution. It is worth noting that there is no Stokes shift between PL and PLE lines at 1.662 eV, as expected from the absence of inhomogeneous broadening in the spectrum of a single dot. Consequently, the width of the PLE peaks seems to be intrinsic. Part of it can be due to different phonon contributions as the phonon of the wetting layer, which has been reported at 29.6 meV in InAs/GaAs QDs [222], or interface phonons [30]. Also inhomogeneity in the strain of the QD can contribute to the broadening. It is difficult to quantify the different contributions of the broadening, so that the true polaron decay time from the width of the PLE peaks cannot be estimated. PLE spectra of smaller dots emitting at higher energies are difficult to interpret due to the overlap with excited-state transitions in larger dots in the same spectral region. The energy loss in the QD occurs through the coupling of the phonon part of the polaron to optical or acoustical barrier phonons [204, 214, 221]. This coupling is favored in InAs/GaAs QDs by the fact that the QD phonon energy is very close to the GaAs LO bulk value. Energy can be then easily driven out of the dot via phonon-phonon interaction. In the present case, the energies of the optical phonons of the barrier (45-50 meV) are too high to couple to the QD polaron. This can result in an enhancement of the polaron lifetime in InAs/AlAs QDs. An alternative possible decay path of the polaron is the emission of two acoustic AlAs phonons TA(X,K), whose energy (15 meV) [228] is close to one half of the QD one. A marked peak in the density of states for acoustic phonons in AlAs at this energy [228] gives support to this mechanism. However, the coupling to acoustical phonons is comparatively weak, and it might not result in an efficient polaron decay. Time-resolved PL measurements on single QD with intra-dot excitation would be needed to decide on the polaron decay time of the system.

5.3 Piezoelectric exciton-acoustic phonon coupling

In this section the study of the exciton-phonon coupling in a single quantum dot is extended to acoustic phonons. Microphotoluminescence spectroscopy at variable temperature, excitation intensity and energy was performed on a single InAs/AlAs SAQD. The exciton emission line (zero-phonon line, ZPL) exhibits a broad sideband due to exciton-acoustic phonon coupling by the deformation potential mechanism. Additionally, narrow low-energy sidebands at about 0.25 meV from the ZPL are observed and attributed to exciton-acoustic phonon piezoelectric coupling. By lowering the excitation energy or intensity these bands gradually dominate the emission spectrum of the quantum dot while the ZPL disappears. At high excitation intensity the sidebands due to piezoelectric coupling decrease strongly and the ZPL dominates the spectrum as a consequence of screening of the piezoelectric coupling by the photocreated free carriers. [3]

5.3.1 Introduction

The knowledge of interactions of confined carriers with the environment is of fundamental importance for device operation because they determine both the optical efficiency and the coherence properties. Phase coherence can be lost either by relaxation processes, namely, radiative and phonon-assisted recombination, or by coupling to acoustic phonons (pure dephasing). The former produces a broadening of the Lorentzian zero-phonon line (see section 3.4 for a more detailed discussion). Coupling to acoustic phonons gives rise to non-Lorentzian sidebands [229], as discussed in the introduction of this chapter.

Temperature induced broadening of the ZPL associated to exciton-phonon scattering was reported for natural QDs in a GaAs QW [230] and CdSe/ZnCdSe QDs [231]. Acoustic phonon sidebands were observed in CdTe/ZnTe QDs [229, 232], InAs/GaAs QDs [233], GaAs monolayer fluctuation QDs [234], and CdSe QDs [100].

Exciton acoustic-phonon interactions in QD have been treated theoretically considering both the deformation potential (DP) and piezoelectric (PZ) coupling mechanisms [97, 199, 229]. It was pointed out theoretically [200] and experimentally [229]

[3] Part of these results were published in Phys. Rev. B 78, 241305(R) (2008) and AIP Conf. Proc. (submitted)

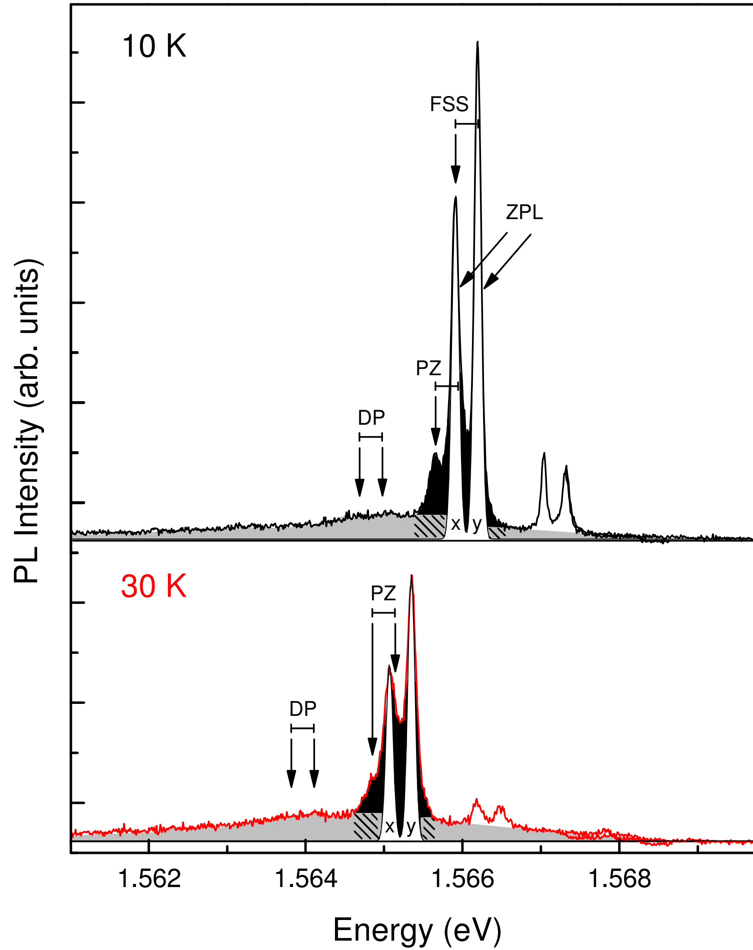

Figure 5.10: Photoluminescence spectra of a fine-structure split exciton doublet (x,y) of a single QD for temperatures of 10 and 30 K, excited at $E_{excit} = 2.41$ eV. Each component of the doublet is composed of a central Lorentzian zero-phonon line and asymmetric acoustic phonon wings.

that in small QDs the DP coupling mechanism dominates over PZ coupling. However, effects related to piezoelectricity in quantum dots are still under investigation, as they are very sensible to QD geometry, size and composition [183, 191, 235, 236].

In this section micro-PL spectra on a single InAs/AlAs QD for varying temperature, excitation power, and excitation energy are presented. Besides a broad acoustic phonon sideband, similar to previously reported ones originated by DP coupling [100, 229, 232–234] a narrow low-energy sideband (PZ sideband) is observed as a result of the PZ exciton coupling to long-wavelength acoustical phonons. This interpretation is supported by the strong reduction of the PZ sidebands observed

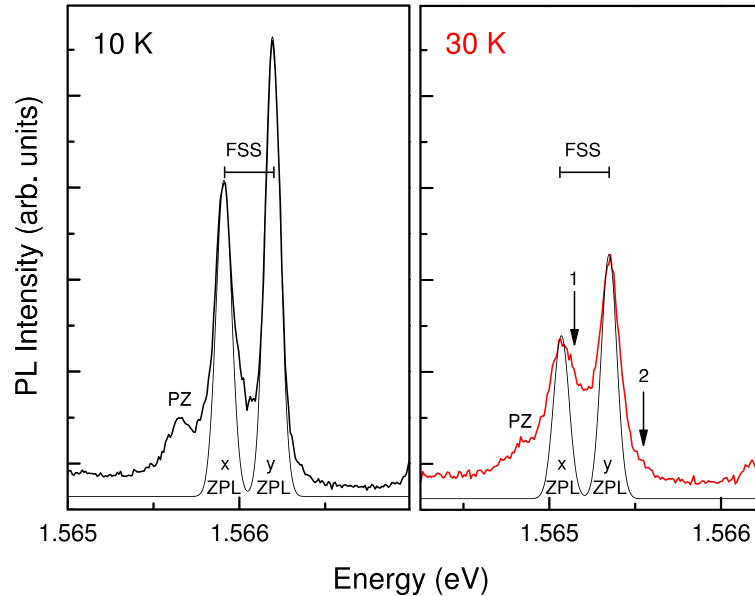

Figure 5.11: The narrow sidebands due to piezoelectric exciton-acoustic phonon coupling are shown. Left panel (10 K): The PZ sideband of the x-peak is observed at 0.25 meV below the zero-phonon line. The sideband corresponding to the y-ZPL results in an additional broadening of the x-peak. Right panel (30 K): By increasing the temperature sidebands also appear on the high energy sides of the y-ZPL (arrow 2) and x-ZPL (arrow 1, perceived as elevated x-y valley).

on increasing excitation power, as a consequence of screening by the photocreated carriers.

5.3.2 Results and Discussion

Figure 5.10 shows the PL spectra of the exciton transition of a single quantum dot for temperatures of 10 and 30 K. All peaks belong to the same QD, as shown by the spectral jitter and the polarization- and power dependence [79]. The exciton transition consists of a fine-structure split doublet of linearly cross-polarized peaks x and y. The weak peaks at higher energy belong to the same QD, as shown by jitter and resonant excitation experiments (see section 5.1. They could be the X+ and X- charged excitons, as they are not polarized. The fact that both are at higher energy than the neutral exciton recombination has been discussed in section 3.3. The large fine-structure splitting of 0.28 meV is due to the high AlAs barriers (see section 4.4). The peaks shift to lower energies with increasing temperature, due to

thermal expansion (see section 3.4). At 10 K broad acoustic phonon wings (light gray area) are observed. They are more pronounced at the low energy side [237] reflecting the higher probability of emitting than absorbing a phonon. With increasing temperature this asymmetry is gradually removed and the wing and ZPL broaden as reported for II-VI [100, 229, 232] and III-V [233, 234] semiconductor QDs. This wing corresponds to the widely reported *DP mediated* exciton-acoustic phonon interaction. Note, that the fine-structure splitting of the exciton transition is sufficiently large to resolve two separate maxima in the low energy wing at about 1.2 meV (DP arrows) corresponding to the most efficiently coupled acoustic phonon modes. This value is larger than the 0.7 meV estimated [4] for CdTe QD

The ratio between these values is 1.7. Assuming similar QD sizes, the value for this ratio can be estimated from the ratio of the corresponding sound velocities v_{LA}. For QD materials the ratio is 1.3 ($v_{LA,InAs} = 4.28 \times 10^5 cm/s, v_{LA,CdTe} = 3.34 \times 10^5 cm/s$ [111]), while for barrier materials the ratio is 1.6 ($v_{LA,AlAs} = 6.24 \times 10^5 cm/s, v_{LA,ZnTe} = 3.84 \times 10^5 cm/s$ [111])

Additional features (black areas) are observed close to the ZPL, which are the main focus of this section. They are shown in detail in Figure 5.11. At 10 K an additional narrow low-energy band located at 0.25 meV below the x-ZPL (marked PZ) is observed. A similar band can be perceived below the y-ZPL, although it is masked by the x-ZPL, giving rise to an apparent additional broadening of the x peak. By increasing the temperature (30K), a wing appears on the high energy side of the y-ZPL (arrow 2). The corresponding wing for the x-ZPL (arrow 1) results in an elevation of the x-y valley. Thus, concerning temperature dependence the low-energy sidebands behave similarly to the DP wings. These narrow low-energy sidebands are attributed to the interaction of the exciton with *long wavelength* acoustic phonons mediated by *PZ coupling*.

In order to support this assignment, excitation intensity dependent measurements were performed, shown in Figure 5.12. The spectra are normalized to the excitation power, which ranges from $P_0/160$ to P_0 ($P_0 = 0.4$ mW). Spectra are shifted vertically for clarity. The left and right panel show PL spectra for excitation below (1.98 eV) and above (2.14 eV) the wetting layer absorption edge, respectively. For decreasing excitation power the acoustic phonon wings become wider and more pronounced while

[4]The strongest coupling is found in reference [229] for a wave vector equal to the inverse of the dot size. For a QD of size of 9 nm, this gives 0.66 meV (Figure 3 of reference [229]).

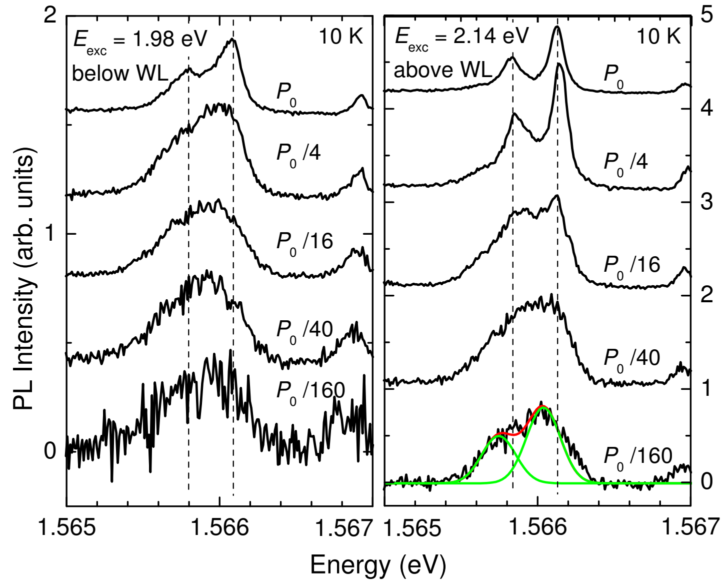

Figure 5.12: Photoluminescence spectra of the exciton doublet for a series of excitation power. Left and right panel show the spectra for excitation below and above the wetting layer absorption edge. For increasing excitation intensities the sidebands get less pronounced opposite to the zero-phonon lines, which gain weight. This indicates a screening effect of the acoustic-phonon-exciton coupling. Spectra are taken at 10 K.

the ZPLs lose weight compared to the sidebands. For the lowest intensities the ZPLs are not even observed any longer and the transition lineshape is completely dominated by the PZ sidebands. This power dependence of the sidebands and ZPLs is indicative of screening. In contrast to the DP coupling mechanism, PZ coupling can be screened out by free carriers [199, 200]. By increasing the excitation power, more electron-hole pairs are generated and the PZ mediated exciton acoustic-phonon interaction is more efficiently screened. When exciting above the wetting-layer absorption edge (right panel in Figure 5.12) the screening is more efficient than exciting below it (left panel). This observation supports the attribution to the PZ coupling mechanism revealed by the power dependence observed in Figure 5.12. Apart from the transition of a ZPL-dominated spectrum to a lineshape dominated by the PZ acoustic-phonon wings upon decreasing excitation power, a redshift can be observed: Both PL maxima in the spectrum taken at lowest excitation power are clearly red-shifted with respect to the corresponding ZPL maxima . For clarity two Gaussian peaks have been drawn

into the spectrum taken at the lowest excitation power, shown in Figure 5.12 This shift confirms that for lowest excitation power the ZPL disappeared and the PL arises from acoustic-phonon replicas. For a monochromatic (optical) phonon the shift would give the average number of phonons involved in the transition. Here, the continuous dispersion relation of acoustic phonons leads to a wing of overlapping replicas corresponding to phonons of different energies. Supposing, that one phonon processes dominate, the peak position gives the phonon mode, which is most efficiently coupled (via PZ coupling) to the exciton state.

The PZ sidebands are much closer ($E_{PZ} = 0.25$ meV) to the ZPL than the corresponding DP wings ($E_{DP} = 1.2$ meV). One possible explanation of that difference is the wave vector dependence of both coupling mechanisms: the electron-acoustic-phonon coupling mediated by DP interaction increases with the wave vector q as $\sqrt{q}$ while the unscreened PZ mediated coupling goes [199] as $1/\sqrt{q}$. This additional $1/q$ dependence of the PZ coupling results in an stronger interaction for small q (long-wavelength) acoustic phonons [238].

The presence of residual or photo-generated carriers changes the $1/\sqrt{q}$ dependence to $1/\sqrt{q} \times q^2/(q^2 + q_D^2)$,[199] which vanishes at zero wave vector. Therefore, screening gives rise to a sideband appearing as a peak next to the zero phonon line instead of a broad wing, as shown in Figure 5.11. The sidebands could be thought to be due to dark exciton states becoming allowed by QD asymmetry. Although bright-dark exciton splitting have been reported for similar energy differences as observed here, it is excluded that the sidebands are due to dark exciton transitions: Magneto-PL measurements carried out on the same QD are presented in section 3.8 and reveal that the sidebands of both ZPLs are at a constant energy difference for varying magnetic field up to 12 T. This would imply a vanishing hole g-factor in contrast to reported values around -2 for InGaAs/GaAs QDs having similar bright-dark splitting [149]. Besides, the lineshape evolution at low excitation power (Figure 5.12) cannot be explained by dark excitons, but is well described by piezoelectric coupling and screening.

From the energy maxima of the sidebands one can estimate the QD size and screening length. The energy of the DP sideband maxima is related to the QD size by $E_{DP} = \hbar v_{LA}/\xi$, ξ being the localization length [229, 239], since the most efficient exciton-phonon coupling is expected for a phonon wavelength similar to the extension of the exciton wavefunction.. This gives a rough estimate of around

10 nm for the here investigated QD, consistent with the atomic force microscopy measurements [67]. On the other hand, the energy position of the maximum of the PZ sideband allows to estimate the Debye screening length [5] $\lambda_D = 1/k_D = \hbar v_s/E_{PZ} \approx 10$ nm ($v_s = 2250$ m/s is the mixed LA/TA sound velocity [199]), which is of the order of the QD size.

This confirms that screening is relevant in the system studied here. Indeed one can estimate the density of mobile photocreated charges: $n_0 = \epsilon\epsilon_0 k_B T/e^2\lambda_D^2 \approx 10^{14}$ cm^{-3}, at temperature $T = 10$ K, static dielectric constant $\epsilon_r = 15$. k_B is the Boltzmann constant, and ϵ_0 is the vacuum dielectric constant and e the elementary charge.

Figure 5.13 exhibits the total apparent linewidth of the emission peak versus the excitation energy for constant intensity. A line narrowing effect is observed for increasing excitation energy. It appears more pronounced for the x exciton because it overlaps with the wing of the y peak. This is in contrast to experiments with InGaAs QDs [240] where line narrowing is observed for decreasing excitation energy and is interpreted in terms of electrostatic broadening: A reduced excess energy $E_{excit} - E_X$ leads to fewer charges in the vicinity of the QD resulting in a weaker spectral diffusion. Thus, jitter can be excluded as the origin of the exciton broadening in the present case. Line narrowing with increasing excitation energy was reported for InAlGaAs QDs[105], and tentatively attributed to increasingly efficient evaporation of excess carriers from the QD , but the origin of the effect is left open. In the present case, the line narrowing is attributed to a more efficient creation of free carriers at energies above the wetting layer, which shield the exciton PZ coupling to acoustic phonons. Therefore it can be concluded that charges photocreated in the wetting layer continuum are responsible for the screening.

The power and energy dependent exciton-acoustic phonon coupling as well as the the large fine-structure splitting (see section 4.4) manifest strong PZ effects in the here investigated dots compared to previously reported experiments. In general QDs present different strain distributions, which depend delicately on the QD geometry and give rise to PZ effects. Both linear [183, 235] and particularly quadratic piezoelectric effects [191, 236] are very sensitive to QD shape, size and composition, so that both components might even cancel out [241]. Regarding the composition, part of the strong effect can be attributed to the larger PZ coefficient $e_{14} = -0.23$ Cm^{-2} (bulk,

[5] The Debye screening length λ_D is the characteristic length up to which charges are relevant for interactions. Beyond this distance charges are screened.

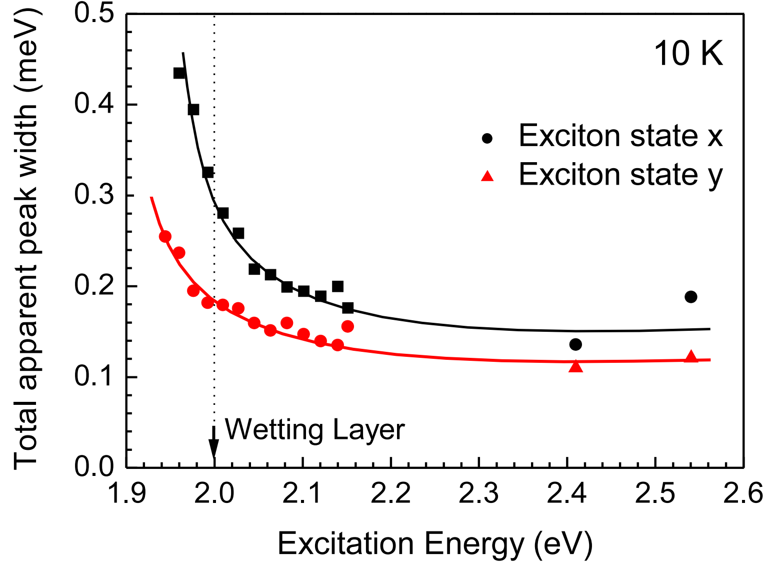

Figure 5.13: Total apparent linewidth of the exciton peaks versus excitation energy for constant excitation power. A transition to broader peaks can be observed for excitation below the wetting layer. Continuous lines are drawn as a guide for the eyes.

estimated) of AlAs compared to GaAs (-0.16) and InAs (-0.045) (bulk, experimental) [111]. For GaAs and InAs the calculated effect of strain increases [236] e_{14} to -0.230 (GaAs) and -0.115 (InAs). For strained AlAs also an even higher value might be expected. Additionally, intermixing [33, 242] of Al (see also section 5.1) will rise the PZ coefficient of the InAs QD. Referring to the QD geometry, it has been predicted that a high vertical aspect ratio [191], which allows a large vertical separation of the electron and hole charges, increases the PZ effects. The QD under investigation are the larger ones, emitting at the low energy tail of the QD ensemble. It was reported that for InAs/GaAs [73] and InAs/AlAs QDs [24] a large QD volume involves also a large vertical aspect ratio and consequently would lead to stronger PZ effect. Thus, both morphology and composition of the here investigated QDs definitely can lead to stronger PZ effects compared to InAs/GaAs ones.

5.4 Conclusions

In summary, the exciton-phonon interactions were studied by PL spectroscopy and resonant excitation of the PL emission in single InAs/AlAs QDs. Resonances corresponding to all the LO phonons of the QD system were found (InAs-like and AlAs-like of the QD, and AlAs-LO of the barrier). In particular the 41.3 meV resonance is associated to the AlAs-like LO phonon of InAlAs with small Al concentration. This constitutes a direct optical determination of the intermixing in a single QD. All of the observed phonons couple to the QD electronic transitions and can thus contribute to carrier relaxation.

Furthermore, The PLE spectra of single QDs under intra-dot excitation presents strong peaks at multiples of 31 meV, which are interpreted as the result of the polaronic coupling of the electronic states in the dot to the QD phonon.

Finally, it is shown that piezoelectric effects play an important role in InAs/AlAs QDs. Particularly, a considerable contribution to the exciton-long wavelength acoustic-phonon interaction is mediated by PZ coupling. The interaction can be screened by photo-created carriers, and this switching ability might be used in future quantum devices.

Chapter 6

Conclusions

In the present thesis a study of individual self-assembled InAs/AlAs quantum dots by means of optical spectroscopy has been presented. Experimental techniques newly developed and implemented for this study in the continuous-wave spectroscopy laboratory at the UAM are described. Basic properties of InAs/AlAs QDs have been investigated and compared with the widely studied InAs/GaAs QDs. Furthermore, systematic dependencies of the electronic properties have been found, and the interactions of the confined exciton with optical and acoustic phonons have been studied. The main results are summarized in the following points.

Experimental developments:

- A high spatial resolution micro-photoluminescence microscope setup has been constructed, allowing the spectroscopy of single quantum dots. For photoluminescence excitation measurements the fore-monochromator was automatized by building an electronic interface and several computer programs/scripts have been developed for automatic data acquisition.

- In order to reduce the probed number of dots, opaque metal masks with small square openings of lateral sizes of 10 down to 0.2 μm were fabricated on top of the sample, in collaboration with Prof. R.J. Haug and J.M. Meyer (Leibniz University of Hannover) by electron beam lithography and lift-off.

Basic properties of the InAs/AlAs QD:

- Micro-PL measurements on small ensembles of QD reveal sharp emission lines below 1.8 eV, and continuous emission at higher energies. The indirect character of the band gap of the matrix leads to a quantum-confinement driven direct-indirect transition in real (type I - type II transition) and reciprocal space (Γ-X transition) for decreasing QD size. For small QDs the ground exciton state is pushed above the AlAs X-band allowing the electron to scatter into the dispersive barrier states.

- A series of preliminar/fundamental micro-photoluminescence experiments were carried out in order to get a first insight into the properties of single InAs/AlAs QDs. Time series of photoluminescence spectra reveal spectral diffusion of the emission peaks and allow the assignment of emission lines to individual dots. Polarization resolved spectra show linearly counter-polarized doublets for the exciton and biexciton emission. Excitation power dependent spectra are taken to distinguish exciton and biexciton emission by their power dependencies.

- Photoluminescence spectra for varying temperatures show the usual red-shift of the exciton emission for increasing temperature, corresponding to the temperature dependence of the bulk InAs band gap. A yet typical, but fairly large zero-phonon linewidth broadening of 1.5 μeV/K is observed and tentatively attributed to the small distance between the dot and the sample surface. Acoustic phonon wings are identified and were further studied in detail (see below).

- Magneto-photoluminescence measurements reveal an extremely small diamagnetic shift of 1.4 μeV/T^2 due to strong exciton localization. The Zeeman splitting reveals an exciton g-factor of about 1.7 being in the range of commonly observed values. Circular polarization of the exciton emission is restored at moderate fields above 4 T, indicating a symmetrization of the electron and hole wavefunctions.

Electronic properties:

- Very large biexciton binding energies up to 9 meV were found and attributed to increased correlation effects due to the large AlAs barriers. The biexciton

binding energy is sensitive to the quantum dot size, since its magnitude decreases for increasing exciton emission energy. Further, the biexciton becomes anti-bound for exciton emission energies above 1.63 meV. The trend is similar to those reported for InAs/GaAs QDs and likewise attributed to an interplay of direct Coulomb contributions and a dominant impact of correlation terms. For small dots with less bound states the correlation term decreases and repulsive Coulomb contributions dominate.

- Large fine-structure splittings of the bright exciton state up to 0.3 meV were observed. They are larger than splittings for the commonly investigated InAs/GaAs QDs. This difference is attributed to large piezoelectric effects, due to the larger piezoelectric constant of AlAs compared to GaAs and the QD morphology. Both large vertical aspect ratio and reduced indium-aluminum intermixing (what in turn implies large shear strains) lead to enhanced piezoelectric effects.

- Both the biexciton binding energy and fine-structure splitting vanish nearly at the same exciton emission energy suggesting a common origin. This is tentatively attributed to a simultaneous reduction of correlation and exchange terms for decreasing QD size.

Exciton-Phonon interactions:

- The photoluminescence excitation spectra of a single QD exhibit broad resonances at multiples of about 31 meV and are attributed to polaron formation involving the QD InAs longitudinal-optical phonon. This is in contrast to InAs/GaAs QDs, where typically polaron formation with the GaAs LO barrier phonon is observed. This result evidences the poorer exciton coupling to the barrier phonon due to the stronger exciton localization in the InAs QDs and the harder AlAs barrier material.

- Multiple resonances are observed in the high-resolution photoluminescence excitation spectrum of a single QD and reveal that the QD exciton couples to all longitudinal-optical phonons of the dot-barrier system. In particular, a resonance at 41.3 meV is associated to the AlAs-like QD phonon. This constitutes a direct optical detection of the incorporation of aluminum into a single QD, which is estimated to be below 10 %.

- Exciton-acoustic phonon interactions are investigated for varying temperature, excitation intensity and excitation energy. Very broad acoustic phonon wings are observed and attributed to deformation potential coupling. The large fine-structure splitting of the bright exciton states allows the identification of a wing for each of the two zero-phonon lines. Apart from this commonly observed broad wings, narrow, low energy sidebands are observed and attributed to piezoelectric exciton-acoustic phonon coupling. Excitation power and energy dependent photoluminescence spectra support this attribution by the observation of a screening effect. Photocreated free carriers in the wetting layer, are able to screen the piezoelectric interaction. A characteristic screening length of about 10 nm is estimated, being in the order of magnitude of the QD size. This demonstrates the relevance of screening in the system.

Bibliography

[1] Bayer, M. *Nature* **418**(6898), 597–598 (2002).

[2] Chen, G., Bonadeo, N. H., Steel, D. G., Gammon, D., Katzer, D. S., Park, D., and Sham, L. J. *Science* **289**(5486), 1906–1909 September (2000).

[3] Michler, P., Kiraz, A., Becher, C., Schoenfeld, W. V., Petroff, P. M., Zhang, L., Hu, E., and Imamoglu, A. *Science* **290**(5500), 2282–2285 December (2000).

[4] Santori, C., Pelton, M., Solomon, G., Dale, Y., and Yamamoto, Y. *Phys. Rev. Lett.* **86**(8), 1502 February (2001).

[5] Santori, C., Fattal, D., Vuckovic, J., Solomon, G. S., and Yamamoto, Y. *Nature* **419**(6907), 594–597 October (2002).

[6] Benson, O., Santori, C., Pelton, M., and Yamamoto, Y. *Phys. Rev. Lett.* **84**, 2513 March (2000).

[7] Stevenson, R. M., Young, R. J., Atkinson, P., Cooper, K., Ritchie, D. A., and Shields, A. J. *Nature* **439**, 179–182 (2006).

[8] Akopian, N., Lindner, N. H., Poem, E., Berlatzky, Y., Avron, J., Gershoni, D., Gerardot, B. D., and Petroff, P. M. *Phys. Rev. Lett.* **96**(13), 130501–4 April (2006).

[9] Fiore, A., Chen, J. X., and Ilegems, M. *Appl. Phys. Lett.* **81**(10), 1756–1758 (2002).

[10] Liu, H., Gao, M., McCaffrey, J., Wasilewski, Z., and Fafard, S. *Appl. Phys. Lett.* **78**(1), 79–81 (2001).

[11] Chakrabarti, S., Stiff-Roberts, A. D., Su, X. H., Bhattacharya, P., Ariyawansa, G., and Perera, A. G. U. *Journal of Physics D: Applied Physics* **38**(13), 2135 (2005).

[12] Bimberg, D. *J. Phys. D: Appl. Phys.* **38**, 2055 (2005). qd-appl qd-laser.

[13] Akiyama, T., Hatori, N., Nakata, Y., Ebe, H., and Sugawara, M. *Electronics Letters* **38**, 1139–1140 (2002).

[14] Imamura, K., Sugiyama, Y., Nakata, Y., Muto, S., and Yokoyama, N. *Japanese Journal of Applied Physics, Part 2 (Letters)* **34**, L1445–7 November (1995).

[15] Gao, X., Cui, Y., Levenson, R. M., Chung, L. W. K., and Nie, S. *Nat Biotech* **22**(8), 969–976 (2004).

[16] Fafard, S., Leon, R., Leonard, D., Merz, J. L., and Petroff, P. M. *Phys. Rev. B* **50**, 8086 (1994).

[17] Finley, J. J., Mowbray, D. J., Skolnick, M. S., Ashmore, A. D., Baker, C., Monte, A. F. G., and Hopkinson, M. *Phys. Rev. B* **66**, 153316 October (2002).

[18] Shamirzaev. *Phys. Status Solidi C* **5**, 2528 (2008).

[19] Shamirzaev, T. S., Nenashev, A. V., Gutakovskii, A. K., Kalagin, A. K., Zhuravlev, K. S., Larsson, M., and Holtz, P. O. *Phys. Rev. B* **78**, 085323–10 (2008).

[20] Leon, R., Fafard, S., Leonard, D., Merz, J. L., and Petroff, P. M. *Appl. Phys. Lett.* **67**, 521–523 July (1995).

[21] Arzberger, M., Kasberger, U., Bohm, G., and Abstreiter, G. *Appl. Phys. Lett.* **75**, 3968–3970 December (1999).

[22] Polimeni, A., Patan, A., Henini, M., Eaves, L., and Main, P. C. *Phys. Rev. B* **59**, 5064 February (1999).

[23] Lee, U. H., Lee, D., Lee, H. G., Noh, S. K., Leem, J. Y., and Lee, H. J. *Appl. Phys. Lett.* **74**, 1597–1599 March (1999).

[24] Ballet, P., Smathers, J., and Salamo, G. *Appl. Phys. Lett.* **75**, 337–339 July (1999).

[25] Ma, Z., Pierz, K., and Hinze, P. *Appl. Phys. Lett.* **79**, 2564–2566 October (2001).

[26] Ma, Z. and Pierz, K. *Surface Science* **511**, 57–64 June (2002).

[27] Pierz, K., Ma, Z., Hapke-Wurst, I., Keyser, U. F., Zeitler, U., and Haug, R. J. *Physica E* **13**, 761–764 March (2002).

[28] Ma, Z., Pierz, K., Keyser, U., and Haug, R. *Physica E* **17**, 117–119 April (2003).

[29] Pierz, K., Ma, Z., Keyser, U. F., and Haug, R. J. *Journal of Crystal Growth* **249**, 477–482 March (2003).

[30] Milekhin, A. G., Toropov, A. I., Bakarov, A. K., Tenne, D. A., Zanelatto, G., Galzerani, J. C., Schulze, S., and Zahn, D. R. T. *Phys. Rev. B* **70**, 085314 (2004).

[31] Ladanov, M., Milekhin, A., Toropov, A., Bakarov, A., Gutakovskii, A., Tenne, D., Schulze, S., and Zahn, D. *Journal of Experimental and Theoretical Physics* **101**, 554–561 (2005).

[32] Milekhin, A., Toropov, A., Bakarov, A., Schulze, S., and Zahn, D. *physica status solidi (c)* **3**, 3924–3927 (2006).

[33] Offermans, P., Koenraad, P. M., Wolter, J. H., Pierz, K., Roy, M., and Maksym, P. A. *Phys. Rev. B* **72**, 165332–6 October (2005).

[34] Dawson, P., Ma, Z., Pierz, K., and Gobel, E. O. *Appl. Phys. Lett.* **81**, 2349–2351 (2002).

[35] Shamirzaev, T. S., Nenashev, A. V., and Zhuravlev, K. S. *Appl. Phys. Lett.* **92**, 213101–3 May (2008).

[36] Dawson, P., Gobel, E. O., and Pierz, K. *Journal of Applied Physics* **98**(1), 013541–6 July (2005).

[37] Milekhin, A., Toropov, A., Bakarov, A., Schulze, S., and Zahn, D. *JETP Letters* **83**, 505–508–599 (2006).

[38] Farfad, S., Leon, R., Leonard, D., Merz, J. L., and Petroff, P. M. *Phys. Rev. B* **52**, 5752 (1995).

[39] Pierz, K., Miglo, A., Hinze, P., Ahlers, F., Ade, G., Hapke-Wurst, I., Zeitler, U., and Haug, R. *physica status solidi (b)* **224**, 119–122 (2001).

[40] Xie, Q., Chen, P., Kalburge, A., Ramachandran, T. R., Nayfonov, A., Konkar, A., and Madhukar, A. *Journal of Crystal Growth* **150**, 357–363 May (1995).

[41] Goldstein, L., Glas, F., Marzin, J. Y., Charasse, M. N., and Roux, G. L. *Appl. Phys. Lett.* **47**, 1099–1101 November (1985).

[42] Nishi, K., Mirin, R., Leonard, D., Medeiros-Ribeiro, G., Petroff, P., and Gossard, A. In *Indium Phosphide and Related Materials, 1995. Conference Proceedings., Seventh International Conference on*, 759–762, (1995).

[43] Heitz, R., Guffarth, F., Potschke, K., Schliwa, A., Bimberg, D., Zakharov, N. D., and Werner, P. *Phys. Rev. B* **71**(4), 045325 (2005).

[44] Marzin, J. Y., Gerard, J. M., Izrael, A., Barrier, D., and Bastard, G. *Phys. Rev. Lett.* **73**, 716 (1994).

[45] Zrenner, A., Butov, L. V., Hagn, M., Abstreiter, G., Bohm, G., and Weimann, G. *Phys. Rev. Lett.* **72**, 3382 May (1994).

[46] Brunner, K., Abstreiter, G., Bohm, G., Trankle, G., and Weimann, G. *Phys. Rev. Lett.* **73**, 1138 (1994).

[47] Hess, H. F., Betzig, E., Harris, T. D., Pfeiffer, L. N., and West, K. W. *Science* **264**, 1740–1745 June (1994).

[48] Leon, R., Petroff, P. M., Leonard, D., and Fafard, S. *Science* **267**, 1966–1968 March (1995).

[49] Lazic, S. *Optical spectroscopy of nitride semiconductor structures.* PhD thesis, (2008).

[50] Delhaye, M. and da Silva, E. *Confocal laser Raman.* Dilor, Manual.

[51] *Application notes AN470: The L297 stepper motor controller; L298 DUAL FULL-BRIDGE DRIVER.* SGS-Thomson Microelectronics.

[52] Temkin, H., Dolan, G., Panish, M., and Chu, S. *Appl. Phys. Lett.* **50**(7), 413–415 February (1987).

[53] Martin-Sanchez, J., Gonzalez, Y., Gonzalez, L., Tello, M., Garca, R., Granados, D., Garcia, J., and Briones, F. *Journal of Crystal Growth* **284**(3-4), 313–318 November (2005).

[54] Alonso-Gonzalez, P., Martn-Gonzalez, M., Martin-Sanchez, J., Gonzalez, Y., and Gonzalez, L. *Journal of Crystal Growth* **294**(2), 168–173 September (2006).

[55] Baier, M. H., Watanabe, S., Pelucchi, E., and Kapon, E. *Appl. Phys. Lett.* **84**(11), 1943–1945 March (2004).

[56] Tulkki, J. and Heinamaki, A. *Phys. Rev. B* **52**, 8239 (1995).

[57] Lipsanen, H., Sopanen, M., and Ahopelto, J. *Phys. Rev. B* **51**, 13868 May (1995).

[58] Sopanen, M., Lipsanen, H., and Ahopelto, J. *Appl. Phys. Lett.* **66**, 2364–2366 May (1995).

[59] Gammon, D., Snow, E. S., Shanabrook, B. V., Katzer, D. S., and Park, D. *Phys. Rev. Lett.* **76**, 3005 April (1996).

[60] Brunner, K., Bockelmann, U., Abstreiter, G., Walther, M., Bohm, G., Trankle, G., and Weimann, G. *Phys. Rev. Lett.* **69**(22), 3216 November (1992).

[61] Bacher, G., Kummell, T., Eisert, D., Forchel, A., Konig, B., Ossau, W., Becker, C. R., and Landwehr, G. *Appl. Phys. Lett.* **75**(7), 956–958 (1999).

[62] Schedelbeck, G., Wegscheider, W., Bichler, M., and Abstreiter, G. *Science* **278**(5344), 1792–1795 December (1997).

[63] Gindele, F., Westphaling, R., Woggon, U., Spanhel, L., and Ptatschek, V. *Appl. Phys. Lett.* **71**(15), 2181–2183 October (1997).

[64] Madelung, O. *Semiconductors: Data Handbook*. Springer, 3rd ed. edition, (2004).

[65] Eaglesham, D. J. and Cerullo, M. *Phys. Rev. Lett.* **64**(16), 1943 April (1990).

[66] Guha, S., Madhukar, A., and Rajkumar, K. *Appl. Phys. Lett.* **57**, 2110–2112 November (1990).

[67] Ma, Z., Pierz, K., Ahlers, F. J., Keyser, U. F., and Haug, R. J. (2002).

[68] Hatami, F., Ledentsov, N., Grundmann, M., Bohrer, J., Heinrichsdorff, F., Beer, M., Bimberg, E., Ruvimov, S., Werner, P., Gosele, U., Heydenreich, J., Richter, U., Ivanov, S., Meltser, B., Kop'ev, P., and Alferov, Z. *Appl. Phys. Lett.* **67**, 656–658 July (1995).

[69] Bennett, B., Magno, R., and Shanabrook, B. *Appl. Phys. Lett.* **68**, 505–507 (1996).

[70] Glaser, E., Bennett, B., Shanabrook, B., and Magno, R. *Appl. Phys. Lett.* **68**, 3614–3616 June (1996).

[71] Robach, R., Schulz, W., Jetter, M., and Michler, P. *Journal of Crystal Growth* **298**, 599–602 (2007).

[72] Leonard, D., Krishnamurthy, M., Fafard, S., Merz, J., and Petroff, P. *Journal of Vacuum Science & Technology B (Microelectronics and Nanometer Structures)* **12**, 1063–1066 March (1994).

[73] Saito, H., Nishi, K., and Sugou, S. *Appl. Phys. Lett.* **74**, 1224 March (1999).

[74] Bayer, M. and Forchel, A. *Phys. Rev. B* **65**, 041308 (2002).

[75] Ortner, G., Yakovlev, D. R., Bayer, M., Rudin, S., Reinecke, T. L., Fafard, S., Wasilewski, Z., and Forchel, A. *Phys. Rev. B* **70**, 201301–4 November (2004).

[76] Hapke-Wurst, I., Zeitler, U., Keyser, U. F., Haug, R. J., Pierz, K., and Ma, Z. *Appl. Phys. Lett.* **82**, 1209–1211 February (2003).

[77] Shamirzaev, T. S., Gilinsky, A. M., Toropov, A. I., Bakarov, A. K., Tenne, D. A., Zhuravlev, K. S., von Borczyskowski, C., and Zahn, D. R. T. *Physica E* **20**, 282–285 (2004).

[78] Milekhin, A. G., Toropov, A. I., Bakarov, A. K., Ladanov, M. Y., Zanelatto, G., Galzerani, J. C., Schulze, S., and Zahn, D. R. T. *Applied Surface Science* **234**(1-4), 45–49 July (2004).

[79] Turck, V., Rodt, S., Stier, O., Heitz, R., Engelhardt, R., Pohl, U. W., Bimberg, D., and Steingraber, R. *Phys. Rev. B* **61**, 9944 April (2000).

[80] Joyce, P. B., Krzyzewski, T. J., Bell, G. R., Joyce, B. A., and Jones, T. S. *Phys. Rev. B* **58**(24), R15981 December (1998).

[81] Liu, N., Tersoff, J., Baklenov, O., Holmes, A. L., and Shih, C. K. *Phys. Rev. Lett.* **84**(2), 334 (2000).

[82] Wakefield, B., Halliwell, M., Kerr, T., Andrews, D., Davies, G., and Wood, D. *Appl. Phys. Lett.* **44**(3), 341–343 February (1984).

[83] Chen, Y., Li, G., Zhu, Z., Han, H., Wang, Z., Zhou, W., and Wang, Z. *Appl. Phys. Lett.* **76**, 3188–3190 May (2000).

[84] Luo, J.-W., Franceschetti, A., and Zunger, A. *Phys. Rev. B* **78**, 035306–8 July (2008).

[85] Diaz, J. G. and Bryant, G. W. *Phys. Rev. B* **73**, 075329–9 February (2006).

[86] Franceschetti, A. and Zunger, A. *Appl. Phys. Lett.* **68**, 3455–3457 June (1996).

[87] Christensen, N. E. *Phys. Rev. B* **30**, 5753 November (1984).

[88] Williamson, A., Franceschetti, A., Fu, H., Wang, L., and Zunger, A. *Journal of Electronic Materials* **28**, 414–425 May (1999).

[89] Wei, S.-H. and Zunger, A. *Appl. Phys. Lett.* **72**, 2011–2013 April (1998).

[90] Yoon, H. W., Wake, D. R., and Wolfe, J. P. *Phys. Rev. B* **54**(4), 2763 July (1996).

[91] Moskalenko, E. S., Karlsson, K. F., Holtz, P. O., Monemar, B., Schoenfeld, W. V., Garcia, J. M., and Petroff, P. M. *Phys. Rev. B* **64**, 085302 July (2001).

[92] Narvaez, G. A., Bester, G., and Zunger, A. *Phys. Rev. B* **72**, 245318–10 December (2005).

[93] Borri, P. and Langbein, W. *J. Phys.: Condens. Matter* **19**, 295201 (2007).

[94] Berthelot, A., Favero, I., Cassabois, G., Voisin, C., Delalande, C., Roussignol, P., Ferreira, R., and Gerard, J. M. *Nat Phys* **2**, 759–764 November (2006).

[95] Favero, I., Berthelot, A., Cassabois, G., Voisin, C., Delalande, C., Roussignol, P., Ferreira, R., and Gerard, J. M. *Physical Review B (Condensed Matter and Materials Physics)* **75**(7), 073308–4 February (2007).

[96] Kamada, H. and Kutsuwa, T. *Phys. Rev. B* **78**, 155324–16 October (2008).

[97] Vasilevskiy, M. I., Anda, E. V., and Makler, S. S. *Phys. Rev. B* **70**(3), 035318 July (2004).

[98] Gindele, F., Hild, K., Langbein, W., and Woggon, U. *Phys. Rev. B* **60**, R2157 July (1999).

[99] Gindele, F., Hild, K., Langbein, W., and Woggon, U. *Journal of Luminescence* **87-89**, 381–383 May (2000).

[100] Arians, R., Kummell, T., Bacher, G., Gust, A., Kruse, C., and Hommel, D. *Appl. Phys. Lett.* **90**, 101114–3 March (2007).

[101] Urbaszek, B., McGhee, E. J., Kruger, M., Warburton, R. J., Karrai, K., Amand, T., Gerardot, B. D., Petroff, P. M., and Garcia, J. M. *Physical Review B (Condensed Matter and Materials Physics)* **69**(3), 035304–6 (2004).

[102] Bayer, M., Ortner, G., Stern, O., Kuther, A., Gorbunov, A. A., Forchel, A., Hawrylak, P., Fafard, S., Hinzer, K., Reinecke, T. L., Walck, S. N., Reithmaier, J. P., Klopf, F., and Schafer, F. *Phys. Rev. B* **65**, 195315 May (2002).

[103] Kammerer, C., Voisin, C., Cassabois, G., Delalande, C., Roussignol, P., Klopf, F., Reithmaier, J. P., Forchel, A., and Gerard, J. M. *Phys. Rev. B* **66**, 041306 July (2002).

[104] Kammerer, C., Cassabois, G., Voisin, C., Perrin, M., Delalande, C., Roussignol, P., and Gerard, J. *Appl. Phys. Lett.* **81**, 2737–2739 October (2002).

[105] Leosson, K., Birkedal, D., Magnusdottir, I., Langbein, W., and Hvam, J. *Physica E* **17**, 1–6 April (2003).

[106] Sanguinetti, S., Poliani, E., Bonfanti, M., Guzzi, M., Grilli, E., Gurioli, M., and Koguchi, N. *Physical Review B (Condensed Matter and Materials Physics)* **73**(12), 125342–7 March (2006).

[107] Borri, P., Langbein, W., Woggon, U., Stavarache, V., Reuter, D., and Wieck, A. D. *Phys. Rev. B* **71**(11), 115328 March (2005).

[108] Passler, R. *Phys. Rev. B* **66**(8), 085201 (2002).

[109] Grundmann, M. *The physics of semiconductors an introduction including devices and nanophysics ; with tables.* Springer, Berlin [u.a., (2006).

[110] Madelung, O., Schulz, M., and Weiss, H. June (1983).

[111] Adachi, S. *Properties of Group-IV, III-V and II-VI Semiconductors.* John Wiley and Sons, (2005).

[112] Olkhovets, A., Hsu, R., Lipovskii, A., and Wise, F. W. *Phys. Rev. Lett.* **81**(16), 3539 October (1998).

[113] Leon, R., Kim, Y., Jagadish, C., Gal, M., Zou, J., and Cockayne, D. J. H. *Appl. Phys. Lett.* **69**(13), 1888–1890 (1996).

[114] Gammon, D., Snow, E. S., and Katzer, D. S. *Appl. Phys. Lett.* **67**, 2391–2393 October (1995).

[115] Empedocles, S. A., Norris, D. J., and Bawendi, M. G. *Phys. Rev. Lett.* **77**, 3873 October (1996).

[116] Robinson, H. D. and Goldberg, B. B. *Phys. Rev. B* **61**, R5086 February (2000).

[117] Seufert, J., Weigand, R., Bacher, G., Kummell, T., Forchel, A., Leonardi, K., and Hommel, D. *Appl. Phys. Lett.* **76**(14), 1872–1874 April (2000).

[118] Besombes, L., Kheng, K., Marsal, L., and Mariette, H. *Phys. Rev. B* **65**, 121314 March (2002).

[119] Bardoux, R., Guillet, T., Lefebvre, P., Taliercio, T., Bretagnon, T., Rousset, S., Gil, B., and Semond, F. *Physical Review B (Condensed Matter and Materials Physics)* **74**(19), 195319–6 November (2006).

[120] Trck, V., Rodt, S., Heitz, R., Stier, O., Straburg, M., Pohl, U. W., and Bimberg, D. *Physica E: Low-dimensional Systems and Nanostructures* **13**(2-4), 269–272 March (2002).

[121] Nirmal, M., Dabbousi, B. O., Bawendi, M. G., Macklin, J. J., Trautman, J. K., Harris, T. D., and Brus, L. E. *Nature* **383**, 802–804 October (1996).

[122] Pistol, M.-E., Castrillo, P., Hessman, D., Prieto, J. A., and Samuelson, L. *Phys. Rev. B* **59**, 10725 April (1999).

[123] Sugisaki, M., Ren, H., Nishi, K., and Masumoto, Y. *Phys. Rev. Lett.* **86**(21), 4883 May (2001).

[124] Ambrose, W. P. and Moerner, W. E. *Nature* **349**, 225–227 (1991).

[125] Efros, A. L. and Rosen, M. *Phys. Rev. Lett.* **78**, 1110 February (1997).

[126] Blome, P. G., Wenderoth, M., Hubner, M., Ulbrich, R. G., Porsche, J., and Scholz, F. *Phys. Rev. B* **61**, 8382 March (2000).

[127] Obermuller, C., Deisenrieder, A., Abstreiter, G., Karrai, K., Grosse, S., Manus, S., Feldmann, J., Lipsanen, H., Sopanen, M., and Ahopelto, J. *Appl. Phys. Lett.* **74**, 3200–3202 May (1999).

[128] Empedocles, S. A. and Bawendi, M. G. *Science* **278**, 2114–2117 December (1997).

[129] Ballet, P., Smathers, J. B., Yang, H., Workman, C. L., and Salamo, G. J. *J. Appl. Phys.* **90**, 481–487 July (2001).

[130] Patton, B., Langbein, W., and Woggon, U. *Phys. Rev. B* **68**(12), 125316 (2003).

[131] Bacher, G., Weigand, R., Seufert, J., Kulakovskii, V., Gippius, N., Forchel, A., Leonardi, K., and Hommel, D. *Phys. Rev. Lett.* **83**, 4417–4420 November (1999).

[132] Miller, R. C., Kleinman, D. A., Gossard, A. C., and Munteanu, O. *Phys. Rev. B* **25**(10), 6545 May (1982).

[133] pt Hooft, G. W., van der Poel, W. A. J. A., Molenkamp, L. W., and Foxon, C. T. *Phys. Rev. B* **35**(15), 8281 May (1987).

[134] Puls, J., Rossin, V. V., Kreller, F., Wunsche, H. J., Renisch, S., Hoffmann, N., Rabe, M., and Henneberger, F. *Journal of Crystal Growth* **159**, 784–787 February (1996).

[135] Finley, J. J., Fry, P. W., Ashmore, A. D., Lemaitre, A., Tartakovskii, A. I., Oulton, R., Mowbray, D. J., Skolnick, M. S., Hopkinson, M., Buckle, P. D., and Maksym, P. A. *Phys. Rev. B* **63**, 161305 April (2001).

[136] Dekel, E., Gershoni, D., Ehrenfreund, E., Spektor, D., Garcia, J. M., and Petroff, P. M. *Phys. Rev. Lett.* **80**, 4991 June (1998).

[137] Kaiser, S., Mensing, T., Worschech, L., Klopf, F., Reithmaier, J. P., and Forchel, A. *Appl. Phys. Lett.* **81**(26), 4898–4900 December (2002).

[138] Wu, Q., Grober, R. D., Gammon, D., and Katzer, D. S. *Phys. Rev. B* **2**, 13022 November (2000).

[139] Lowisch, M., Rabe, M., Kreller, F., and Henneberger, F. *Appl. Phys. Lett.* **74**, 2489–2491 April (1999).

[140] Alloing, B., Zinoni, C., Zwiller, V., Li, L. H., Monat, C., Gobet, M., Buchs, G., Fiore, A., Pelucchi, E., and Kapon, E. *Appl. Phys. Lett.* **86**(10), 101908–3 March (2005).

[141] Kuther, A., Bayer, M., Forchel, A., Gorbunov, A., Timofeev, V. B., Schafer, F., and Reithmaier, J. P. *Phys. Rev. B* **58**, R7508 (1998).

[142] Kamada, H., Ando, H., Temmyo, J., and Tamamura, T. *Phys. Rev. B* **58**, 16243 December (1998).

[143] Nakayama, M., Suyama, K., and Nishimura, H. *Phys. Rev. B* **51**(12), 7870 March (1995).

[144] Rodt, S., Heitz, R., Schliwa, A., Sellin, R. L., Guffarth, F., and Bimberg, D. *Phys. Rev. B* **68**, 035331 July (2003).

[145] Kulakovskii, V. D., Bacher, G., Weigand, R., Kummell, T., Forchel, A., Borovitskaya, E., Leonardi, K., and Hommel, D. *Phys. Rev. Lett.* **82**, 1780 February (1999).

[146] Young, R. J., Stevenson, R. M., Shields, A. J., Atkinson, P., Cooper, K., Ritchie, D. A., Groom, K. M., Tartakovskii, A. I., and Skolnick, M. S. *Phys. Rev. B* **72**, 113305–4 (2005).

[147] He, L., Bester, G., and Zunger, A. *Phys. Rev. B* **70**(23), 235316 December (2004).

[148] Harrison, P. *Quantum wells, wires, and dots : theoretical and computational physics of semiconductor nanostructures.* Wiley, Hoboken, NJ, (2005).

[149] Bayer, M., Kuther, A., Forchel, A., Gorbunov, A., Timofeev, V. B., Schafer, F., Reithmaier, J. P., Reinecke, T. L., and Walck, S. N. *Phys. Rev. Lett.* **82**, 1748 February (1999).

[150] van Kesteren, H. W., Cosman, E. C., van der Poel, W. A. J. A., and Foxon, C. T. *Phys. Rev. B* **41**(8), 5283 March (1990).

[151] Blackwood, E., Snelling, M. J., Harley, R. T., Andrews, S. R., and Foxon, C. T. B. *Phys. Rev. B* **50**, 14246 November (1994).

[152] Gammon, D., Snow, E. S., Shanabrook, B. V., Katzer, D. S., and Park, D. *Science* **273**, 87–90 July (1996).

[153] Ivchenko, E. L. *physica status solidi (a)* **164**, 487–492 (1997).

[154] Cade, N. I., Gotoh, H., Kamada, H., Nakano, H., and Okamoto, H. *Physical Review B (Condensed Matter and Materials Physics)* **73**(11), 115322–7 March (2006).

[155] Flissikowski, T., Hundt, A., Lowisch, M., Rabe, M., and Henneberger, F. *Phys. Rev. Lett.* **86**, 3172 April (2001).

[156] Puls, J., Rabe, M., Wunsche, H.-J., and Henneberger, F. *Phys. Rev. B* **60**, R16303 December (1999).

[157] Besombes, L., Kheng, K., and Martrou, D. *Phys. Rev. Lett.* **85**, 425 July (2000).

[158] Bayer, M., Stern, O., Kuther, A., and Forchel, A. *Phys. Rev. B* **61**, 7273 March (2000).

[159] Landin, L., Pistol, M.-E., Pryor, C., Persson, M., Samuelson, L., and Miller, M. *Phys. Rev. B* **60**, 16640 December (1999).

[160] Reischle, M., Beirne, G. J., Rossbach, R., Jetter, M., and Michler, P. *Phys. Rev. Lett.* **101**, 146402–4 October (2008).

[161] Nirmal, M., Norris, D. J., Kuno, M., Bawendi, M. G., Efros, A. L., and Rosen, M. *Phys. Rev. Lett.* **75**, 3728 November (1995).

[162] Bayer, M., Kuther, A., Schafer, F., Reithmaier, J. P., and Forchel, A. *Phys. Rev. B* **60**, R8481 (1999).

[163] Nakaoka, T., Saito, T., Tatebayashi, J., and Arakawa, Y. *Phys. Rev. B* **70**, 235337 December (2004).

[164] Babinski, A., Ortner, G., Raymond, S., Potemski, M., Bayer, M., Sheng, W., Hawrylak, P., Wasilewski, Z., Fafard, S., and Forchel, A. *Physical Review B (Condensed Matter and Materials Physics)* **74**(7), 075310–6 (2006).

[165] Stevenson, R. M., Young, R. J., See, P., Farrer, I., Ritchie, D. A., and Shields, A. J. *Physica E: Low-dimensional Systems and Nanostructures* **21**(2-4), 381–384 March (2004).

[166] Kim, D., Sheng, W., Poole, P. J., Dalacu, D., Lefebvre, J., Lapointe, J., Reimer, M. E., Aers, G. C., and Williams, R. L. (2008).

[167] Bayer, M., Gutbrod, T., Forchel, A., Kulakovskii, V. D., Gorbunov, A., Michel, M., Steffen, R., and Wang, K. H. *Phys. Rev. B* **58**(8), 4740 (1998).

[168] Young, R., Stevenson, R., Shields, A., Atkinson, P., Cooper, K., Ritchie, D., Groom, K., Tartakovskii, A., and Skolnick, M. *Physica E: Low-dimensional Systems and Nanostructures* **32**(1-2), 97–100 May (2006).

[169] Vuckovic, J., Fattal, D., Santori, C., Solomon, G. S., and Yamamoto, Y. *Appl. Phys. Lett.* **82**, 3596–3598 May (2003).

[170] Moreau, E., Robert, I., Manin, L., Thierry-Mieg, V., and Gerard, J. M. .

[171] Gotoh, H., Kamada, H., Saitoh, T., Ando, H., and Temmyo, J. *Phys. Rev. B* **71**, 195334–9 May (2005).

[172] Li, X., Wu, Y., Steel, D., Gammon, D., Stievater, T. H., Katzer, D. S., Park, D., Piermarocchi, C., and Sham, L. J. *Science* **301**, 809–811 August (2003).

[173] Rodt, S., Schliwa, A., Potschke, K., Guffarth, F., and Bimberg, D. *Phys. Rev. B* **71**, 155325–7 April (2005).

[174] Narvaez, G. A., Bester, G., and Zunger, A. *Phys. Rev. B* **72**, 041307–4 July (2005).

[175] Langbein, W., Borri, P., Woggon, U., Stavarache, V., Reuter, D., and Wieck, A. D. *Phys. Rev. B* **69**(16), 161301 April (2004).

[176] Nair, S. V. and Takagahara, T. *Phys. Rev. B* **55**(8), 5153 February (1997).

[177] Masumoto, Y., Okamoto, S., and Katayanagi, S. *Phys. Rev. B* **50**(24), 18658 December (1994).

[178] Stier, O., Schliwa, A., Heitz, R., Grundmann, M., and Bimberg, D. *physica status solidi (b)* **224**(1), 115–118 (2001).

[179] Barker, J. A. and OReilly, E. P. *Phys. Rev. B* **61**(20), 13840 May (2000).

[180] Stier, O., Heitz, R., Schliwa, A., and Bimberg, D. *physica status solidi (a)* **190**(2), 477–484 (2002).

[181] Bryant, G. W. *Phys. Rev. B* **41**(2), 1243 (1990).

[182] Grundmann, M., Stier, O., and Bimberg, D. *Phys. Rev. B* **52**, 11969 October (1995).

[183] Stier, O., Grundmann, M., and Bimberg, D. *Phys. Rev. B* **59**, 5688 February (1999).

[184] Seguin, R., Schliwa, A., Rodt, S., Potschke, K., Pohl, U. W., and Bimberg, D. *Phys. Rev. Lett.* **95**, 257402–4 December (2005).

[185] Bester, G., Nair, S., and Zunger, A. *Phys. Rev. B* **67**, 161306 April (2003).

[186] Tartakovskii, A. I., Makhonin, M. N., Sellers, I. R., Cahill, J., Andreev, A. D., Whittaker, D. M., Wells, J. R., Fox, A. M., Mowbray, D. J., Skolnick, M. S., Groom, K. M., Steer, M. J., Liu, H. Y., and Hopkinson, M. *Phys. Rev. B* **70**(19), 193303 November (2004).

[187] Tartakovskii, A. I., Kolodka, R. S., Liu, H. Y., Migliorato, M. A., Hopkinson, M., Makhonin, M. N., Mowbray, D. J., and Skolnick, M. S. *Appl. Phys. Lett.* **88**(13), 131115–3 March (2006).

[188] Seguin, R., Schliwa, A., Germann, T. D., Rodt, S., Potschke, K., Strittmatter, A., Pohl, U. W., Bimberg, D., Winkelnkemper, M., Hammerschmidt, T., and Kratzer, P. *Appl. Phys. Lett.* **89**(26), 263109–3 December (2006).

[189] Langbein, W. and Hvam, J. M. *Phys. Rev. B* **61**, 1692 (2000).

[190] Hinzer, K., Hawrylak, P., Korkusinski, M., Fafard, S., Bayer, M., Stern, O., Gorbunov, A., and Forchel, A. *Phys. Rev. B* **63**(7), 075314 (2001).

[191] Schliwa, A., Winkelnkemper, M., and Bimberg, D. *Phys. Rev. B* **76**, 205324–17 November (2007).

[192] Benisty, H., Sotomayor-Torres, C. M., and Weisbuch, C. *Phys. Rev. B* **44**(19), 10945 November (1991).

[193] Inoshita, T. and Sakaki, H. *Phys. Rev. B* **56**, R4355 (1997).

[194] Bockelmann, U. and Bastard, G. *Phys. Rev. B* **42**, 8947 November (1990).

[195] Schmitt-Rink, S., Miller, D. A. B., and Chemla, D. S. *Phys. Rev. B* **35**, 8113 May (1987).

[196] Heitz, R., Mukhametzhanov, I., Stier, O., Madhukar, A., and Bimberg, D. *Phys. Rev. Lett.* **83**(22), 4654 November (1999).

[197] Raymond, S., Reynolds, J. P., Merz, J. L., Fafard, S., Feng, Y., and Charbonneau, S. *Phys. Rev. B* **58**(20), R13415 November (1998).

[198] Fry, P. W., Itskevich, I. E., Mowbray, D. J., Skolnick, M. S., Finley, J. J., Barker, J. A., O'Reilly, E. P., Wilson, L. R., Larkin, I. A., Maksym, P. A., Hopkinson, M., Al-Khafaji, M., David, J. P. R., Cullis, A. G., Hill, G., and Clark, J. C. *Phys. Rev. Lett.* **84**(4), 733 (2000).

[199] Duke, C. B. and Mahan, G. D. *Physical Review* **139**, A1965 (1965).

[200] Takagahara, T. *Phys. Rev. Lett.* **71**, 3577 November (1993).

[201] Takagahara, T. *Phys. Rev. B* **60**, 2638 July (1999).

[202] Heitz, R., Born, H., Hoffmann, A., Bimberg, D., Mukhametzhanov, I., and Madhukar, A. *Appl. Phys. Lett.* **77**(23), 3746–3748 December (2000).

[203] Lemaitre, A., Ashmore, A. D., Finley, J. J., Mowbray, D. J., Skolnick, M. S., Hopkinson, M., and Krauss, T. F. *Phys. Rev. B* **63**, 161309 April (2001).

[204] Verzelen, O., Ferreira, R., and Bastard, G. *Phys. Rev. B* **62**, R4809 (2000).

[205] Lemaitre, A., Ashmore, A. D., Finley, J. J., Mowbray, D. J., Skolnick, M. S., Hopkinson, M., and Krauss, T. F. *Phys. Rev. B* **63**, 161309 April (2001).

[206] Oulton, R., Finley, J. J., Tartakovskii, A. I., Mowbray, D. J., Skolnick, M. S., Hopkinson, M., Vasanelli, A., Ferreira, R., and Bastard, G. *Phys. Rev. B* **68**, 235301 December (2003).

[207] Itoh, T., Nishijima, M., Ekimov, A. I., Gourdon, C., Efros, A. L., and Rosen, M. *Phys. Rev. Lett.* **74**(9), 1645 February (1995).

[208] Sauvage, S., Boucaud, P., Lobo, R. P. S. M., Bras, F., Fishman, G., Prazeres, R., Glotin, F., Ortega, J. M., and Gerard, J.-M. *Phys. Rev. Lett.* **88**, 177402 April (2002).

[209] Zibik, E. A., Wilson, L. R., Green, R. P., Bastard, G., Ferreira, R., Phillips, P. J., Carder, D. A., Wells, J.-P. R., Cockburn, J. W., Skolnick, M. S., Steer, M. J., and Hopkinson, M. *Phys. Rev. B* **70**, 161305 October (2004).

[210] Menzel, S., Zibik, E. A., Aivaliotis, P., Cockburn, J. W., Wilson, L. R., and Steer, M. J. *Physical Review B (Condensed Matter and Materials Physics)* **77**(15), 153302–4 April (2008).

[211] Zibik, E. A., Grange, T., Carpenter, B. A., Ferreira, R., Bastard, G., Vinh, N. Q., Phillips, P. J., Steer, M. J., Hopkinson, M., Cockburn, J. W., Skolnick, M. S., and Wilson, L. R. *Physical Review B (Condensed Matter and Materials Physics)* **77**(4), 041307–4 (2008).

[212] Aslan, B., Liu, H. C., Korkusinski, M., Hawrylak, P., and Lockwood, D. J. *Phys. Rev. B* **73**, 233311–4 June (2006).

[213] Hameau, S., Isaia, J. N., Guldner, Y., Deleporte, E., Verzelen, O., Ferreira, R., Bastard, G., Zeman, J., and Gerard, J. M. *Phys. Rev. B* **65**, 085316 February (2002).

[214] Li, X.-Q., Nakayama, H., and Arakawa, Y. *Phys. Rev. B* **59**, 5069 February (1999).

[215] Fomin, V. M., Gladilin, V. N., Devreese, J. T., Pokatilov, E. P., Balaban, S. N., and Klimin, S. N. *Phys. Rev. B* **57**, 2415 (1998).

[216] Verzelen, O., Ferreira, R., and Bastard, G. *Phys. Rev. Lett.* **88**, 146803 March (2002).

[217] Miranda, R. P., Vasilevskiy, M. I., and Trallero-Giner, C. *Phys. Rev. B* **74**, 115317–13 (2006).

[218] Findeis, F., Zrenner, A., Bohm, G., and Abstreiter, G. *Phys. Rev. B* **61**, R10579 April (2000).

[219] Toda, Y., Moriwaki, O., Nishioka, M., and Arakawa, Y. *Phys. Rev. Lett.* **82**, 4114 May (1999).

[220] Sarkar, D., van der Meulen, H. P., Calleja, J. M., Becker, J. M., Haug, R. J., and Pierz, K. *Phys. Rev. B* **71**, 081302–4 February (2005).

[221] Hameau, S., Guldner, Y., Verzelen, O., Ferreira, R., Bastard, G., Zeman, J., Lemaitre, A., and Gerard, J. M. *Phys. Rev. Lett.* **83**, 4152 November (1999).

[222] Heitz, R., Veit, M., Ledentsov, N. N., Hoffmann, A., Bimberg, D., Ustinov, V. M., Kopev, P. S., and Alferov, Z. I. *Phys. Rev. B* **56**, 10435 October (1997).

[223] Tenne, D. A., Haisler, V. A., Toropov, A. I., Bakarov, A. K., Gutakovsky, A. K., Zahn, D. R. T., and Shebanin, A. P. *Phys. Rev. B* **61**, 13785 May (2000).

[224] Emura, S., Nakagawa, T., ichi Gonda, S., and Shimizu, S. *J. Appl. Phys.* **62**, 4632–4634 December (1987).

[225] Bissiri, M., von Hogersthal, G. B. H., Bhatti, A. S., Capizzi, M., Frova, A., Frigeri, P., and Franchi, S. *Phys. Rev. B* **62**, 4642 (2000).

[226] Seebeck, J., Nielsen, T. R., Gartner, P., and Jahnke, F. *cond-mat/0406563* (2004).

[227] Paarmann, A., Guffarth, F., Warming, T., Hoffmann, A., and Bimberg, D. In *Proceedings of the 27th International Conference on the Physics of Semiconductors, Flagstaff, USA, 2004,*, (to be published).

[228] Azuhata, T., Sota, T., and Suzuki, K. *Journal of Physics: Condensed Matter* **7**, 1949–1957 (1995).

[229] Besombes, L., Kheng, K., Marsal, L., and Mariette, H. *Phys. Rev. B* **63**, 155307 March (2001).

[230] Fan, X., Takagahara, T., Cunningham, J. E., and Wang, H. *Solid State Communications* **108**, 857–861 November (1998).

[231] Gindele, F., Hild, K., Langbein, W., and Woggon, U. *Phys. Rev. B* **60**, R2157 July (1999).

[232] Moehl, S., Tinjod, F., Kheng, K., and Mariette, H. *Phys. Rev. B* **69**, 245318 June (2004).

[233] Favero, I., Cassabois, G., Ferreira, R., Darson, D., Voisin, C., Tignon, J., Delalande, C., Bastard, G., Roussignol, P., and Gerard, J. M. *Phys. Rev. B* **68**, 233301 December (2003).

[234] Peter, E., Hours, J., Senellart, P., Vasanelli, A., Cavanna, A., Bloch, J., and Gerard, J. M. *Phys. Rev. B* **69**, 041307–4 (2004).

[235] Bester, G. and Zunger, A. *Phys. Rev. B* **71**, 045318–12 (2005).

[236] Bester, G., Wu, X., Vanderbilt, D., and Zunger, A. *Phys. Rev. Lett.* **96**, 187602–4 May (2006).

[237] Ikeda, K., Ogawa, Y., Minami, F., Kuroda, S., and Takita, K. *Phys. Status Solidi C* **3**, 874–877 (2006).

[238] Yu, P. Y. and Cardona, M. *Fundamentals of Semiconductors: Physics and Materials Properties*. Springer, (2001).

[239] Takagahara, T. *Phys. Rev. B* **31**, 6552 May (1985).

[240] Kammerer, C., Voisin, C., Cassabois, G., Delalande, C., Roussignol, P., Klopf, F., Reithmaier, J. P., Forchel, A., and Gerard, J. M. *Phys. Rev. B* **66**, 041306 July (2002).

[241] Bester, G., Zunger, A., Wu, X., and Vanderbilt, D. *Phys. Rev. B* **74**, 081305–4 (2006).

[242] Sarkar, D., van der Meulen, H. P., Calleja, J. M., Meyer, J. M., Haug, R. J., and Pierz, K. *Appl. Phys. Lett.* **92**, 181909–3 May (2008).

List of publications

Free versus localized hole magnetophotoluminescence in semiconductor heterojunctions near integer filling factors
H.P. van der Meulen, D. Sarkar, J.M. Calleja, R. Hey, K.J. Friedland, and K. Ploog
Phys. Rev. B 70, 155314 (2004)
Selected for: Virtual J. of Nanoscale Science and Technology, 10 (18), 1 Nov. 2004

Role of hole localization in the magneto-luminescence of a two-dimensional electron gas
J.M. Calleja, D. Sarkar, H.P. van der Meulen, R. Hey, K.J. Friedland, and K. Ploog
Acta Physica Polonica A 106, 329 (2004)

Phonons in InAs/AlAs single quantum dots observed by optical emission
D. Sarkar, H.P. van der Meulen, J.M. Calleja, J.M. Becker, R.J. Haug, and K. Pierz
Phys. Rev. B 71, 81302(R) (2005)
Selected for: Virtual J. of Nanoscale Science and Technology, 11 (7), 21 Feb. 2005

Polaronic effects in optical transitions of single InAs/AlAs quantum dots
D. Sarkar, H.P. van der Meulen, J.M. Calleja, J.M. Becker, R.J. Haug, and K. Pierz
AIP Conf. Proc. 772, 715 (2005)

Magneto-PL Of Free And Localized Holes In Semiconductor Heterojunctions Near Integer Filling Factors
H. P. van der Meulen, D. Sarkar, J. M. Calleja, R. Hey, K. J. Friedland, and K. Ploog
AIP Conf. Proc. 772, 531 (2005)

Exciton fine structure and biexciton binding energy in single self-assembled InAs/AlAs quantum dots
D. Sarkar, H.P. van der Meulen, J.M. Calleja, J.M. Becker, R.J. Haug, and K. Pierz
J. Appl. Phys. 100, 023109 (2006)

Fine structure splitting and biexciton binding energy in single self-assembled InAs/AlAs quantum dots
D. Sarkar, H.P. van der Meulen, J.M. Calleja, J.M. Becker, R.J. Haug, and K. Pierz
Physica E 32, 111 (2006)

Nd^{3+} ion shift under domain inversion by electron beam writing in $LiNbO_3$
P. Molina, D. Sarkar, M. O. Ramrez, J. Garca Sol, L. E. Baus, B. J. Garca, and J. E. Muoz Santiuste
Appl. Phys. Lett. 90, 141901 (2007)

Resonant optical excitation of LO-phonons and intermixing in InAs/AlAs single quantum dots
D. Sarkar, H.P. van der Meulen, J.M. Calleja, J.M. Becker, R.J. Haug, and K. Pierz
Appl. Phys. Lett. 92, 181909 (2008)
Selected for: Virtual J. of Nanoscale Science and Technology, 17 (21), 26 May 2008

Piezoelectric exciton-acoustic phonon coupling in single quantum dots
D. Sarkar, H.P. van der Meulen, J.M. Calleja, J.M. Becker, R.J. Haug, and K. Pierz
Phys. Rev. B 78, 241305(R) (2008)
Selected as Editor's Suggestion paper
Selected for: Virtual J. of Nanoscale Science and Technology, 19 (2), 12 Jan 2009

Optical emission of InAs/GaAs quantum rings coupled to a two-dimensional photonic crystal microcavity
D. Sarkar, L.J. Martinez, I. Prieto-Gonzalez, H.P. van der Meulen, J.M. Calleja, D. Grana-

dos, A.G. Taboada, J.M. Garcia, A.R. Alija, P.A. Postigo
Physica E 40, 2156 (2008)

Resonant optical excitation and intermixing in InAs/AlAs single quantum dots
D. Sarkar, H.P. van der Meulen, J.M. Calleja, J.M. Becker, R.J. Haug, and K. Pierz
Physica E 40, 2172 (2008)

Piezoelectric Screening in a Single InAs/AlAs Quantum Dot
D. Sarkar, H.P. van der Meulen, J.M. Calleja, J.M. Becker, R.J. Haug, and K. Pierz
AIP Conf. Proc. (2008) (submitted)